Volume 3, Issue 1, March 2023

COMPLEX ENGINEERING SYSTEMS

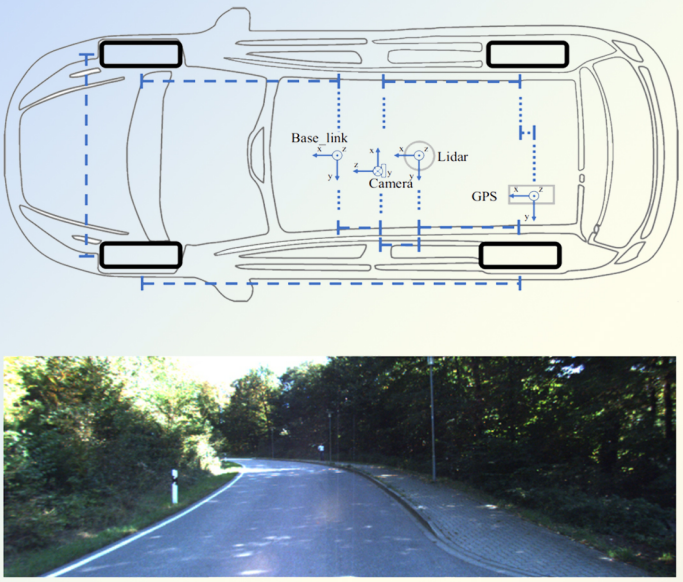

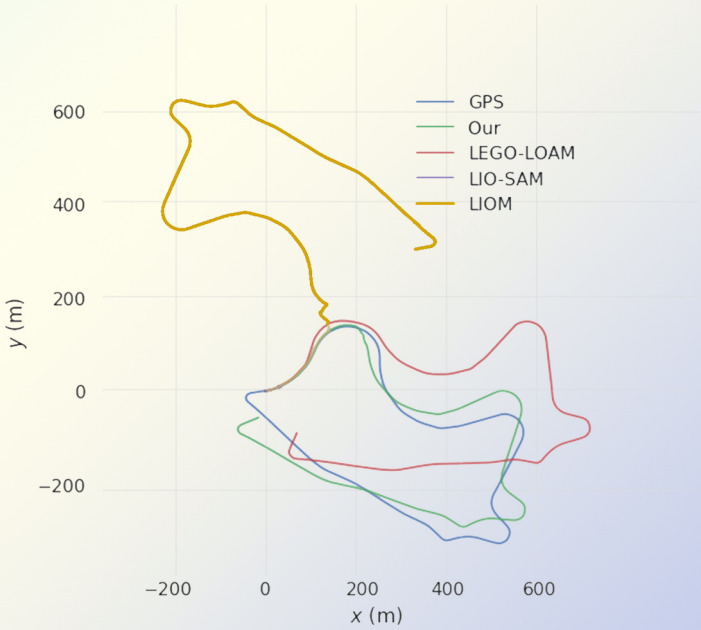

Generation of high definition map for accurate and robust localization

Zhengjie Huang, Sijie Chen, Xing Xi, Yanzhou Li*, Ya Li, Shuanglin Wu

Open Access
ISSN 2770-6249 (Online)
www.comengsys.com

EDITORIAL BOARD

GENERAL INFORMATION

About the Journal

Complex Engineering Systems (*CES*) are composed of a set of interconnected systems that their collective behaviors or properties are difficult to be predicted or managed. The context of *Complex Engineering Systems* (*CES*) is concerned with developing multi-component engineering systems, designs, or algorithms to exploit those unpredictable collective behaviors or properties. Complexity in engineering systems is in general manifested in component, product, system, interconnections of interacting subsystems or multidisciplinary system designs. In a broad sense, complexity is related to the expected amount of information may need to describe a dynamical system.

The primary objective of this journal is to provide a high-level platform for researchers and practitioners to disseminate theoretical- or engineering-oriented research output achievements within the context of *Complex Engineering Systems* (*CES*)that fosters knowledge sharing in different branches of engineering discipline. *Complex Engineering Systems* (*CES*) also publishes novel theoretical methods, algorithms, simulations, experiments, and case studies as applications of state-of-the-art research in *Complex Engineering Systems* (*CES*).

Information for Authors

Manuscripts should be prepared in accordance with Author Instructions.
Please check https://comengsys.com/pages/view/author_instructions for details.
All manuscripts should be submitted online at https://oaemesas.com/login?JournalId=comengsys.

Copyright

Permissions

Disclaimer

Publisher

OAE Publishing Inc.
245 E Main Street Ste 107, Alhambra CA 91801, USA
Website: www.oaepublish.com

Contacts

E-mail: editorial@comengsys.com
Website: https://comengsys.com/

Complex Engineering Systems

CONTENTS

Volume 3 / Issue 1 /

Research Article

Review

Fan *et al*. *Complex Eng Syst* 2023;3:5
DOI: 10.20517/ces.2023.04

Complex Engineering Systems

Research Article

Open Access

Decentralized tracking control design based on intelligent critic for an interconnected spring-mass-damper system

Wenqian Fan[1,2,3,4], Ao Liu[1,2,3,4], Ding Wang[1,2,3,4]

[1]Faculty of Information Technology, Beijing University of Technology, Beijing 100124, China.
[2]Beijing Key Laboratory of Computational Intelligence and Intelligent System, Beijing University of Technology, Beijing 100124, China.
[3]Beijing Institute of Artificial Intelligence, Beijing University of Technology, Beijing 100124, China.
[4]Beijing Laboratory of Smart Environmental Protection, Beijing University of Technology, Beijing 100124, China.

Correspondence to: Prof. Ding Wang, Faculty of Information Technology, Beijing University of Technology, 100 Pingleyuan, Chaoyang District, Beijing 100124, China. E-mail: dingwang@bjut.edu.cn

How to cite this article: Fan W, Liu A, Wang D. Decentralized tracking control design based on intelligent critic for an interconnected spring-mass-damper system. *Complex Eng Syst* 2023;3:5. http://dx.doi.org/10.20517/ces.2023.04

Received: 17 Feb 2023 **First Decision:** 6 Mar 2023 **Revised:** 14 Mar 2023 **Accepted:** 20 Mar 2023 **Published:** 30 Mar 2023

Academic Editor: Yurong Liu **Copy Editor:** Fanglin Lan **Production Editor:** Fanglin Lan

Abstract

In this paper, the decentralized tracking control (DTC) problem is investigated for a class of continuous-time nonlinear systems with external disturbances. First, the DTC problem is resolved by converting it into the optimal tracking controller design for augmented tracking isolated subsystems (ATISs). A cost function with a discount is taken into consideration. Then, in the case of external disturbances, the DTC scheme is effectively constructed via adding the appropriate feedback gain to each ATIS. In addition, utilizing the approximation property of the neural network, the critic network is constructed to solve the Hamilton-Jacobi-Isaacs equation, which can derive the optimal tracking control law and the worst disturbance law. Moreover, the updating rule is improved during the process of weight learning, which removes the requirement for initial admission control. Finally, through the interconnected spring-mass-damper system, a simulation example is given to verify the availability of the DTC scheme.

Keywords: Adaptive dynamic programming, discounted cost function, decentralized tracking control, disturbance rejection, interconnected spring-mass-damper systems, neural networks, optimal control

1. INTRODUCTION

For large-scale nonlinear interconnected systems, which are considered as nonlinear plants consisting of many interconnected subsystems, decentralized control has become a research hotspot in the last few decades[1–4]. Compared with the centralized control, the decentralized control has the advantages of simplifying the structure and reducing the computation burden of the controller. Besides, the local controller only depends on the information of the local subsystem. Meanwhile, with the development of science and technology, interconnected engineering applications have become increasingly complex, such as robotic systems[5] and power systems[6,7]. In[8–10], we found that the decentralized control of the large-scale system was connected with the optimal control of the isolated subsystems, which means the optimal control method[11–14] can be adopted to achieve the design purpose of the decentralized controllers. However, the optimal control of the nonlinear system often needs to solve the Hamilton-Jacobi-Bellman (HJB) or Hamilton-Jacobi-Isaacs (HJI) equation, which can be solved by using the adaptive dynamic programming (ADP) method[15,16]. Besides, in[13], Wang *et al.* investigated the latest intelligent critic framework for advanced optimal control. In[14], the optimal feedback stabilization problem was discussed with discounted guaranteed cost for nonlinear systems. It follows that the interconnection plays a significant role in designing the controller. Hence, it can be classified as decentralized and distributed control schemes. There is a certain distinction between decentralized control and distributed control. For decentralized control, each sub-controller only uses local information and the interconnection among subsystems can be assumed to be weak in nature. Compared with the decentralized control, the distributed control[17–19] can be introduced to improve the performance of the subsystems when the interconnections among subsystems become strong. In[20], the distributed optimal observer was devised to assess the nonlinear leader state for all followers. In[21], the distributed control was developed by means of online reinforcement learning for interconnected systems with exploration.

It is worth mentioning that the ADP algorithm has been extensively employed for dealing with various optimal regulation problems and tracking problems[22–24], which will achieve the goal, that is, the actual signal can track the reference signal under the noisy and the uncertain environment. In[25], Ha *et al.* proposed a novel cost function to explore the evaluation framework of the optimal tracking control problem. Then, aimed at complicated control systems, it is necessary to consider decentralized tracking control (DTC) problems[26–29]. The DTC systems can be transformed into the the nominal augmented tracking isolated subsystems (ATISs), which are composed of the tracking error and the reference signal. In[26], Qu *et al.* proposed a novel formulation consisting of a steady-state controller and a modified optimal feedback controller of the DTC strategy. Besides, the asymptotic DTC was realized by introducing two integral bounded functions in[27]. In[28], Liu *et al.* proposed a finite-time DTC method for a class of nonstrict feedback interconnected systems with disturbances. Moreover, the adaptive fuzzy output-feedback DTC design was investigated for switched large-scale systems in[29].

Game theory is a discipline that implements corresponding strategies. It contains cooperative and noncooperative types, that is, zero-sum (ZS) games and non-ZS games. In particular, ZS games have been widely applied in many fields[30–33]. The object of the ZS game is to derive the Nash equilibrium of nonliner systems, which makes the cost function optimized. In[31], the finite-horizon H-infinity state estimator design was studied for periodic neural networks over multiple fading channels. The noncooperative control problem was formulated as a two-player ZS game in[32]. In[33], Wang *et al.* investigated the stability of the general value iteration algorithm for ZS games. At the same time, we can also combine the ZS problem with the tracking problem to make the system more stable while achieving the trajectory tracking. In[34], Zhang *et al.* developed an online model-free integral reinforcement learning algorithm for solving the H-infinity optimal tracking problem for completely unknown systems. In[35], a general bounded L_2 gain tracking policy was introduced with a discounted function. In[36], Hou *et al.* proposed an action-disturbance-critic neural network frame to realize the iterative dual heuristic programming algorithm.

As can be seen from the above, there are few studies that combine the DTC problem with the ZS game problem. It is necessary to take the related discounted cost function into account for the DTC system, which can transform the DTC problem into an optimal control problem with disturbances. In practice, the existence of disturbances will make an unpredictable impact on the plant. Hence, it is of vital importance to consider the stability of the DTC system. In the experimental simulation, it is a challenge to achieve the goal of effective online weight training, which is implemented under the tracking control law and the disturbance control law. Consequently, in this paper, we put forward a novel method in view of ADP to resolve the DTC problem with external disturbances for continuous-time (CT) nonlinear systems. More importantly, for the sake of overcoming the difficulty of selecting initial admissible control policies, an additional term is added during the weight updating process. Remarkably, in this paper, we introduce the discount factor for maximizing and minimizing the corresponding cost function.

The contributions of this paper are as follows: First, considering the disturbance input in the DTC system, the strategy feasibility and the system stability are discussed through theoretical proofs. It is worth noting that the discount factor is introduced to the cost function. Moreover, in the process of online weight training, we can make the DTC system reach a stable state without selecting the initial admissible control law. Additionally, we present the experimental process of the spring-mass-damper system. Besides, we derive the desired tracking error curves as well as control strategy curves, which demonstrates that they are uniformly ultimately bounded (UUB).

The whole paper is divided into six sections. The first section is the introduction of relevant background knowledges of the research content. The second section is the problem statement of basic problems about the two person ZS game and the DTC strategy. In the third section, we design the decentralized tracking controller by using the optimal control method through solving the HJI equations. Meanwhile, the relevant lemma and theorem are given to validate the establishment of the DTC strategy. In the fourth section, the design method in accordance with adaptive critic is elaborated. Most importantly, an improved critic learning rule is implemented via critic networks. In the fifth section, the practicability of this method is validated by an interconnected spring-mass-damper system. Finally, the sixth section displays conclusions and summarizes overall research content of the whole paper.

2. PROBLEM STATEMENT

Consider a CT nonlinear interconnected system with disturbances, which is composed of N interconnected subsystems. Its dynamic description can be expressed as

$$\dot{x}_i(t) = f_i(x_i(t)) + g_i(x_i(t))\left(\bar{u}_i(x_i(t)) + \bar{Z}_i(x(t))\right) + h_i(x_i(t))v_i(x_i(t)), \tag{1}$$

where $i = 1, 2, \ldots, N$, $x_i(t) \in \mathbb{R}^{n_i}$ is the state vector of the ith subsystem and $x(t)$ denotes the partial interconnected state related to other subsystems of the large-scale system. $\bar{u}_i(x_i(t)) \in \mathbb{R}^{m_i}$ is the control input and $v_i(x_i(t)) \in \mathbb{R}^{q_i}$ is the external disturbance input. As for the ith subsystem, we denote $f_i(x_i(t))$, $g_i(x_i(t))$, $h_i(x_i(t))$, and $\bar{Z}_i(x(t))$ as the nonlinear internal dynamics, the input gain matrix, the disturbance gain matrix, and the interconnected item in sequence. Besides, $[x_1^{\mathsf{T}}, x_2^{\mathsf{T}}, \ldots, x_N^{\mathsf{T}}]^{\mathsf{T}} \in \mathbb{R}^n$ denotes the whole state of the large-scale system Equation (1), where $n = \sum_{i=1}^{N} n_i$. Accordingly, $x_1, x_2, \ldots, x_N$ are named local states and $\bar{u}_1(x_1), \bar{u}_2(x_2), \ldots, \bar{u}_N(x_N)$ are called local controllers. We let $R_i \in \mathbb{R}^{m_i \times m_i}$ be the symmetric positive definite matrix and denote $Z_i(x(t)) = {R_i}^{1/2}\bar{Z}_i(x(t))$. In addition, $Z_i(x(t)) \in \mathbb{R}^{m_i}$ is bounded as follows:

$$\|Z_i(x(t))\| \le \sum_{j=1}^{N} \alpha_{ij}\theta_{ij}(x_j) \le \sum_{j=1}^{N} \beta_{ij}\theta_j(x_j), \tag{2}$$

where $j = 1, 2, \ldots, N$, α_{ij} is the nonnegative constant, $\theta_{ij}(x_j)$ is the positive semidefinite function. Besides, we define $\theta_j(x_j) = \max\{\theta_{1j}(x_j), \theta_{2j}(x_j), \ldots, \theta_{Nj}(x_j)\}$ and the element of $\{\theta_{1j}(x_j), \theta_{2j}(x_j), \ldots, \theta_{Nj}(x_j)\}$

will not reach zero at the same time. For this reason, $\beta_{ij} \geq \alpha_{ij}\theta_{ij}(x_j)/\theta_j(x_j)$ holds, where β_{ij} is also the nonnegative constant.

In this paper, considering the nonlinear system Equation (1), a reference system is introduced as follows:

$$\dot{r}_i(t) = \zeta_i(r_i(t)), \tag{3}$$

where $r_i(t) \in \mathbb{R}^{n_i}$ denotes the desired trajectory with $r_i(0) = r_{i0}$, the function ζ_i is locally Lipschitz continuous satisfying $\zeta_i(0) = 0$. For the ith subsystem, the trajectory tracking error can be defined as $e_i(t) = x_i(t) - r_i(t)$ with $e_i(0) = e_{i0}$. Thus, the dynamics of the tracking error is

$$\dot{e}_i(t) = f_i(x_i(t)) + g_i(x_i(t))\left(\bar{u}_i(x_i(t)) + \bar{Z}_i(x(t))\right) + h_i(x_i(t))v_i(x_i(t)) - \zeta_i(r_i(t)). \tag{4}$$

Noticing $x_i(t) = e_i(t) + r_i(t)$, we define the augmented subsystem states as $y_i(t) = [e_i^{\mathsf{T}}(t), r_i^{\mathsf{T}}(t)]^{\mathsf{T}} \in \mathbb{R}^{2n_i}$ with $y_i(0) = y_{i0} = [e_{i0}^{\mathsf{T}}, r_{i0}^{\mathsf{T}}]^{\mathsf{T}}$. Hence, the dynamic of the ith ATIS based on Equations (1) and (3) can be formulated as a concise form

$$\dot{y}_i(t) = \mathcal{F}_i(y_i(t)) + \mathcal{G}_i(y_i(t))\left(\bar{u}_i(y_i(t)) + \bar{Z}_i(y(t))\right) + \mathcal{H}_i(y_i(t))v_i(y_i(t)), \tag{5}$$

where $\mathcal{F}_i(y_i(t)) \in \mathbb{R}^{2n_i}$, $\mathcal{G}_i(y_i(t)) \in \mathbb{R}^{2n_i \times m_i}$, and $\mathcal{H}_i(y_i(t)) \in \mathbb{R}^{2n_i \times q_i}$ respectively. Specifically, they can be expressed as

$$\mathcal{F}_i(y_i(t)) = \begin{bmatrix} f_i(e_i(t) + r_i(t)) - \zeta_i(r_i(t)) \\ \zeta_i(r_i(t)) \end{bmatrix}, \tag{6}$$

$$\mathcal{G}_i(y_i(t)) = \begin{bmatrix} g_i(e_i(t) + r_i(t)) \\ 0_{n_i \times m_i} \end{bmatrix}, \tag{7}$$

$$\mathcal{H}_i(y_i(t)) = \begin{bmatrix} h_i(e_i(t) + r_i(t)) \\ 0_{n_i \times q_i} \end{bmatrix}. \tag{8}$$

We aim to design a pair of decentralized control policies $\bar{u}_1, \bar{u}_2, \ldots, \bar{u}_N$ to ensure that large-scale system Equation (1) can track the desired object while being restricted by external disturbances. It means that as $t \to +\infty$, $\|x_i(t) - r_i(t)\| \to 0$. Meanwhile, it is noteworthy that the control pair $\bar{u}_1, \bar{u}_2, \ldots, \bar{u}_N$ should be pointed out only as a corresponding controller with the local information. In what follows, it presents the DTC problem by transforming it into the optimal controller design of ATISs by considering an appropriate discounted cost function.

3. DTC DESIGN VIA OPTIMAL REGULATION

3.1. Optimal control and the HJI equations

In this section, the optimal DTC strategy of the ATIS with the disturbance rejection is elaborated. It is addressed by solving the HJI equation with a discounted cost function. Then, we consider the nominal part of the augmented system Equation (5) as

$$\dot{y}_i(t) = \mathcal{F}_i(y_i(t)) + \mathcal{G}_i(y_i(t))u_i(y_i(t)) + \mathcal{H}_i(y_i(t))v_i(y_i(t)). \tag{9}$$

We assume that $\mathcal{F}_i + \mathcal{G}_i u_i + \mathcal{H}_i v_i$ is Lipschitz continuous on a set $\Omega_i \subset \mathbb{R}^{2n_i}$, which is commonly used in the field of adaptive critic control to ensure the existence and uniqueness of the solution for the differential equation. Related to the ith ATIS, we manage to minimize and maximize the discounted cost function as

$$J_i(y_{i0}) = \int_0^{\infty} e^{-\lambda_i(\tau - t)} \left\{ y_i^{\mathsf{T}}(\tau) Q_i y_i(\tau) + u_i^{\mathsf{T}}(y_i(\tau)) R_i u_i(y_i(\tau)) - \varrho_i^2 v_i^{\mathsf{T}}(y_i(\tau)) v_i(y_i(\tau)) \right\} \mathrm{d}\tau, \tag{10}$$

where $Q_i \in \mathbb{R}^{2n_i \times 2n_i}$, $R_i \in \mathbb{R}^{m_i \times m_i}$ are both positive definite matrices. Herein, we let $y_i^{\mathsf{T}} Q_i y_i - \varrho_i^2 v_i^{\mathsf{T}}(y_i) v_i(y_i) = \gamma_i^2(y_i)$ and $\theta_i(y_i) \leq \sqrt{\gamma_i^2(y_i) - \lambda_i J_i(y_i)}$, where $\gamma_i^2(y_i) > \lambda_i J_i(y_i)$. It is worth noting that this inequality is employed to prove the feasibility of Theorem 1. Then, Equation (10) can be equivalent to

$$J_i(y_{i0}) = \int_0^\infty e^{-\lambda_i(\tau - t)} \left\{ \gamma_i^2(y_i) + u_i^{\mathsf{T}}(y_i(\tau)) R_i u_i(y_i(\tau)) \right\} \mathrm{d}\tau. \tag{11}$$

If Equation (11) is continuously differentiable, the nonlinear Lyapunov equation is the infinitely small form of Equation (11). The Lyapunov equation is as follows:

$$\gamma_i^2(y_i) + u_i^{\mathsf{T}}(y_i) R_i u_i(y_i) - \lambda_i J_i(y_i) + (\nabla J_i(y_i))^{\mathsf{T}} [\mathcal{F}_i(y_i) + \mathcal{G}_i(y_i) u_i(y_i) + \mathcal{H}_i(y_i) v_i(y_i)] = 0. \tag{12}$$

Define the Hamiltonian of the ith ATIS for the optimization problem as

$$\begin{aligned} H_i(y_i, u_i, v_i, \nabla J_i(y_i)) = {} & \gamma_i^2(y_i) + u_i^{\mathsf{T}}(y_i) R_i u_i(y_i) - \lambda_i J_i(y_i) + (\nabla J_i(y_i))^{\mathsf{T}} \\ & \times [\mathcal{F}_i(y_i) + \mathcal{G}_i(y_i) u_i(y_i) + \mathcal{H}_i(y_i) v_i(y_i)]. \end{aligned} \tag{13}$$

To acquire the saddle point solution $\{u_i^*, v_i^*\}$, the local optimal cost function need to satisfy the following Nash condition

$$J_i^*(y_{i0}) = \min_{u_i} \max_{v_i} J_i(y_{i0}). \tag{14}$$

Then, the optimal cost function $J_i^*(y_i)$ is derived via solving the local HJI equation in the following:

$$\min_{u_i} \max_{v_i} H_i(y_i, u_i, v_i, \nabla J_i^*(y_i)) = 0. \tag{15}$$

Due to the saddle point solution $\{u_i^*, v_i^*\}$ satisfies the extremum theorem, the optimal tracking control law and the worst disturbance law can be computed by

$$u_i^*(y_i) = -\frac{1}{2} R_i^{-1} \mathcal{G}_i^{\mathsf{T}}(y_i) \nabla J_i^*(y_i), \tag{16}$$

$$v_i^*(y_i) = \frac{1}{2\varrho_i^2} \mathcal{H}_i^{\mathsf{T}}(y_i) \nabla J_i^*(y_i). \tag{17}$$

Substituting the optimal tracking control strategy Equation (16) into Equation (15), the HJI equation for the ith ATIS becomes

$$(\nabla J_i^*(y_i))^{\mathsf{T}} [\mathcal{F}_i(y_i) + \mathcal{H}_i(y_i) v_i^*(y_i)] + \gamma_i^2(y_i) - \lambda_i J_i^*(y_i) - \frac{1}{4} (\nabla J_i^*(y_i))^{\mathsf{T}} \mathcal{G}_i(y_i) R_i^{-1} \mathcal{G}_i^{\mathsf{T}}(y_i) \nabla J_i^*(y_i) = 0. \tag{18}$$

3.2. Establishment of the DTC strategy design

In the following, we present the DTC strategy by adding the feedback gain to the interconnected system Equation (5). Herein, the following lemma is given by

Lemma 1 Considering the ATIS Equation (9), the feedback control

$$\bar{u}_i(y_i) = k_i u_i^*(y_i) \tag{19}$$

can ensure the N ATISs are asymptotically stable as long as $k_i \geq 1/2$, which makes the tracking error approach to zero.

Proof. The lemma can be proved by showing $J_i^*(y_i)$ is a candidate Lyapunov function. We can find $J_i^*(y_i) \geq 0$ in Equation (11), which implies that $J_i^*(y_i)$ is a positive definite function. The derivative of $J_i^*(y_i)$ along with the ith ATIS is given by

$$\begin{aligned}\dot{J}_i^*(y_i) &= (\nabla J_i^*(y_i))^{\mathsf{T}} \dot{y}_i \\ &= (\nabla J_i^*(y_i))^{\mathsf{T}} [\mathcal{F}_i(y_i) + \mathcal{G}_i(y_i)\bar{u}_i(y_i) + \mathcal{H}_i(y_i)v_i(y_i)].\end{aligned} \tag{20}$$

Substituting Equations (18) and (19) into Equation (20), we can rewrite it as

$$\begin{aligned}\dot{J}_i^*(y_i) =& -\gamma_i^2(y_i) + \lambda_i J_i^*(y_i) + \frac{1}{4}(\nabla J_i^*(y_i))^{\mathsf{T}} \mathcal{G}_i(y_i) R_i^{-1} \mathcal{G}_i^{\mathsf{T}}(y_i) \nabla J_i^*(y_i) \\ & - \frac{1}{2} k_i (\nabla J_i^*(y_i))^{\mathsf{T}} \mathcal{G}_i(y_i) R_i^{-1} \mathcal{G}_i^{\mathsf{T}}(y_i) \nabla J_i^*(y_i) \\ =& -(\gamma_i^2(y_i) - \lambda_i J_i^*(y_i)) - \left(\frac{1}{2}k_i - \frac{1}{4}\right) \left\| R_i^{-\frac{1}{2}} \mathcal{G}_i^{\mathsf{T}}(y_i) \nabla J_i^*(y_i) \right\|^2 .\end{aligned} \tag{21}$$

Observing Equation (21), we can obtain that $\dot{J}_i^*(y_i) < 0$ holds under the condition $\gamma_i^2(y_i) > \lambda_i J_i^*(y_i)$ for all $k_i \geq 1/2$ and $y_i \neq 0$. Thus, the conditions are satisfied for Lyapunov local stability theory and the actual state of each ATIS can realize desired tracking objectives under the feedback control strategy. The proof is completed.

Remark 1. *It is worth mentioning that only when $k_i = 1$, the feedback control is optimal. Then, we will show the following theorem to verify the proposed control law can effectively establish the DTC strategy.*

Theorem 1 Taking Equation (2) and the interconnected augmented tracking system Equation (5) into account, there exist N positive numbers k_i^*, such that, for any $k_i > k_i^*$, the feedback control polices given by Equation (19) guarantee that the interconnected tracking system can maintain the asymptotic stability. In other words, the control pair $\bar{u}_1(y_1), \bar{u}_2(y_2), \ldots, \bar{u}_N(y_N)$ is the DTC strategy for the large-scale system.

Proof. Inspired by Lemma 1, we observe that $J_i^*(y_i)$ is the Lyapunov function. Therefore, a composite Lyapunov function of $J_i^*(y_i)$ is chosen as

$$\mathcal{L}(y) = \sum_{i=1}^{N} \mu_i J_i^*(y_i), \tag{22}$$

where μ_i is a random positive constant. Taking the time derivative of $\mathcal{L}(y)$, we have

$$\begin{aligned}\dot{\mathcal{L}}(y) =& \sum_{i=1}^{N} \mu_i \dot{J}_i^*(y_i) \\ =& \sum_{i=1}^{N} \mu_i \Big\{ (\nabla J_i^*(y_i))^{\mathsf{T}} [\mathcal{F}_i(y_i) + \mathcal{G}_i(y_i)\bar{u}_i(y_i) + \mathcal{H}_i(y_i)v_i(y_i)] \\ & + (\nabla J_i^*(y_i))^{\mathsf{T}} \mathcal{G}_i(y_i) \bar{Z}_i(y) \Big\}.\end{aligned} \tag{23}$$

Considering Equation (2), the mentioned inequality $\theta_i(y_i) \leq \sqrt{\gamma_i^2(y_i) - \lambda_i J_i(y_i)}$, where $\gamma_i^2(y_i) > \lambda_i J_i(y_i)$, and Equation (21), the upper formula can be converted to

$$\begin{aligned}\dot{\mathcal{L}}(y) \leq & -\sum_{i=1}^{N} \mu_i \Big\{ \gamma_i^2(y_i) - \lambda_i J_i(y_i) + \left(\frac{1}{2}k_i - \frac{1}{4}\right) \left\| (\nabla J_i^*(y_i))^{\mathsf{T}} \mathcal{G}_i(y_i) R_i^{-\frac{1}{2}} \right\|^2 \\ & - \left\| (\nabla J_i^*(y_i))^{\mathsf{T}} \mathcal{G}_i(y_i) R_i^{-\frac{1}{2}} \right\| \sum_{i=1}^{N} \beta_{ij} \sqrt{\gamma_i^2(y_i) - \lambda_i J_i(y_i)} \Big\}.\end{aligned} \tag{24}$$

Herein, in order to transform Equation (24) to the compact form, we denote

$$M = \mathrm{diag}\{\mu_1, \mu_2, \ldots, \mu_N\}, \tag{25}$$

$$K = \mathrm{diag}\left\{\frac{1}{2}k_1 - \frac{1}{4}, \frac{1}{2}k_2 - \frac{1}{4}, \ldots, \frac{1}{2}k_N - \frac{1}{4}\right\}, \tag{26}$$

$$B = \begin{bmatrix} \beta_{11}\ \beta_{12}\ \ldots\ \beta_{1N} \\ \beta_{21}\ \beta_{22}\ \ldots\ \beta_{2N} \\ \vdots\ \ \vdots\ \ \ddots\ \ \vdots \\ \beta_{N1}\beta_{N2}\ \ldots\ \beta_{NN} \end{bmatrix}. \tag{27}$$

Therefore, we introduce a $2N$-dimensional column vector ϑ, which consists of the N-dimensional column vector $\sqrt{\gamma_i^2(y_i) - \lambda_i J_i(y_i)}$ and the N-dimensional column vector $\left\|(\nabla J_i^*(y_i))^{\mathsf{T}} \mathcal{G}_i(y_i) R_i^{-\frac{1}{2}}\right\|$. Its form is as follows:

$$\vartheta = \begin{bmatrix} \sqrt{\gamma_1^2(y_1) - \lambda_1 J_1(y_1)} \\ \sqrt{\gamma_2^2(y_2) - \lambda_2 J_2(y_2)} \\ \vdots \\ \sqrt{\gamma_N^2(y_N) - \lambda_N J_N(y_N)} \\ \hline \left\|(\nabla J_1^*(y_1))^{\mathsf{T}} \mathcal{G}_1(y_1) R_1^{-\frac{1}{2}}\right\| \\ \left\|(\nabla J_2^*(y_2))^{\mathsf{T}} \mathcal{G}_2(y_2) R_2^{-\frac{1}{2}}\right\| \\ \vdots \\ \left\|(\nabla J_N^*(y_N))^{\mathsf{T}} \mathcal{G}_N(y_N) R_N^{-\frac{1}{2}}\right\| \end{bmatrix} \tag{28}$$

Next, Equation (24) can be transformed to the following compact form:

$$\begin{aligned} \dot{\mathcal{L}}(y) &\leq -\vartheta^{\mathsf{T}} \begin{bmatrix} M & -\frac{1}{2}B^{\mathsf{T}}M \\ -\frac{1}{2}MB & MK \end{bmatrix} \vartheta \\ &\triangleq -\vartheta^{\mathsf{T}} \mathscr{A} \vartheta. \end{aligned} \tag{29}$$

According to Equation (29), it can be concluded that when k_i is sufficiently large, the matrix $\mathscr{A}$ is positive definite, which means there exist k_i^* so that any $k_i > k_i^*$ sufficiently large to ensure the positive definite property of $\mathscr{A}$. Then, we get $\dot{\mathcal{L}}(y) < 0$. Consequently, the DTC strategy with external disturbances is constructed. The proof is completed.

Obviously, the key point of designing the DTC strategy is to obtain the optimal controller of the ATIS based on Theorem 1. Next, for the sake of getting hold of optimal controllers for the N ATISs by solving the HJI equations, in the following, we employ the ADP method to obtain the approximate optimal solutions by means of critic networks.

4. OPTIMAL DTC DESIGN VIA NEURAL NETWORKS

4.1. Implementation procedure via neural networks

In this section, we show the process of finding the approximate optimal solution by employing the ADP method based on neural networks. The critic networks have the capability of approximating nonlinear mapping, and the approximate cost function can be derived for the DTC system. Hence, $J_i^*(y_i)$ can be expressed as

$$J_i^*(y_i) = w_{ci}^{\mathsf{T}}\sigma_{ci}(y_i) + \xi_{ci}(y_i), \tag{30}$$

where $w_{ci} \in \mathbb{R}^{l_{ci}}$ is the ideal weight vector, l_{ci} is the number of neurons in the hidden layer, $\sigma_{ci}(y_i) \in \mathbb{R}^{l_{ci}}$ is the activation function, and $\xi_{ci}(y_i)$ is the reconstruction error of the ith neural network. The gradient of $J_i^*(y_i)$ is formulated as

$$\nabla J_i^*(y_i) = (\nabla\sigma_{ci}(y_i))^{\mathsf{T}} w_{ci} + \nabla\xi_{ci}(y_i), \tag{31}$$

Considering Equation (16), the optimal control policy for the ith ATIS is replaced by

$$u_i^*(y_i) = -\frac{1}{2}R_i^{-1}\mathcal{G}_i^{\mathsf{T}}(y_i)\left((\nabla\sigma_{ci}(y_i))^{\mathsf{T}} w_{ci} + \nabla\xi_{ci}(y_i)\right). \tag{32}$$

Utilizing Equations (31) and (32), the Hamiltonian associated with the ith ATIS is obtained as

$$\begin{aligned} H_i(y_i, v_i(y_i), w_{ci}) = {} & \gamma_i^2(y_i) - \lambda_i(w_{ci}^{\mathsf{T}}\sigma_{ci}(y_i)) + w_{ci}^{\mathsf{T}}(\nabla\sigma_{ci}(y_i))[\mathcal{F}_i(y_i) + \mathcal{H}_i(y_i)v_i(y_i)] \\ & - \frac{1}{4}w_{ci}^{\mathsf{T}}\nabla\sigma_{ci}(y_i)\mathcal{G}_i(y_i)R_i^{-1}\mathcal{G}_i^{\mathsf{T}}(y_i)(\nabla\sigma_{ci}(y_i))^{\mathsf{T}} w_{ci} + e_{chi} = 0, \end{aligned} \tag{33}$$

where e_{chi} is the residual error of the neural network. To avoid the unknown ideal weight vector, we construct N critic neural networks to approximate $J_i^*(y_i)$ as

$$\hat{J}_i^*(y_i) = \hat{w}_{ci}^{\mathsf{T}}\sigma_{ci}(y_i), \tag{34}$$

where $\hat{w}_{ci}$ is the estimated weight. Likewise, the derivative of $\hat{J}_i^*(y_i)$ is

$$\nabla\hat{J}_i^*(y_i) = (\nabla\sigma_{ci}(y_i))^{\mathsf{T}}\hat{w}_{ci}. \tag{35}$$

Based on Equation (35), we obtain the estimated value of $u_i^*(y_i)$ and $v_i^*(y_i)$ as

$$\hat{u}_i^*(y_i) = -\frac{1}{2}R_i^{-1}\mathcal{G}_i^{\mathsf{T}}(y_i)(\nabla\sigma_{ci}(y_i))^{\mathsf{T}}\hat{w}_{ci}, \tag{36}$$

$$\hat{v}_i^*(y_i) = \frac{1}{2\varrho_i^2}\mathcal{H}_i^{\mathsf{T}}(y_i)(\nabla\sigma_{ci}(y_i))^{\mathsf{T}}\hat{w}_{ci}. \tag{37}$$

Considering Equations (34-36), the approximate Hamiltonian is expressed as

$$\begin{aligned} \hat{H}_i(y_i, \hat{v}_i^*(y_i), \hat{w}_{ci}) = {} & \gamma_i^2(y_i) - \lambda_i(\hat{w}_{ci}^{\mathsf{T}}\sigma_{ci}(y_i)) + \hat{w}_{ci}^{\mathsf{T}}(\nabla\sigma_{ci}(y_i))[\mathcal{F}_i(y_i) + \mathcal{H}_i(y_i)\hat{v}_i^*(y_i)] \\ & - \frac{1}{4}\hat{w}_{ci}^{\mathsf{T}}\nabla\sigma_{ci}(y_i)\mathcal{G}_i(y_i)R_i^{-1}\mathcal{G}_i^{\mathsf{T}}(y_i)(\nabla\sigma_{ci}(y_i))^{\mathsf{T}}\hat{w}_{ci} = e_{ci}. \end{aligned} \tag{38}$$

Then, we obtain an error function of the Hamiltonian, which is denoted as e_{ci} and is expressed by

$$\begin{aligned} e_{ci} = {} & \hat{H}_i(y_i, \hat{v}_i^*(y_i), \hat{w}_{ci}) - H_i(y_i, v_i(y_i), w_{ci}) \\ = {} & \lambda_i(\tilde{w}_{ci}^{\mathsf{T}}\sigma_{ci}(y_i)) - \tilde{w}_{ci}^{\mathsf{T}}(\nabla\sigma_{ci}(y_i))[\mathcal{F}_i(y_i) + \mathcal{H}_i(y_i)v_i(y_i)] \\ & - \frac{1}{4}\tilde{w}_{ci}^{\mathsf{T}}\nabla\sigma_{ci}(y_i)\mathcal{G}_i(y_i)R_i^{-1}\mathcal{G}_i^{\mathsf{T}}(y_i)(\nabla\sigma_{ci}(y_i))^{\mathsf{T}}\tilde{w}_{ci} \\ & + \frac{1}{2}w_{ci}^{\mathsf{T}}\nabla\sigma_{ci}(y_i)\mathcal{G}_i(y_i)R_i^{-1}\mathcal{G}_i^{\mathsf{T}}(y_i)(\nabla\sigma_{ci}(y_i))^{\mathsf{T}}\tilde{w}_{ci} - e_{chi}, \end{aligned} \tag{39}$$

where $\tilde{w}_{ci} = w_{ci} - \hat{w}_{ci}$ is the weight error vector. At present, in order to minimize the objective function $E_{ci} = (1/2)e_{ci}^{\mathsf{T}}e_{ci}$, the normalised steepest descent algorithm based on Equation (38) is employed as follows:

$$\dot{\hat{w}}_{ci} = -\eta_{ci}\frac{1}{(1+\phi_i^{\mathsf{T}}\phi_i)^2}\left(\frac{\partial E_{ci}}{\partial \hat{w}_{ci}}\right) = -\eta_{ci}\frac{\phi_i}{(1+\phi_i^{\mathsf{T}}\phi_i)^2}e_{ci}, \tag{40}$$

where $\eta_{ci} > 0$ represents the basic learning rate. Besides, $(1+\phi_i^{\mathsf{T}}\phi_i)^2$ is introduced for the normalization to simplify the critic error dynamics, and ϕ_i is derived as

$$\phi_i = \nabla\sigma_{ci}(y_i)[\mathcal{F}_i(y_i) + \mathcal{H}_i(y_i)\hat{v}_i^*(y_i)] - \lambda_i\sigma_{ci}(y_i). \tag{41}$$

Usually, in the traditional weight training process, it is often necessary to select the appropriate initial weight vector for effective training. To eliminate the initial admissible control law, an improved critic learning rule is presented in the following.

4.2. Improved critic learning rule via neural networks

Herein, an additional Lyapunov function is introduced for the purpose of improving the critic learning mechanism. Then, the following rational assumption is given.

Assumption 1 Consider the dynamic of the ith ATIS Equation (9) with the optimal cost function Equation (14) and the closed-loop optimal control policy Equation (32). We select $J_{si}(y_i)$ as a continuously differentiable Lyapunov function and have the following relation:

$$\dot{J}_{si}(y_i) = (\nabla J_{si}(y_i))^{\mathsf{T}}[\mathcal{F}_i(y_i) + \mathcal{G}_i(y_i)u_i^*(y_i) + \mathcal{H}_i(y_i)v_i^*(y_i)] < 0. \tag{42}$$

In other words, there exists a positive definite matrix $\mathcal{B}$ such that

$$(\nabla J_{si}(y_i))^{\mathsf{T}}[\mathcal{F}_i(y_i) + \mathcal{G}_i(y_i)u_i^*(y_i) + \mathcal{H}_i(y_i)v_i^*(y_i)] = -(\nabla J_{si}(y_i))^{\mathsf{T}}\mathcal{B}\nabla J_{si}(y_i) \le -s_{mi}\|\nabla J_{si}(y_i)\|^2, \tag{43}$$

where s_{mi} is the minimum eigenvalue of the matrix $\mathcal{B}$.

Remark 2. *Herein, the motivation of selecting the cost function $J_{si}(y_i)$ is to obtain the optimal DTC strategy, which can minimize and maximize $J_{si}(y_i)$ under the optimal control law and the worst disturbance law. Moreover, we can discuss the stability of closed-loop systems by the constructed optimal cost function. Besides, just to be clear, $J_{si}(y_i)$ is derived by properly selecting the quadratic polynomial in terms of the state vector. We generally choose $J_{si}(y_i) = 0.5y_i^{\mathsf{T}}y_i$.*

When the condition occurs, that is, $(\nabla J_{si}(y_i))^{\mathsf{T}}[\mathcal{F}_i(y_i) + \mathcal{G}_i(y_i)u_i^*(y_i) + \mathcal{H}_i(y_i)v_i^*(y_i)] > 0$, which means the system is in an unstable state under the optimal control law Equation (36). In this case, an additional term is introduced to ensure the system stability. Based on Equation (36), some processing is performed as follows:

$$\begin{aligned}
&\frac{-\partial[(\nabla J_{si}(y_i))^{\mathsf{T}}(\mathcal{F}_i(y_i) + \mathcal{G}_i(y_i)u_i^*(y_i) + \mathcal{H}_i(y_i)v_i^*(y_i))]}{\partial \hat{w}_{ci}} \\
&= \left(\frac{\partial \hat{u}_i^*(y_i)}{\partial \hat{w}_{ci}}\right)^{\mathsf{T}}\frac{-\partial[(\nabla J_{si}(y_i))^{\mathsf{T}}(\mathcal{F}_i(y_i) + \mathcal{G}_i(y_i)u_i^*(y_i) + \mathcal{H}_i(y_i)v_i^*(y_i))]}{\partial \hat{u}_i^*(y_i)} \\
&= \frac{1}{2}\nabla\sigma_{ci}(y_i)\mathcal{G}_i(y_i)R_i^{-1}\mathcal{G}_i^{\mathsf{T}}(y_i)\nabla J_{si}(y_i).
\end{aligned} \tag{44}$$

Thus, we describe the improved learning rule as

$$\dot{\hat{w}}_{ci} = -\eta_{ci}\frac{\phi_i}{(1+\phi_i^{\mathsf{T}}\phi_i)^2}e_{ci} + \frac{1}{2}\eta_{si}\Pi_i(y_i, \hat{u}_i^*, \hat{v}_i^*)\nabla\sigma_{ci}(y_i)\mathcal{G}_i(y_i)R_i^{-1}\mathcal{G}_i^{\mathsf{T}}(y_i)\nabla J_{si}(y_i), \tag{45}$$

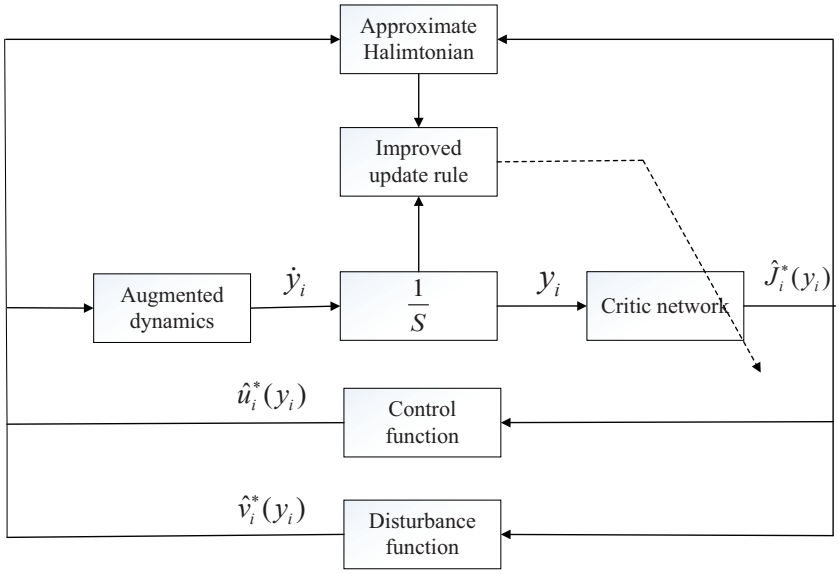

Figure 1. Control structure of the ATIS. ATIS: augmented tracking isolated subsystem.

where $\eta_{si} > 0$ represents the additional learning rate with respect to the stabilising term and $\Pi_i(y_i, \hat{u}_i^*, \hat{v}_i^*)$ stands for the adaptation parameter term that tests the stability of the ATIS. The definition of Π_i is as follows:

$$\Pi_i(y_i, \hat{u}_i^*, \hat{v}_i^*) = \begin{cases} 0, & \text{if } \dot{J}_{si}^*(y_i) < 0, \\ 1, & \text{else.} \end{cases} \tag{46}$$

It is found that when the derivative of $J_{si}(y_i)$ satisfies $\dot{J}_{si}(y_i) < 0$, the latter term of the weight update rule does not play its role so that the update mode is still the traditional normalized steepest descent algorithm. When $\dot{J}_{si}(y_i) > 0$, the latter term of the weight update rule starts to play its role of ensuring the stability, that is, the improved weight update method is adopted. It can be seen that the system can be adjusted to be stable under the improved weight updating criterion. Moreover, in order to clearly highlight that we have achieved the elimination of the initial admissible control law, herein, we set the initial weight vector to zero. Through the new critic learning rule, the structure of the proposed DTC strategy for ATIS is performed in Figure 1.

In accordance to $\dot{\tilde{w}}_{ci} = -\dot{\hat{w}}_{ci}$ and Equation (39), the specific form of $\tilde{w}_{ci}$ is derived. Then, we can convert the estimated weight $\hat{w}_{ci}$ into the form of the weight vector w_{ci} and the error weight vector $\tilde{w}_{ci}$, which can be employed by proving the state y_i and the weight estimation error $\tilde{w}_{ci}$ are UUB for the closed-loop system.

5. SIMULATION EXPERIMENT

In this section, we will introduce the common mechanical vibration system, that is, the spring-mass-damper system. The structural diagram of the mechanical system is shown in Figure 2. From it, M_1 and M_2 denote the mass of two objects, K_1, K_2, and K_3 represent the stiffness constants of three springs. C_1, C_2, and C_3 stand for the damping, respectively.

In addition, let P_i, V_i, F_i, and f_{μ_i} be the position, the velocity, the force, and the friction applied to the object, where $i = 1, 2$. Hence, the system dynamics for M_1 and M_2 are as follows:

$$\dot{P}_1 = V_1, \tag{47}$$

$$M_1\dot{V}_1 = -K_1P_1 - C_1V_1 + K_2(P_2 - P_1) + C_2(V_2 - V_1) + F_1 - f_{\mu_1}, \tag{48}$$

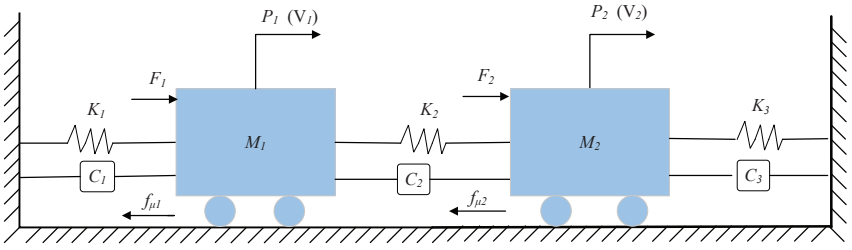

Figure 2. Simple diagram of the interconnected mass-spring-damper system.

$$\dot{P}_2 = V_2, \tag{49}$$

$$M_2\dot{V}_2 = -K_3P_2 - C_3V_2 + K_2\left(P_1 - P_2\right) + C_2\left(V_1 - V_2\right) + F_2 - f_{\mu_2}. \tag{50}$$

For the object M_1, we define $x_{11} = P_1, x_{12} = V_1, \bar{u}_1(x_1) = F_1$, and $v_1(x_1) = f_{\mu_1}$. In the same way, we let $x_{21} = P_2$, $x_{22} = V_2$, $\bar{u}_2(x_2) = F_2$, and $v_2(x_2) = f_{\mu_2}$ for the object M_2. Next, the state-space of the spring-mass-damper system is written as

$$\dot{x}_1 = \begin{bmatrix} \dot{x}_{11} \\ \dot{x}_{12} \end{bmatrix} = \begin{bmatrix} x_{12} \\ -\frac{K_1}{M_1}x_{11} - \frac{C_1}{M_1}x_{12} \end{bmatrix} + \begin{bmatrix} 0 \\ \frac{1}{M_1} \end{bmatrix}\left(\bar{u}_1\left(x_1\right) + Z_1(x)\right) + \begin{bmatrix} 0 \\ -\frac{1}{M_1} \end{bmatrix} v_1\left(x_1\right) \tag{51}$$

and

$$\dot{x}_2 = \begin{bmatrix} \dot{x}_{21} \\ \dot{x}_{22} \end{bmatrix} = \begin{bmatrix} x_{22} \\ -\frac{K_3}{M_2}x_{21} - \frac{C_3}{M_2}x_{22} \end{bmatrix} + \begin{bmatrix} 0 \\ \frac{1}{M_2} \end{bmatrix}\left(\bar{u}_2\left(x_2\right) + Z_2(x)\right) + \begin{bmatrix} 0 \\ -\frac{1}{M_2} \end{bmatrix} v_2\left(x_2\right), \tag{52}$$

where $x_1 = [x_{11}, x_{12}]^{\mathsf{T}} \in \mathbb{R}^2$ and $x_2 = [x_{21}, x_{22}]^{\mathsf{T}} \in \mathbb{R}^2$ are system states. $\bar{u}_1(x_1) \in \mathbb{R}$, $\bar{u}_2(x_2) \in \mathbb{R}$, $v_1(x_1) \in \mathbb{R}$, and $v_2(x_2) \in \mathbb{R}$ are control inputs and disturbance inputs of the subsystem 1 and the subsystem 2, respectively. Simultaneously, $Z_1(x) = K_2\left(x_{21} - x_{11}\right) + C_2\left(x_{22} - x_{12}\right)$ and $Z_2(x) = K_2\left(x_{11} - x_{21}\right) + C_2\left(x_{12} - x_{22}\right)$, which indicates the spring K_2 and the damping C_2 play a connecting role for two subsystems. Herein, we let $\theta_1(x_1) = ||x_1||$ and $\theta_2(x_2) = |x_{22}|$. Besides, we choose $\beta_{11} = \beta_{12} = 1$, $\beta_{21} = \beta_{22} = 1/2$, and $\mu_1 = \mu_2 = 1$. Moreover, we select $\lambda_1 = \lambda_2 = 0.6$, $\varrho_1 = \varrho_2 = 1$, $R_1 = R_2 = 2$, and $Q_1 = Q_2 = 2I_4$, where I_4 is the four-dimensional identity matrix. Above all, the desired reference trajectories r_1 and r_2 for two subsystems are generated by the following command system:

$$\dot{r}_i = \begin{bmatrix} \dot{r}_{i1} \\ \dot{r}_{i2} \end{bmatrix} = \begin{bmatrix} -0.5r_{i1} - 0.5r_{i2}\cos\left(r_{i1}\right) \\ \sin\left(r_{i1}\right) - 0.5r_{i2} \end{bmatrix}, \quad i = 1, 2, \tag{53}$$

where $r_1 = [r_{11}, r_{12}]^{\mathsf{T}} \in \mathbb{R}^2$ and $r_2 = [r_{21}, r_{22}]^{\mathsf{T}} \in \mathbb{R}^2$ are reference states. Then, we define the tracking errors as $e_{i1} = x_{i1} - r_{i1}$ and $e_{i2} = x_{i2} - r_{i2}$. Hence, the augmented state vector can be expressed as $y_i = [y_{i1}, y_{i2}, y_{i3}, y_{i4}]^{\mathsf{T}} = [e_{i1}, e_{i2}, r_{i1}, r_{i2}]^{\mathsf{T}}$, $i = 1, 2$. We set practical parameters as $M_1 = 1$kg, $K_1 = 3$N/m, and $C_1 = 0.5$Ns/m for the subsystem 1. Similarly, we let $M_2 = 2$kg, $K_3 = 5$N/m, and $C_3 = 1$Ns/m for the subsystem 2. Considering Equations (51-53), the augmented system dynamics $\dot{y}_1$ and $\dot{y}_2$ can be obtained in the following forms:

$$\dot{y}_1 = \begin{bmatrix} r_{12} + e_{12} + 0.5r_{11} + 0.5r_{12}\cos\left(r_{11}\right) \\ -3(r_{11} + e_{11}) - 0.5(r_{12} + e_{12}) - \sin\left(r_{11}\right) + 0.5r_{12} \\ -0.5r_{11} - 0.5r_{12}\cos\left(r_{11}\right) \\ \sin\left(r_{11}\right) - 0.5r_{12} \end{bmatrix} + \begin{bmatrix} 0 \\ 1 \\ 0 \\ 0 \end{bmatrix}\bar{u}_1\left(y_1\right) + \begin{bmatrix} 0 \\ -1 \\ 0 \\ 0 \end{bmatrix} v_1\left(y_1\right) \tag{54}$$

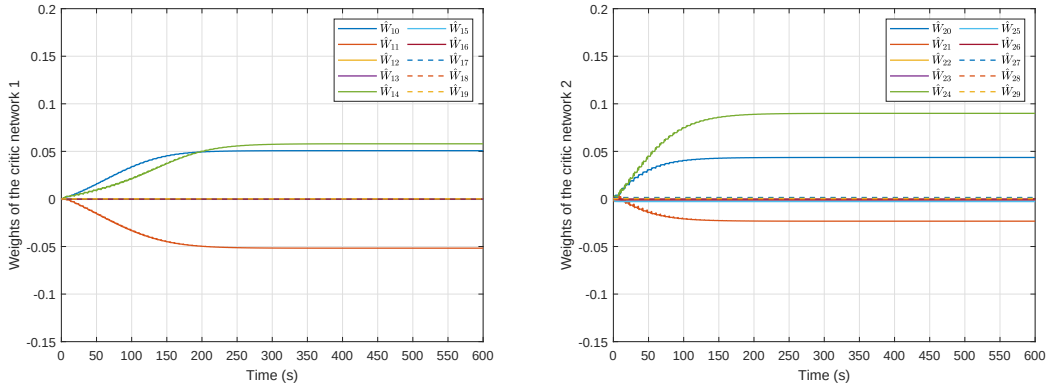

Figure 3. Weights convergence process of the critic network 1 and the critic network 2.

and

$$\dot{y}_2 = \begin{bmatrix} r_{22} + e_{22} + 0.5r_{21} + 0.5r_{22}\cos(r_{21}) \\ -2.5(r_{21} + e_{21}) - 0.5(r_{22} + e_{22}) - \sin(r_{21}) + 0.5r_{22} \\ -0.5r_{21} - 0.5r_{22}\cos(r_{21}) \\ \sin(r_{21}) - 0.5r_{22} \end{bmatrix} + \begin{bmatrix} 0 \\ 0.5 \\ 0 \\ 0 \end{bmatrix} \bar{u}_2(y_2) + \begin{bmatrix} 0 \\ -0.5 \\ 0 \\ 0 \end{bmatrix} v_2(y_2). \quad (55)$$

Based on the online ADP algorithm, two critic networks are constructed as follows:

$$\begin{aligned} \hat{J}_1^*(y_1) = {} & \hat{w}_{10}y_{11}^2 + \hat{w}_{11}y_{11}y_{12} + \hat{w}_{12}y_{11}y_{13} + \hat{w}_{13}y_{11}y_{14} + \hat{w}_{14}y_{12}^2 \\ & + \hat{w}_{15}y_{12}y_{13} + \hat{w}_{16}y_{12}y_{14} + \hat{w}_{17}y_{13}^2 + \hat{w}_{18}y_{13}y_{14} + \hat{w}_{19}y_{14}^2 \end{aligned} \quad (56)$$

and

$$\begin{aligned} \hat{J}_2^*(y_2) = {} & \hat{w}_{20}y_{21}^2 + \hat{w}_{21}y_{21}y_{22} + \hat{w}_{22}y_{21}y_{23} + \hat{w}_{23}y_{21}y_{24} + \hat{w}_{24}y_{22}^2 \\ & + \hat{w}_{25}y_{22}y_{23} + \hat{w}_{26}y_{22}y_{24} + \hat{w}_{27}y_{23}^2 + \hat{w}_{28}y_{23}y_{24} + \hat{w}_{29}y_{24}^2. \end{aligned} \quad (57)$$

During the online learning process, we take basic learning rates and additional learning rates as $\eta_{c1} = 0.01$, $\eta_{c2} = 0.03$ as well as $\eta_{s1} = \eta_{s2} = 0.01$. Let initial system states and reference states be $x_{10} = [1.5, 0]^\mathsf{T}$, $x_{20} = [1, -1]^\mathsf{T}$, and $r_{10} = r_{20} = [0.5, -0.5]^\mathsf{T}$, respectively. Therefore, initial states of the ATIS are $y_{10} = [1, 0.5, 0.5, -0.5]^\mathsf{T}$ and $y_{20} = [0.5, -0.5, 0.5, -0.5]^\mathsf{T}$.

Herein, two probing noises are added within the beginning 400 steps to keep the persistence of excitation condition of the ATIS. The weight convergence curves are shown in Figure 3. It can be seen that the weight has converged to a certain numerical value before turning off the excitation condition, which confirms the validity of the improved weight update algorithm. Form it, we find the initial weights are selected as zero, which indicates the initial admissible control is eliminated.

Next, in order to make the system achieve the purpose of the optimal tracking, feedback gains are selected as $k_1 = k_2 = 1$. Then, the DTC strategy $\{k_1\hat{u}_1^*(y_1), k_2\hat{u}_2^*(y_2)\}$ can be derived from the obtained weight vector for the spring-mass-damper interconnected system. In addition, the evolution curves are shown in Figure 4, which displays the tracking control inputs and disturbance inputs for the subsystem 1 and the subsystem 2. Then, the obtained DTC strategy is applied to the controlled system for 50 s, and its tracking error trajectory curves are displayed in Figure 5. It is obvious that the tracking error curves are eventually enforced to the origin. Taken together, this simulation result verifies the effectiveness of the proposed DTC strategy.

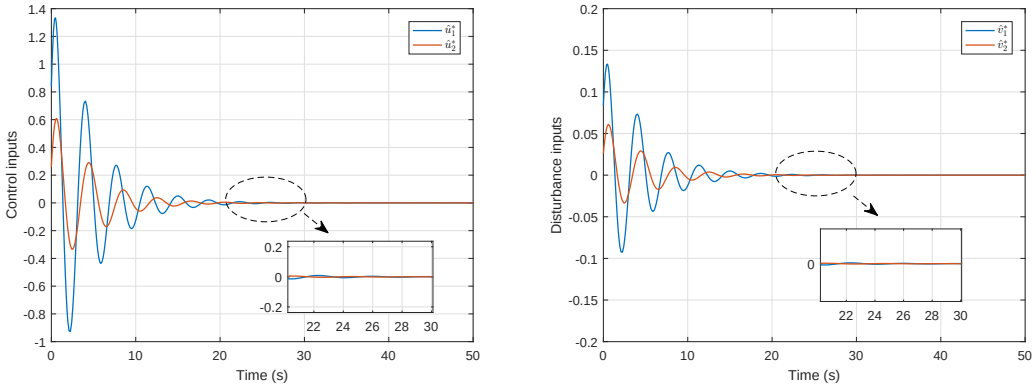

Figure 4. Tracking control inputs and disturbance inputs for subsystem 1 and subsystem 2

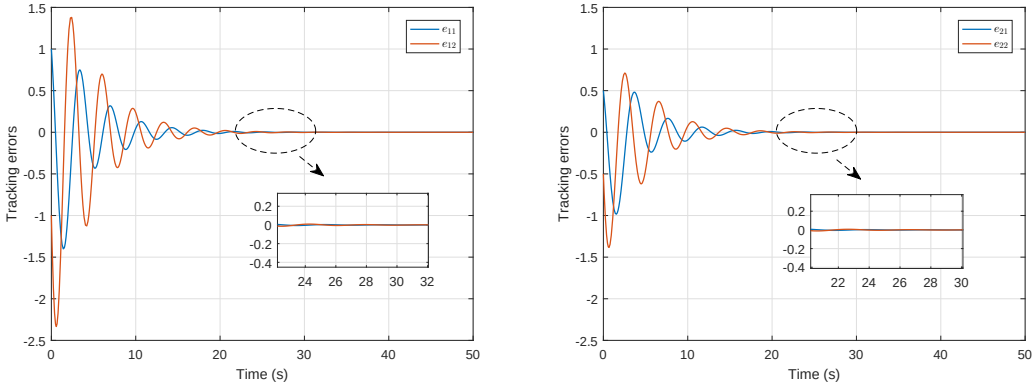

Figure 5. Tracking error trajectories for subsystem 1 and subsystem 2.

6. CONCLUSION

In this paper, the optimal DTC strategy for CT nonlinear large-scale systems with external disturbances is proposed by employing the ADP algorithm. The approximate optimal control law of the ATISs can achieve the trajectory tracking goal. Then, the establishment of the DTC strategy is derived by adding the appropriate feedback gain, whose feasibility has been proved via the Lyapunov theory. Note that all the above-mentioned results are investigated by considering a cost function with the discount. Then, only a series of single critic networks are employed to solve HJI equations of N ATISs, so that we acquire the approximate optimal control law and the worst disturbance law. In addition, the stability term added in the weight updating process avoids the selection of the initial stable control policy. Furthermore, the simulation results are displayed for the spring-mass-damper system to indicate the validity of the proposed DTC method. In the future, we will utilize more advanced methods to deal with the DTC problem for nonaffine systems. Besides, we can also consider the unmatched interconnected relationship for the DTC problem, which is a considerable direction of improved research.

DECLARATIONS

Authors' contributions

Made significant contributions to the conception and experiments: Fan W, Wang D
Made significant contributions to the writing: Fan W, Wang D
Made substantial contributions to the revision and translation: Liu A, Wang D

Availability of data and materials
Not applicable

Financial support and sponsorship
This work was supported in part by the National Natural Science Foundation of China (No. 62222301; No. 61890930-5 and No. 62021003); in part by the National Key Research and Development Program of China (No. 2021ZD0112302; No. 2021ZD0112301 and No. 2018YFC1900800-5); and in part by the Beijing Natural Science Foundation (No. JQ19013).

Conflicts of interest
All authors declared that there are no conflicts of interest.

Ethical approval and consent to participate
Not applicable.

Consent for publication
Not applicable.

REFERENCES
1. Saberi A. On optimality of decentralized control for a class of nonlinear interconnected systems. *Automatica* 1988;24:1101–4. DOI
2. Mu CX, Sun CY, Wang D, Song AG, Qian CS. Decentralized adaptive optimal stabilization of nonlinear systems with matched interconnections. *Soft Comput* 2018;22:82705–15. DOI
3. Mehraeen S, Jagannathan S. Decentralized optimal control of a class of interconnected nonlinear discrete-time systems by using online Hamilton-Jacobi-Bellman formulation. *IEEE Trans Neural Netw* 2011;22:111715–96. DOI
4. Yang X, He HB. Adaptive dynamic programming for decentralized stabilization of uncertain nonlinear large-scale systems with mismatched interconnections. *IEEE Trans Syst Man Cybern Syst* 2020;50:82870–82. DOI
5. Karimi HR. How to deal with the complexity in robotic systems? *Complex Eng Syst* 2022;2:15. DOI
6. Xu Q, Yu C, Yuan X, Fu Z, Liu H. A distributed electricity energy trading strategy under energy shortage environment. *Complex Eng Syst* 2022;2:14. DOI
7. Bian T, Jiang Y, Jiang ZP. Decentralized adaptive optimal control of large-scale systems with application to power systems. *IEEE Trans Ind Electron* 2015;62:42439–47. DOI
8. Liu DR, Wang D, Li HL. Decentralized stabilization for a class of continuous-time nonlinear interconnected systems using online learning optimal control approach. *IEEE Trans Neural Netw Learn Syst* 2014;25:2418–28. DOI
9. Sun KK, Sui S, Tong SC. Fuzzy adaptive decentralized optimal control for strict feedback nonlinear large-scale systems. *IEEE Trans Cybern* 2018;48:41326–39. DOI
10. Wang XM, Feng ZG, Zhang GJ, Niu B, Yang D, et al. Adaptive decentralised control for large-scale non-linear non-strict-feedback interconnected systems with time-varying asymmetric output constraints and dead-zone inputs. *IET Control Theory & Appl* 2020;14:203417–27. DOI
11. Wei QL, Liu DR, Lin Q, Song RZ. Discrete-time optimal control via local policy iteration adaptive dynamic programming. *IEEE Trans Cybern* 2017;47:103367–79. DOI
12. Wang D, Ren J, Ha MM, Qiao JF. System stability of learning-based linear optimal control with general discounted value iteration. *IEEE Trans Neural Netw Learn Syst* 2022. DOI
13. Wang D, Ha MM, Zhao MM. The intelligent critic framework for advanced optimal control. *Artif Intell Rev* 2022;55:11–22. DOI
14. Wang D, Qiao JF, Cheng L. An approximate neuro-optimal solution of discounted guaranteed cost control design. *IEEE Trans Cybern* 2022;52:177–86. DOI
15. Li YM, Liu YJ, Tong SC. Observer-based neuro-adaptive optimized control of strict-feedback nonlinear systems with state constraints. *IEEE Trans Neural Netw Learn Syst* 2022;33:73131–45. DOI
16. Wang H, Yang CY, Liu XM, Zhou LN. Neural-network-based adaptive control of uncertain MIMO singularly perturbed systems with full-state constraints. *IEEE Trans Neural Netw Learn Syst* 2021. DOI
17. Zhang H, Hong QQ, Yan HC, Yang FW, Guo G. Event-based distributed H-infinity filtering networks of 2-DOF quarter-car suspension systems. *IEEE Trans Ind Inform* 2017;13:1312–21. DOI
18. Chen YG, Fei SM, Li YM. Robust stabilization for uncertain saturated time-delay systems: A distributed-delay-dependent polytopic

approach. *IEEE Trans Automat Contr* 2017;62:73455–60. DOI
19. Chen YG, Wang ZD. Local stabilization for discrete-time systems with distributed state delay and fast-varying input delay under actuator saturations. *IEEE Trans Automat Contr* 2021;66:31337–44. DOI
20. Fu H, Chen X, Wu M. Distributed optimal observer design of networked systems via adaptive critic design. *IEEE Trans Syst Man Cybern Syst* 2021;51:116976–85. DOI
21. Narayanan V, Jagannathan S. Event-triggered distributed control of nonlinear interconnected systems using online reinforcement learning with exploration. *IEEE Trans Cybern* 2018;48:92510–9. DOI
22. Wang D, Zhao MM, Ha MM, Qiao JF. Intelligent optimal tracking with application verifications via discounted generalized value iteration. *Acta Automatica Sinica* 2022;48:1182–93. DOI
23. Zhang HG, Zhang K, Cai YL, Han J. Adaptive fuzzy fault-tolerant tracking control for partially unknown systems with actuator faults via integral reinforcement learning method. *IEEE Trans Fuzzy Syst* 2019;27:101986–98. DOI
24. Modares H, Lewis FL. Optimal tracking control of nonlinear partially-unknown constrained-input systems using integral reinforcement learning. *Automatica* 2014;50:71780–1792. DOI
25. Ha MM, Wang D, Liu DR. Discounted iterative adaptive critic designs with novel stability analysis for tracking control. *IEEE/CAA Journal of Automat Sinica* 2022;9:71262–1272. DOI
26. Qu QX, Zhang HG, Feng T, Jiang H. Decentralized adaptive tracking control scheme for nonlinear large-scale interconnected systems via adaptive dynamic programming. *Neurocomputing* 2017;225:1–10. DOI
27. Niu B, Liu JD, Wang D, Zhao XD, Wang HQ. Adaptive decentralized asymptotic tracking control for large-scale nonlinear systems with unknown strong interconnections. *IEEE/CAA Journal of Automatica Sinica* 2022;9:1173–86. DOI
28. Liu JD, Niu B, Kao YG, Zhao P, Yang D. Decentralized adaptive command filtered neural tracking control of large-scale nonlinear systems: An almost fast finite-time framework. *IEEE Trans Neural Netw Learn Syst* 2021;32:83621–2. DOI
29. Tong SC, Zhang LL, Li YM. Observed-based adaptive fuzzy decentralized tracking control for switched uncertain nonlinear large-scale systems with dead zones. *IEEE Trans Syst Man Cybern Syst* 2016;46:137–47. DOI
30. Wang D, Hu LZ, Zhao MM, Qiao JF. Dual event-triggered constrained control through adaptive critic for discrete-time zero-sum games. *IEEE Trans Syst Man Cybern Syst* 2023;53:31584–9. DOI
31. Li XM, Zhang B, Li PS, Zhou Q, Lu RQ. Finite-horizon H-infinity state estimation for periodic neural networks over fading channels. *IEEE Trans Neural Netw Learn Syst* 2020;31:51450–60. DOI
32. Duan JJ, Xu H, Liu WX, Peng JC, Jiang H. Zero-sum game based cooperative control for onboard pulsed power load accommodation. *IEEE Trans Ind Inform* 2020;16:1238–47. DOI
33. Wang D, Zhao MM, Ha MM, Qiao JF. Stability and admissibility analysis for zero-sum games under general value iteration formulation. *IEEE Trans Neural Netw Learn Syst* 2022. DOI
34. Zhang HG, Cui XH, Luo YH, Jiang H. Finite-horizon H-infinity tracking control for unknown nonlinear systems with saturating actuators. *IEEE Trans Neural Netw Learn Syst* 2018;29:41200–12. DOI
35. Modares H, Lewis FL, Jiang ZP, H-infinity tracking control of completely unknown continuous-time systems via off-policy reinforcement learning. *IEEE Trans Neural Netw Learn Syst* 2015;26:102550–62. DOI
36. Hou JX, Wang D, Liu DR, Zhang Y. Model-free H-infinity optimal tracking control of constrained nonlinear systems via an iterative adaptive learning algorithm. *IEEE Trans Syst Man Cybern Syst* 2020;50:114097–108. DOI

Ernest *et al*. *Complex Eng Syst* 2023;3:4
DOI: 10.20517/ces.2022.54

Complex Engineering Systems

Research Article

Open Access

Formal verification of Fuzzy-based XAI for Strategic Combat Game

Nicholas Ernest, Timothy Arnett, Zachariah Phillips

Thales Avionics Inc., Cincinnati, OH 45242, USA.

Correspondence to: Dr. Nicholas Ernest, Thales Avionics Inc., 4358 Glendale-Milford Rd., Cincinnati, OH 45242, USA. E-mail: nick.ernest@us.thalesgroup.com

How to cite this article: Ernest N, Arnett T, Phillips Z. Formal verification of Fuzzy-based XAI for Strategic Combat Game. *Complex Eng Syst* 2023;3:4. http://dx.doi.org/10.20517/ces.2022.54

Received: 11 Dec 2022 **First Decision:** 31 Jan 2023 **Revised:** 13 Mar 2023 **Accepted:** 14 Mar 2023 **Published:** 30 Mar 2023

Academic Editor: Hamid Reza Karimi **Copy Editor:** Yin Han **Production Editor:** Yin Han

Abstract

Explainable AI is a topic at the forefront of the field currently for reasons involving human trust in AI, correctness, auditing, knowledge transfer, and regulation. AI that is developed with reinforcement learning (RL) is especially of interest due to the non-transparency of what was learned from the environment. RL AI systems have been shown to be "brittle" with respect to the conditions it can safely operate in, and therefore ways to show correctness regardless of input values are of key interest. One way to show correctness is to verify the system using Formal Methods, known as Formal Verification. These methods are valuable, but costly and difficult to implement, leading most to instead favor other methodologies for verification that may be less rigorous, but more easily implemented. In this work, we show methods for development of an RL AI system for aspects of the strategic combat game *Starcraft 2* that is performant, explainable, and formally verifiable. The resulting system performs very well on example scenarios while retaining explainability of its actions to a human operator or designer. In addition, it is shown to adhere to formal safety specifications about its behavior.

Keywords: Explainable AI, reinforcement learning, formal verification, starcraft, genetic algorithm, fuzzy logic, genetic fuzzy trees, formal methods

1. INTRODUCTION

Artificial intelligence (AI) applications in reinforcement learning (RL) have garnered significant attention in recent years[1,2] due to their wide ranging applicability to previously intractable problems. In particular, the success of DeepMind's AlphaGo system[3] ignited a revitalization of research and attention in the area, specifically with the introduction of new techniques combining RL with deep neural networks (DNN), known as Deep Reinforcement Learning (DRL). However, while improvements within the overarching field of RL and DRL continue to increase the scalability and performance of these approaches, verification and explainability efforts have not received comparable attention. There have been efforts to take highly performant DRL solutions and increase explainability and trustworthiness *ex post facto*. An example of this was DARPA's XAI program, introduced to study and identify the importance and usage of explainability in AI[4]. Their conclusions were that many DRL solutions were brittle, unverifiable, and opaque to human designers/operators that may want to audit, verify, or extract knowledge from what the agent learned.

Fuzzy inference systems (FIS), function approximators that utilize Fuzzy Logic and inference rules to map inputs to outputs[5], have several properties that lend themselves towards XAI, but have other potential drawbacks compared to DNNs, namely scalability. Fuzzy Logic-based systems have long been used in control system development due to their approximation capabilities[6], ease of implementation from expert knowledge[7], robustness to input noise[8], explainability and transparency to humans[9], and ability to be formally verified[10]. However, scalability issues with respect to the number of inputs limited the potential applications. Fuzzy trees were introduced in 2015[11] in order to mitigate scalability issues while also retaining explainability and approximation capabilities by combining multiple FISs arranged in a network or tree-like structure.

Genetic Algorithms are a class of gradient-free search algorithms that evolve solutions by mutation and recombination over a number of generations by evaluating their *fitness* against one or more metrics in a *fitness function*. GAs have long been used to great effect in many areas, but also in a large body of work related to optimization of FIS parameters[12]. Combining Fuzzy Trees with Genetic Algorithms led to Genetic Fuzzy Trees (GFTs)[11], a powerful combination that uses an explainable and formally verifiable function approximator with a gradient-free optimizer and has been applied to several complex use cases in both supervised[13] and reinforcement learning domains[14]. Thales's GFT software toolkit includes both a Fuzzy Logic engine, Psion, and a state-of-the-art Genetic Algorithm-based optimization tool, EVE[15]. Its strengths include ease of utilization for finding low wall-time solutions and wide applicability due to the nature of gradient-free optimization. Perhaps the most notable prior use-case was the Alpha system[14], a super-human AI for beyond visual range air-to-air engagements within high-fidelity simulations against expert human pilots[14].

Another benefit of GFTs is that they can be verified using Formal Methods. Formal Methods are often defined as "mathematically rigorous techniques for the development, specification, and verification of systems." Many methods and techniques fall under the umbrella of Formal Methods including the boolean satisfiability problem (SAT)[16], satisfiability modulo theories (SMT), model checking, theorem proving, reachability analysis, etc. Formal Verification is the utilization of Formal Methods towards verifying the correctness of a system. In general, verification is about confidence in the correctness of a system, and formal verification extends traditional verification methods (e.g., Monte Carlo evaluation) towards definitive proofs of correctness. The adoption of formal verification has been slow in the world of AI and ML mainly due to the difficulty in proving properties of DNNs as their scale continues to increase.

In this work, an AI agent using the GFT construct is created and then trained using reinforcement learning to play specific scenarios within StarCraft 2. Note that this study does not analyze an entire standard Starcraft 2 match. Instead, the focus will be on specific control applications with a focus on explainability and formal verifiability, though an entire standard game of Starcraft 2 could certainly be studied through utilization of the GFT approach. This study is not aimed towards demonstrating a performance disparity between Fuzzy logic-

based AI approaches and any other methodology, but rather to demonstrate how these systems can be created in a way that maintains explainability and formal verifiability. These capabilities are highly desired, and often required, for mission/safety-critical applications. Starcraft 2 is used because it is a commonly used environment in modern RL research, it allows for creation of publicly-shareable mission/safety-critical use-cases, and allows for extension of this work for comparisons with other highly performant RL methodologies.

The GFT is initialized with a structure, given initial parameter values where applicable, and then trained by interaction in the game across a training set of episodes. The structure of the GFT is such that output actions can be explained by extracting the activated rules and membership functions. Specifications about the system's behavior are then created and verified against the system using Formal Methods[17]. In cases where the specifications are violated, counterexamples are returned showing where the violations occur, and then corrections are performed. The corrected systems are then verified to not violate specifications showing definitive correctness with respect to the developed behavioral specifications.

Four specifications have been developed for this study, which is by no means an exhaustive potential set. This work will demonstrate the learning capability to solve a particularly difficult sort of engagement, demonstrate the potential explainability possibilities, and prove adherence to a set of relevant specifications. The primary objective for this study is to showcase an example of a fuzzy logic based AI system which can be formally verified to adhere to safety specifications within a mission/safety-critical scenario.

The structure of the remainder of the paper is as follows. Section 2 details the methods used to create, train, and verify a GFT for specific scenarios in SC2. Section 3 shows the results including RL training, verification against specifications (and generated counterexamples), and results after modification to ensure specification adherence. Section 4 discusses the results in depth and offers thoughts on extensions and future work. Finally, Section 5 gives a concise conclusion on the work, results, and impact of this study.

2. METHODS

This section describes both the general background info and setup of a GFT solution for training in a RL context followed by the specific implementation for the SC2 use case.

2.1. General GFT workflow

The typical workflow for creating a GFT AI solution involves creating a GFT-based agent with a tree structure that is purposefully designed such that it is explainable and formally verifiable. The performance of the agent is evaluated through a number of different scenarios for training, testing, and validation. The system is then formally verified against specifications about its behavior. Explainability aspects are used both as an auditing tool when evaluating counterexamples from the formal verification process, and also as a knowledge transfer device to allow human observation and understanding of what the agent learned during the RL process.

GFTs are most often created using a combination of initial expert knowledge and machine learning using gradient-free optimization. Thales's GFT toolkit is a commercial software package that includes both a Fuzzy Inference System (FIS) engine named Psion and a Genetic Algorithm optimization engine, EVE, which combined represent the best software implementation of Genetic Fuzzy Trees available today[15]. An example of a notional GFT structure is shown in Figure 1.

The GFT is then trained using EVE in whatever context the problem is framed (supervised, reinforcment) until termination criteria are met. These termination criteria can include performance metrics, time, number of generations/epochs, stagnation measures, etc. Once this round of training is complete, verification can occur on the GFT (fixed parameters) along with SME/developer auditing and manual changes. Counterexamples

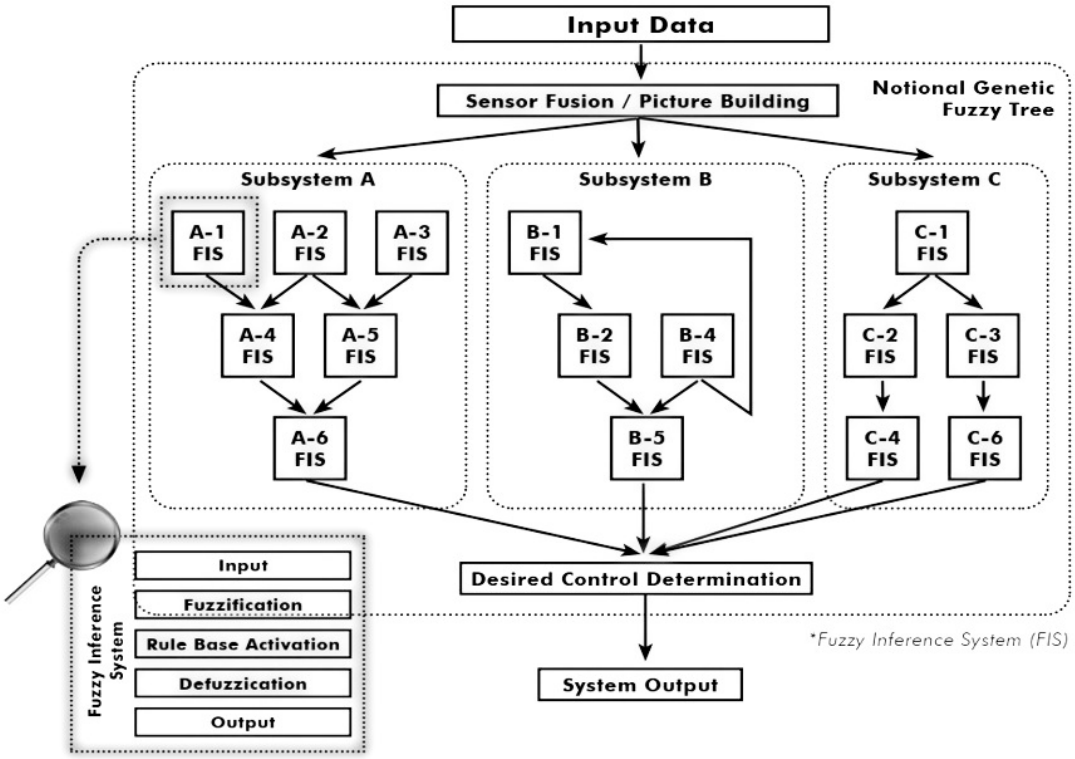

Figure 1. Notional figure of a GFT structure, with a plurality of FIS nodes.

from the verification process can be used to directly change aspects of the GFT, or inform the ML process in the form of constraints, reward modifications, etc. The GFT can then be reinitialized and trained using the ML process again. This process iterates until system requirements are met.

2.1.1. Initial GFT structure

The GFT structure is primarily defined through the input/output flow of each FIS node within the system. Although a GFT structure can be initialized randomly and optimized through EVE, it is often advantageous to initialize using domain knowledge where possible. This is beneficial for two main reasons:

1. It takes advantage of domain knowledge as an initial seeding to use as a starting point. This provides a valuable baseline that can then be expanded/improved upon
2. Depending on methods used, can preserve semantic relationships/importance in the structure itself due to the linguistic nature of FISs and the connections between them in the tree

Note that these are not strictly necessary for explainability or performance, but often lead to shorter project development times and improve transparency/understandability [18]. Assuming a manual structure is provided, the learning agent can be left to optimize all of the Membership Functions (MFs) and Rule-Bases (RBs) of the FISs, either holistically or individually.

2.1.2. GFT RL training

Due to the gradient-free algorithms used for the training process, the methods used for both supervised and reinforcement learning problems are largely the same with the difference being in the formulation of the fitness function. Where in a supervised learning problem the fitness function may be a measure of the fit of the function to the underlying data (LMS, cross entropy, etc.), in RL use cases the fitness is often a measure of how well the agent performed in one or more simulated episodes, or *scenarios*. The resulting fitness score is used

to evolve the population of candidate GFT solutions until termination criteria are met.

After some amount of training, a fixed configuration for the GFT architecture is evaluated, tested, and verified. Additional numerical testing is often performed along with unit tests, formal verification, and human inspection and correction. If counterexamples to formal specifications are found, they are often mitigated through direct designer input, or added to the RL process in such a way to penalize GFT configurations in the GA population that have such violations. This iterative process continues until adherence to all specifications and requirements is achieved and performance metrics are met.

2.1.3. Formal verification

As mentioned in Section 2.1.2, the process for verifying a GFT involves taking a GFT with a particular configuration (fixed structure, parameters, etc.) and evaluating it against formal specifications about its behavior. These specifications are often derived from system requirements, but can also be created from sources such as numeral/simulation-based test results, rules of engagement or other high level behavioral constraints, certification standard criteria, etc. The specifications are then translated from natural language to a formal language using mathematical logic in order to be encoded for formal methods analysis. The formal languages used depend on the necessary expressiveness of the language based on the specification itself. Some of these languages include Propositional Logic, First Order Logic (FOL), and temporal logics such as Linear Temporal Logic, Computational Tree Logic, etc. Many others could be used depending on the use case and formulation of the specifications and models, and Thales GFTs have been implemented with a number of these methods, most commonly FOL and LTL.

Models of the GFT are then translated to formal verification tools such as SMT solvers and model checkers, and then checked against the specifications. If counterexamples are found, modification of the GFT is performed by the designer and/or the ML process. The tools used in this work are the state-of-the-art SMT solver Z3 [19] along with the infinite state model checker jKIND [20].

2.2. Starcraft 2 GFT development

The development process for the SC2 use case is largely the same as the general process described in Section 2.1. An initial GFT is constructed for parts of agent control based on expert knowledge, it is trained using gradient-free RL in the SC2 environment, formal verification is performed and modifications are made based on counterexamples generated, and then iterated until a performant, specification compliant GFT is found.

2.2.1. StarCraft 2 information

As this study is focusing on specific scenarios for demonstrating the explainability and formal verifiability of this capability, we only consider four different unit types within this context:

- **Marine:** A basic human infantry unit which can fire a ranged volley at a certain frequency. Has an advanced technique Starcraft 2 players can utilize in which if they perform rapid movement commands between volleys, they can both re-position slightly as well as fire faster, outputting more damage per second.
- **Medivac:** A human air vehicle which can utilize a limited resource pool to support ground biological units, such as marines, by healing their durability at a set amount per second. Can also be utilized to transport units, though this capability will not be utilized within the context of this study.
- **Siege Tank:** A human ground vehicle, which can move and attack ground units normally. In ”siege mode” the tank becomes stationary, but can attack further and do increased damage per shot, but cannot attack units within a short range of it. Most interestingly for this study, this unit is one of the few that does ”splash damage” that includes friendly units. That is, friendly units near the target will take damage within a certain range. As such, the siege tanks within this study will always be in ”siege mode”.
- **Zergling:** An alien (Zerg) insect unit that is a fast melee attacker. Can not attack air units but can quickly overwhelm ground units. Will serve as the hostile unit type for this study.

Figure 2. Primary scenario to be utilized for training and analysis. Consists of a stronger zergling force within close range of the human force. Pictured (1) siege tank, (2) medivac, (3) marines, (4) zerglings.

A primary training scenario has been developed which will be utilized for reinforcement learning for a difficult engagement made up of these units. A plurality of other engagements have been developed for testing and formal verification.

From a raw performance perspective, the mission shown in Figure 2 is the primary performance objective to complete. This mission has 16 zerglings that make up the hostile forces as well as 6 marines, 1 medivac, and 1 siege tank on the friendly team.

This mission is such that if the in-game controllers for both forces behave natively, the human ground forces lose with on average at least 7 of the zerglings still alive. This mission is feasible for a human to complete with some forces remaining, but is very difficult and requires advanced tactics within the game. Despite expertise in the game, the standard ending with manual full focus on controlling the human forces has notable losses.

2.2.2. Tree structure creation

A GFT has been created to control these 3 specific types of human units, both individually or as an entire force. The general approach for these sorts of control problems is to generate an entire action plan each time step of the environment. As such, the GFT utilized within this study will provide significantly higher action throughput than what would be maintained by a human.

Through subject matter expertise within this type of engagement, we understand that there are a few key control decisions that need to be made each time step:

- **The Medivac** should make healing decisions that efficiently utilize its resources and keeps biological units alive as best as possible.
- **The Marines** must be intelligent in how they spread their fire against the incoming group of targets, focusing fire to eliminate enemy units efficiently.
- **The Marines** optimally will utilize the ”stutter step” strategy, both to increase their effective attack speed as well as to potentially minimize the total incoming damage from the enemy melee units.
- **The Siege Tank** is a powerful unit and should attempt to get as many effective shots off, while minimizing the harm it does to friendly units.

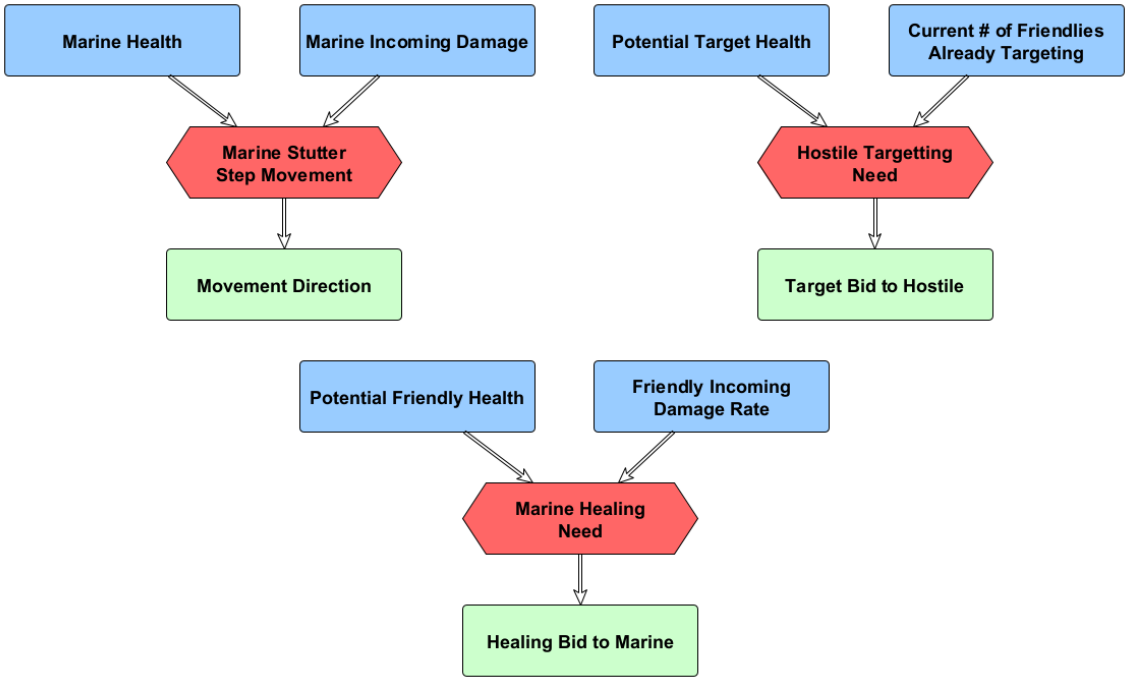

Figure 3. Three standalone FISs for Marine Movement Control, Marine Firing Control, and Medivac Healing Control utilized within the studied model. Normalized inputs in blue, FISs in red, and normalized outputs in green.

A relatively simple FIS structure can accommodate these considerations, with all but the Siege Tank control defined as an output of a single FIS with minimal additional algorithmic work. In Figure 3 these individual FIS nodes are displayed, each being 2-input Mamdani FISs[21].

Specifically, the Marine Stutter Step Movement control will define a relative movement direction to threats based upon both the marines current health, as well as its incoming damage rate from hostiles. The Marine Firing control has a FIS which outputs a bid, from 0% to 100% to select a certain hostile target at every time a shot is available. The potential hostile target with the highest bid is then selected for the marine to attack. This bidding FIS takes in the normalized health of a potential target, as well as the relative quantity of already assigned attacks against this target. The medivac Healing control utilizes a similar approach, considering each friendly unit it can heal and selecting to heal the unit with its highest priority. This priority being determined based upon the normalized health of each marine, and its relative incoming damage rate.

The control for the siege tank's firing logic is more complex and therefore is made up of 3 FIS nodes, shown in Figure 4. The approach utilized for this structure is to make our decisions considering how effective a shot would be against a selected unit, as well as how safe that shot would be to nearby friendly units. Effectiveness is determined by two main items; zerglings are low health units and the siege tank can easily waste some of its damage potential by targeting a very damaged zergling. However, if the very damaged potential target is in the middle of a group of hostiles, selecting that target may still be ideal due to the splash damage. Shot safety is essentially the opposite, now considering splash damage a shot would do to any friendlies, combined with the lowest health of the friendly units that would be affected by said splash damage. A differentiation between the marines' fire control is that the marines should always attack as often as they can in this engagement due to the fact they only damage their hostile target. The fire control for the Siege Tank will select the hostile target to fire at among all hostiles it considers, but only if that maximum fire bid is above 50%, otherwise it would opt to not fire.

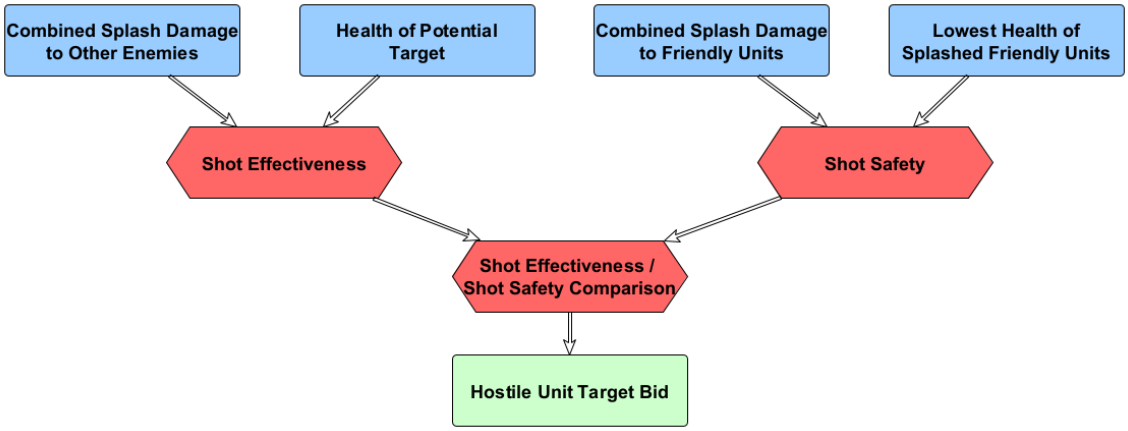

Figure 4. 3-FIS tree for Tank Firing Control utilized within the studied model.

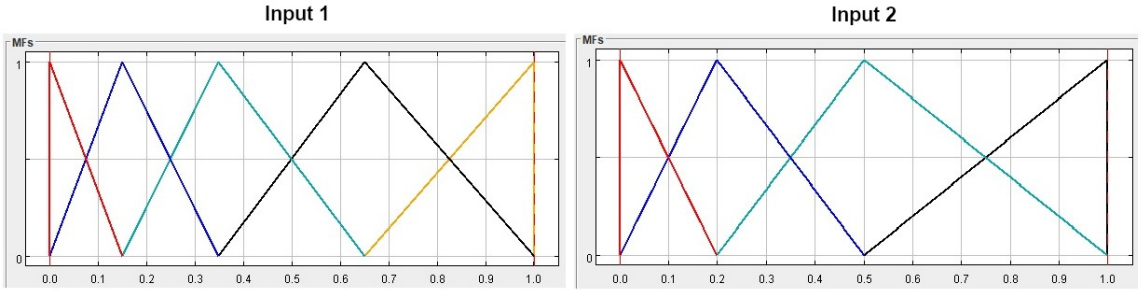

Figure 5. MFs for Marine Firing FIS. Input 1 corresponds to normalized potential target health with 5 MFs for "Very Low, Low, Moderate, High, Very High". Input 2 corresponds to current number of assigned friendly attackers already through this bidding cycle with 4 MFs for "None, Some, Many, All".

2.2.3. Explainability

After creating the tree structure, individual FISs are constructed using expert knowledge where available in most cases. Often this will be in the form of the number of MFs which will be utilized in each FIS; often leaving the specific distribution of said MFs across the input space to the machine learning process.

Explainability can be analyzed through a plethora of manners; the structure of the FISs created for this study were designed to optimize the general explainability and interpretability of the system alongside raw performance. As an example, the input MF sets for the Marine Firing FIS are shown in Figure 5.

A variety of approaches can be utilized to interpret the membership functions and provide explainability, but one of the simplest approaches would be to report or display the most active membership function for each input, corresponding with its rules. This represents the membership function with the largest impact on the output. This can essentially be compared to Shapley Values, a popular explainability metric utilized across multiple RL approaches[22,23]. In general approaches, these values enable a determination of the most impactful variables leading to a particular output. Through the membership functions of a given FIS, this is innately provided. Due to the fact that all system variables have the potential to be human understandable terms within a fuzzy based system such as the GFT, there is further intrinsic value within this approach if the GFT is properly designed. Note that explainability is not inherently granted through the utilization of fuzzy systems; rather fuzzy logic is a construct in which systems that are highly explainable can be developed.

For example, an input combination of 0.04 normalized target health, and 0.01 assigned attackers with its resultant output can be examined, and an explanation structure can be generated from membership function and rule labels: "Bid output is Very High because target health is Very Low and assigned attackers is None". For more extensive fuzzy tree structures, this explanation can be repeated across subsequent cascaded FISs allowing for the creation of a linguistic explanation of the entire decision process. This form of explainability and transparency will be heavily utilized during the formal verification process as manual corrections to the post-training model will be performed if any specifications are found to not be adhered to via formal methods. This requires direct changing of the code of the model at all levels, not just the input or output layers. Holistic understanding of any modifications made throughout this process are critical for any potential deployment of the system post-modification.

2.2.4. Reinforcement learning

The standard RL process for a GFT is to first create a portfolio of training scenarios that each individual in the GA population is evaluated over. This model was created through utilization of an open source Python package for interfacing with SC2 such that constructive runs through these scenarios is possible[24]. Within this study a single mission portfolio is utilized to highlight the formal verification processes, but for most applications a portfolio containing multiple holistic scenarios as well as specific training sub-problems would be included[11,14]

The manner in which the performance will be evaluated must also be defined through the requisite Fitness Function for the GA. The fitness function utilized within this study is found in Equation 1.

$$Fitness = (MarinesAlive * 25.0) + FriendlyHPRemaining - HostileHPRemaining - (Timesteps/100.0) \quad (1)$$

The magnitude range of this fitness function is not critical within EVE, but rather the ability for the evolutionary process to differentiate relative fitnesses between potential solutions, or chromosomes, in a manner that thoroughly rewards good behavior and punishes bad. With this example, the terms specifically are a flat 50 point reward for every marine alive at the end of the scenario. This is then added to the summation of the total friendly health remaining, including that of the siege tank, which has a notably higher health pool than marines. This is subtracted from the hostile force health pool remaining. Finally, there is a slight penalty for the number of timesteps it takes to complete the scenario, as if all other parameters have reached optimality, ideally the solution executes quickly in case additional threats would be inbound to the force. This function is able to be iterated over in future work, but serves as a good basis for the GA to evolve the population of chromosomes.

There is an additional complexity with this particular problem due to the nature of Starcraft 2 and this training setup; non-deterministic fitness evaluations. As the fitness value given to any chromosome within the population will drastically affect both its probability for breeding as well as the relative worth of potential future chromosomes, the ability for a good chromosome to be "unlucky" and a bad one to be "lucky" during their respective evaluations can be damaging to the effectiveness of an evolutionary system. There are mitigating methods, such as evaluating the scenarios, or portions of them, multiple times. Within this study, each chromosome will be evaluated a total of three times, with the worst fitness of those three being the actual fitness that is assigned, to easily mitigate the worst case risk at the expense of computational efficiency of each generation's evaluation.

2.2.5. Specification identification and development

One of the most difficult, and important, aspects of formal verification is specification identification and development. Most often, these specifications come directly from system requirements. However, they can also come from other sources such as certification criteria and standards, external regulations such as Rules of Engagement (RoE), and simulation and testing results. In this work, the specifications come from expert knowledge on desired system behavior with respect to performance and safety of actions taken by the AI. Specifically, that the AI will not take certain actions if unacceptable damage or losses will occur to friendly forces.

Different types of specifications are created based on the FISs that are affected, the needed expressiveness of formal languages in which they will be translated, and the tools available for verifying the systems. For this study, four safety specifications were developed. Safety, in this context, refers to behavior such that *nothing bad ever happens*, where "bad" is defined as an undesirable set of system states. Some would help guarantee not only safe, but also ideal behavior from a performance perspective. However, other safety specifications solely focus on desired safety qualities at the expense of raw fitness performance.

These specifications, in natural language, are as follows:

- **Medivac Healing Spec:** If a marine's health is very high and the marine is not under attack, its corresponding healing bid must be very low;
- **Marine Firing Spec:** If a separate friendly marine has already bid to attack a target whose health is very low, than a marine's fire bid on that target must be very low;
- **Tank Firing Spec:** If a friendly unit would take splash damage from a tank shot and the lowest health friendly in splash range is between very low and low health, only fire at the target if it would do very high damage to the enemy;
- **Tank Conservative Firing Spec:** Never cause splash damage to any friendly unit, regardless of their health.

Through setting the values to the corresponding terms utilized within these specifications to that of our MFs, we can quite simply apply these specifications to a trained Fuzzy Tree through the formal verification tools with the Psion fuzzy logic package. If a counterexample is found where the specification does not hold, typically the designer must either change the spec, or as we will limit this study to, modify the MFs and/or RBs of the associated FISs.

3. RESULTS

3.1. Reinforcement learning

EVE was instantiated to have a relatively small population, 60 chromosomes, each defining a set of MFs and RBs for all seven FISs. The training process was run for 50 generations, each chromosome being evaluated over three scenarios per generation. Thus, this system was trained over 9,000 Starcraft 2 engagements, which was sufficient in this case to reach high performance.

Presented in Figure 6 is a plot showing the best, worst, and mean chromosome fitness within the population of 60 at each generation. Additionally, the running best chromosome's fitness for each generation is displayed. Generally with the fitness function utilized in this system, if the chromosome successfully completed its mission, it would score at least quite close to a positive number. A score of 389.49 was found for the best chromosome thus far. The breakdown of this fitness value is shown in Table 1.

EVE has a heavy focus on maintaining diversity, and therefore especially with a generally smaller population, it is not surprising to see that during each generation the worst chromosome was not able to successfully complete this difficult mission. The distribution between best, worst, and mean is at least one sign of a healthily diverse population throughout the generations. This can help prevent stagnation and ensure continued improvements.

Table 1. Individual Components that made up best chromosome fitness of 389.49.

Fitness Component	Value
Marines Alive (x25)	100.0
Total Friendly Health Remaining	292.0
Total Hostile Health Remaining	0.0
Timestep Penalty (-Timestep/100.0)	-2.51
Total	389.49

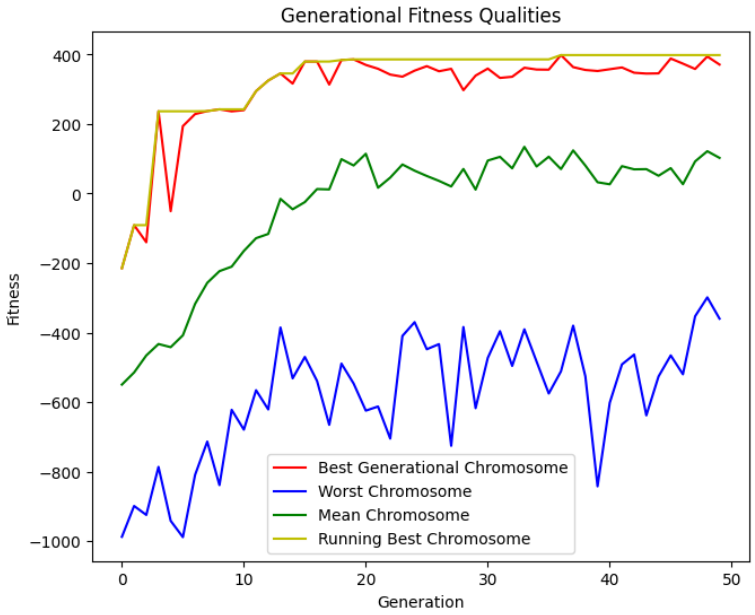

Figure 6. Generational and cumulative fitness values of Genetic Algorithm population.

Figure 7. Frame captures 1 (Left) and 2 (Right) of the mission depicting the evaluation of the best chromosome.

In Figure 7 there are 2 frames of the performance displayed. It is a very active mission, with over 70 actions per second executed by this particular AI model, equating to around 4,200 actions per minute for the roughly 5-9 seconds this mission will last. Obviously this is quite higher than even expert humans would be able to maintain, but again following humanistic restrictions is not a focus of this particular study. There is non-determinism, but the problem typically ends with a few of the marines having been defeated, in this case there were two defeated marines.

Additional training and and increasing the size of the training portfolio would likely lead to greater performance, but for the purposes of this formal verification study, the resultant chromosome is sufficient. It is high

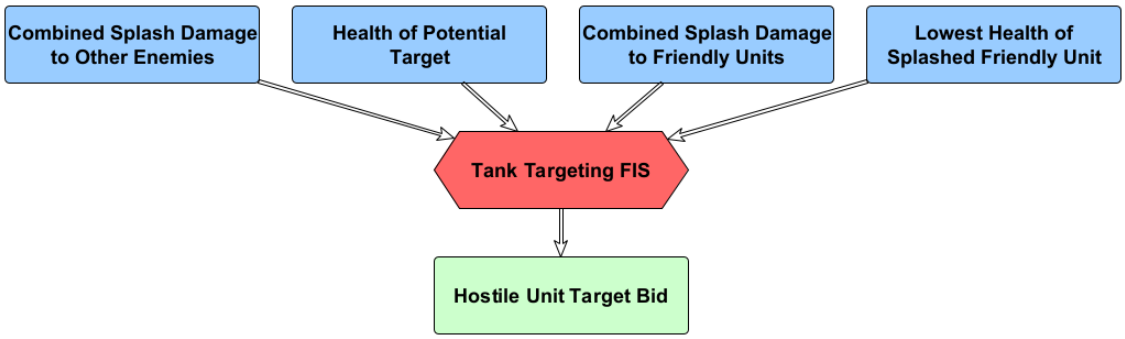

Figure 8. Single FIS variant for siege tank control.

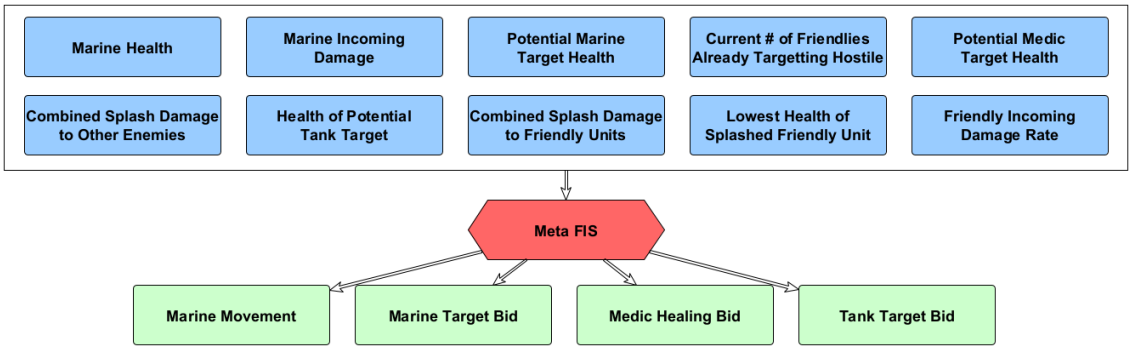

Figure 9. Single FIS variant for all control actions.

performance but will likely have some edge cases that violate the specifications.

3.1.1 Reinforcement learning comparison

Two additional fuzzy systems were developed for the same scenario as a learning performance comparison to the above system. The first comparative system utilized is quite similar to the study system, with the sole difference being that instead of utilizing three separate FISs for control of the siege tank's targeting, this portion of the AI is combined into a single 4-input FIS. The revised diagram is seen in Figure 8.

As five MFs are utilized per input, a full fuzzy rule-base of the original system for siege tank control utilized within this study has 75 rules, 25 rules for each of the three FISs seen in Figure 4. This modified variant has 5^4, or 625, total rules. This change in search space size is significant in terms of total chromosome size, but chromosomes of this size are anticipated to be well within the reasonable scope of the genetic algorithm utilized herein.

Note that the performance of the original system is bounded above by the variant in Figure 8, as any resultant control surface of the original system can be developed within this variant, as can others. The same is true compared to both of these systems for a second variant in which the entirety of the fuzzy AI is encompassed by a single 10-input, 4-output FIS. While the performance ceiling of the system shown in Figure 9 is the same, or higher, as the other variants, the anticipated performance through the same RL process is significantly worse due to an extremely large fuzzy rule-base.

While the original system utilizes a total of 150 fuzzy rules, the single-FIS variant would have $4 * 5^{10}$ or

39,062,500 rules. During the RL comparison process, the compute system utilized however had 32 GB of RAM, an insufficient amount to perform with a chromosome defining a rule-base of this magnitude. However, if this was reduced to 4 MFs per input, making the rule-base contain $4 * 4^{10}$, or 4,194,304 total rules, then 32 GB of RAM was sufficient.

The RL process for these two variants was exactly the same as before, with a total of 60 chromosomes trained over 50 generations. The maximum fitness found by generation for each of the systems is displayed in Figure 10. As anticipated, the 10-input 4-output variant had significantly worse performance than the original system, though improvements were able tobe made throughout the RL process. Though the performance ceiling of the original system is again bounded above by this variant's, the amount of RL that would be necessary to surpass the original's performance is likely prohibitive.

Alternatively, the performance of the variant that solely combined the siege tank's control into a single FIS performed favorably compared to the study's original system. As the genetic process is non-deterministic, and the total number of fuzzy rules is still relatively small, the fact that the initial generation's performance was superior than the original study's is well within expected range. While additional runs of the RL process would create different results, the increased granularity of this variant as compared to the study's original system can be explained through the increase in the search space size. For the majority of this small, 50-generation process, the original system has a higher maximum fitness, though the variant does ultimately end with a higher performing fitness by the end of the run.

While this is a very small GFT system, this comparison demonstrates trade-off comparisons between increased number of FISs (and thus, less overall rules) and the potential effect on RL performance. Though the single-FIS for siege tank control variant performed slightly better, it would be more difficult to formally verify, and overall has a more complex challenge for explainability as compared to the original system. For the remainder of the study, the original GFT architecture will be utilized.

3.2. Formal verification

3.2.1 Safety specification 1

Again, our first specification, the Medivac Healing Spec, states "If a marine's health is very high and the marine is not under attack, its corresponding healing bid must be very low". Although simple, adherence to this specification is desired in all cases. We can represent this in a numerical form by utilizing the points of our MFs with maximum value for each linguistic term, as shown in Equation 2. This is then translated to Linear Temporal Logic (LTL) as shown in Equation 3.

$$\begin{aligned} Spec1 = &\text{If } (MarineHealth > 0.75) \text{ and } (MarineDamageRate = 0.0) \\ &\text{then } (HealBid < 0.25) \end{aligned} \tag{2}$$

$$\begin{aligned} \varphi_1 = &\square((MarineHealth > 0.75) \wedge (MarineDamageRate = 0.0) \\ &\rightarrow (HealBid < 0.25)) \end{aligned} \tag{3}$$

Utilizing Psion and JKIND, we can evaluate our singular FIS node over this specification and either receive a mathematical guarantee that our system will adhere to this system in all cases, or receive a counterexample trace which proves that our system does not. Table 2 shows that a counterexample was found. Note that interestingly the presented counterexample corresponds to exactly the values 1.0 and 0.0 for our two inputs

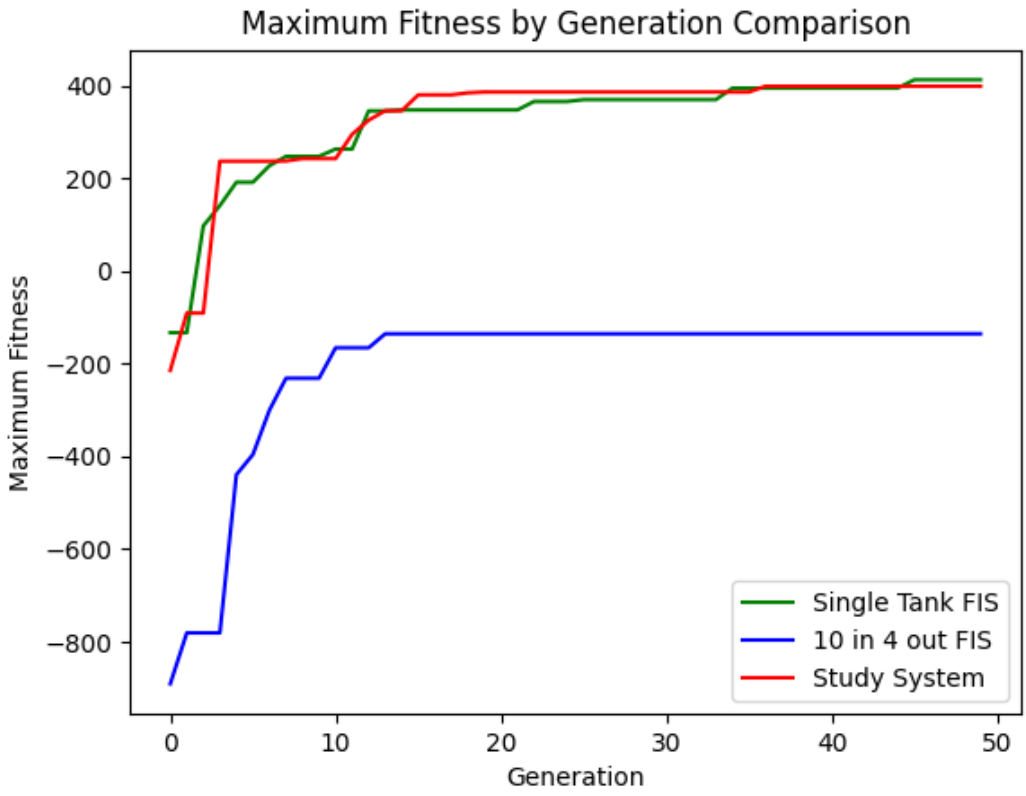

Figure 10. RL performance comparison of the variant with a single FIS for siege tank control, the variant with a single FIS providing all control actions, and the original system that is utilized within this study.

Table 2. Counterexample for Spec 1 failure prior to modification

Variable	Value
MarineHealth	1.0
MarineDamageRate	0.0
HealBid	0.3

respectively. A singular rule in our RB will correspond to exactly when the inputs are at those values, and those values are the extremes of the normalized space for both inputs. Hence, upon investigation of our RB we would see that we have a rule in our chromosome of "If Marine Health is Very High and Marine Damage Rate is None, then Healing Bid is Low". By changing the output MF to "Very Low" for this rule, we can easily solve this specification failure.

Though not a requirement, it is also often very beneficial to develop a scenario within the simulation environment that can help represent a potential case of a found counterexample. Observing the agent's performance through these specifically designed scenarios can both provide insight to the control issue, as well as provide feedback to the solution of the problem once found. Note that removing the failure case from a specific scenario does not guarantee that the specification will always hold, but measures can be taken to ensure this within regions of interest and verified again using Formal Methods. In this case, it is not necessary due to the simplicity of the counterexample found, but was completed and is seen below in Figures 11 and 12.

A scenario was developed in which there are two marines, a medivac, and two zerglings. The zerglings are at full health, but the marines are wounded. In particular, the marine at the top of the formation is moderately

Figure 11. The three frames of the φ_1-non-adherent medivac healing spec scenario are (Left) both marines with the top marine alive and the bottom being healed, (Center) the top marine defeated and the bottom marine still being healed, and (Right) the scenario complete with the bottom marine surviving and all zerglings defeated.

Figure 12. The three frames of the φ_1-adherent medivac healing spec scenario are (Left) both marines alive and the wounded top marine being healed, (Center) the top marine under attack and surviving with medivac support, and (Right) the scenario complete with both marines alive and all zerglings defeated.

hurt, and the marine at the bottom only slightly so. In the case of Figure 11 the unmodified chromosome was used and for a slight period of time, before the zerglings reach the friendly forces, it heals the bottom marine first. This leads to the top marine being defeated, reducing the damage output of the friendly squad by half. The bottom marine does manage to survive, but just barely.

If instead the bottom marine is ignored, at least at first, then the medivac heals the top marine, managing to keep both alive and secure a higher scoring victory. This is shown in Figure 12, though again simply because this specific scenario shows adherence to the specification, formal verification is needed to confirm that it always holds.

3.2.2. Safety specification 2

Safety specification 2 states "If a separate friendly marine has already bid to attack a target whose health is very low, than a marine's fire bid on that target must be very low." This is represented in the same manner as the first specification in Equation 4 and in LTL in Equation 5, utilizing the MF distribution shown above in Section 2.3.

$$\begin{aligned} Spec2 = & If(TargetHealth < 0.15) and (MarinesAssigned > 0.0) \\ & then(FireBid < 0.25) \end{aligned} \tag{4}$$

Figure 13. The three frames from the φ_2-adherent marine firing control scenario are (Left) two marines with six wounded zerglings approaching, (Center) halfway through scenario with three remaining zerglings, and (Right) the scenario complete with both marines alive due to intelligent targeting.

$$\begin{aligned}\varphi_2 =&\square((TargetHealth < 0.15) \wedge (MarinesAssigned > 0.0) \\ &\rightarrow (FireBid < 0.25))\end{aligned} \tag{5}$$

Despite not being explicitly directed to, the resultant chromosome received from training was proven through JKIND to already adhere to this specification, with the resultant output confirming correctness across all input values. However, a relevant scenario was still created and is shown in Figure 13. Within this mission there are only two marines on the friendly forces and six zerglings. However these marines are at full health and the zerglings are each wounded to the point where two shots from the marines would defeat them. Thus, intelligent target assignment is required to win, but victory is possible.

While the training process did generate a model that was adherent to this specification, the confirmation of specification adherence across all possible scenarios is still worthwhile.

3.2.3. Safety specifications 3 and 4

The last two specifications investigated within this study are related, both dealing with the fire control of the siege tank. Specification 3 again being "If a friendly unit would take splash damage from a tank shot and the lowest health friendly in splash range is between very low and low health, only fire at the target if it would do very high damage to the enemy" and able to represented as in Equation 6 and in LTL in Equation 7.

$$\begin{aligned}Spec3 =&If(FriendlySplash > 0.0)and(0.40 > LowestFriendly > 0.15)and(ShotEff. < 0.75) \\ &then(Bid < 0.50)\end{aligned} \tag{6}$$

$$\begin{aligned}\varphi_3 =&\square((FriendlySplash > 0.0) \wedge (LowestFriendly > 0.15) \wedge (LowestFriendly < 0.40) \\ &\wedge (ShotEff < 0.75) \rightarrow (Bid < 0.50))\end{aligned} \tag{7}$$

This is due to the fact that the siege tank will only fire at a target if the fire bid is above 50%, so if the shot effectiveness is below "very high" then we do not wish to fire. This specification did fail with the post-training chromosome, and produced a counterexample as can be seen in Table 3. The counterexample displayed here demonstrates that our AI model was perhaps close to adhering to the specification; the shot priority value was not far above the maximum threshold of 0.50. For this specification there are three FISs to consider, but given the context of the specification a general reduction in the output MFs of the Shot Safety FIS was selected to modify this FIS until it was adherent. However, by changing the MFs and RBs in any of the three FISs

Table 3. Counterexample for Spec 3 failure prior to modification

Variable	Value
CombinedEnemySplash	0.75
CombinedFriendlySplash	0.35
EnemyHealth	0.583
SplashedFriendlyLowestHealth	0.25
ShotEffectiveness	0.5
ShotPriority	0.55
ShotSafety	0.5

there are likely solutions that would be similarly adherent. This specification may be joined by others in the future though, and attempting to modify this FIS tree while maintaining reasonable semantic logic is ideal; thus modifying the safety evaluation FIS was selected.

A scenario was developed to demonstrate this issue which contains one siege tank, two marines, and six zerglings. Readers familiar with Starcraft 2 may be aware that siege tanks within the game do not natively have the ability to hold their fire. Modifications to, or deeper usage of the API can allow a unit to be "paused". In the example scenario created for the tank specifications however, a simple off-screen stationary structure served as a possible target for the tank to attack, rather than the zergling if it chose to not fire at the hostile troops.

Figure 14 shows the post-training FIS in this new scenario. Four specific frames are present in this image, with the upper row being frames 1 and 2, and the bottom being 3 and 4. In the first frame, the tank does take an effective shot at the zerglings before they enter splash range with the top marine. The tank is not able to take another shot again until Frame 2, which is not against the spec as the top marine has very low health at this time and is surrounded by three zerglings. That shot defeats two zerglings, as well as the top marine, but adhered to the specification. The remaining zergling then approaches a full health bottom marine in Frame 3. Unfortunately, in Frame 4, the tank is ready to fire again, and kills a now wounded bottom marine just before he could defeat the zergling and still be alive. However, the tank did survive so the friendly forces secured a victory, just not an ideal or adherent one.

In Figure 15 the engagement plays out almost entirely the same in frames 1 through 3. However, come frame 4, the tank is opting to not attack, allowing the bottom marine to secure the final kill, completing the mission with only 1 marine loss.

Specification 4 is essentially a much more conservative option than specification 3 and states "Never cause splash damage to any friendly unit, regardless of their health". This is represented in natural language in Equation 8 and in LTL in Equation 9.

$$\begin{aligned} Spec4 = & If(FriendlySplashDamage > 0.0) \\ & then(FireBid < 0.50) \end{aligned} \tag{8}$$

$$\begin{aligned} \varphi_4 = & (FriendlySplashDamage > 0.0) \\ & \rightarrow (FireBid < 0.50) \end{aligned} \tag{9}$$

The failure case presented to this system from our trained chromosome is the exact same from JKIND, which is as we expect given the fact that this specification is more conservative. Many solutions exist to create a set of FISs that adhere to this specification, including modifying both the Shot Safety FIS to have much lower

Figure 14. The four frames from the φ_3-non-adherent siege tank firing control scenario are (Upper Left) scenario start showing siege tank taking a safe shot, (Upper Right) siege tank fires at zerglings within range of healthy marine, (Lower Left) marine death due to friendly siege tank fire, and (Lower Right) siege tank firing and defeating all zerglings and remaining friendly marine.

Figure 15. The four frames from the φ_3-adherent siege tank firing control scenario are (Upper Left) scenario start showing siege tank taking a safe shot, (Upper Right) siege tank fires at zerglings within range of near-death marine, (Lower Left) low-health marine death due to friendly siege tank fire, and (Lower Right) siege tank holding fire and allowing marine to defeat final zergling.

Figure 16. The four frames from the mission failure, φ_4-adherent siege tank firing control scenario are (Upper Left) scenario start showing siege tank taking a safe shot, (Upper Right) siege tank does not fire on zergling group in proximity to top marine, (Lower Left) top marine is defeated by zergling group and siege tank continues holding fire, and (Lower Right) mission failure because all marines defeated and siege tank cannot target nearby units.

Output MFs referenced in the RB, as well as in the Shot Effectiveness/Safety Comparison FIS. A version of the modified training chromosome was manually tuned to the point where adherence to this specification was proven by JKIND. Figure 16 below shows the performance of this new system, which essentially opts out of taking a meaningful shot at Frame 2 when the hostile army is heavily grouped around the top marine. While adherent to the spec, this mission ends in failure.

4. DISCUSSION

As can be seen in the Results section, the performance of the AI system after the reinforcement learning process was such that it was likely superhuman[25]. Note that this is heavily dependent on the hypothetical human player. As the actions per minute of the AI system was not constrained, it could select and execute much faster than any human likely could. Note that this is also somewhat different from other SC2 AI systems like AlphaStar, as those are constrained to have near-human constraints on information and action execution rates. The purpose of the AI in this work though is to perform a subset of actions in particular scenarios and is not meant to be a general SC2 player. Instead, at least for specifications 1 through 3, the focus was on creating a high performance AI for unit controls in difficult engagements that were also explainable and formally proven to adhere to safety specifications.

With respect to the safety specifications, it was shown in both simulation and through verification with the model checker JKIND that counterexamples were found for most of the specifications. That is, there were conditions where the system could output actions that would violate the specifications. The counterexamples, due to the transparent and explainable nature of GFTs, were then used to assist in identifying parameters that needed correction. This was achieved by expert knowledge, specifically familiarity with Starcraft 2, but could also be aided via further reinforcement learning runs to correct undesired behaviors. After correction, the

system was verified against the specifications which were shown to always hold. Although simulation results also show that the system performs as intended in the particular runs executed, the benefit of formal verification is that it will hold over any potential run with the given AI system. This is the differentiating factor for formal verification compared to more common methods that rely on numerical evaluation. Formal verification, in this case model checking and SMT solving, can give definitive evidence that the system is correct, while numerical evaluation can only return found counterexamples, but not conclusively identify that there are none.

The case of specification 4 presents a unique point; adherence to certain safety specifications may not necessarily improve overall system performance. For example, there are often strict standards for use-cases that require certification which may overall slow down or weaken control systems, but are still necessary in order to deploy and trust the system. Consider laws such as speed limits placed onto a theoretical optimal driving controller; if the fitness function is minimizing travel time and fuel consumption, an unconstrained RL agent would likely optimize to illegal behaviors in some cases. However, for AI systems in mission/safety-critical applications the benefit of formal verification cannot be understated. In this example of specification 4, all friendly fire was strictly disallowed, even if it would lead to the death of the entire force.

Regarding explainability, the structure of the GFT created is such that actions are easily explained and interpretable by humans. This is of particular interest when auditing the system for explanations on behavior that was learned throughout the reinforcement learning process. In this case, it was also used for a human designer to correct errors in the AI system. This is a powerful capability when creating complex AI control systems for safety-critical applications. Although SC2 AI play will likely never be considered ”safety-critical”, it serves as a good proxy problem for other decision-making applications in notionally similar environments.

4.1. Future work and extensions

Potentially the most obvious extension of this work is to make a more general AI for SC2 that plays more portions of the game including things such as: base building, resource management, etc. This would demonstrate the applicability and efficacy of GFT towards a well-known benchmark problem in RL. That could then be used to show how explainability in complex AI systems may be desired, especially as a learning tool for humans.

In the future, these scenarios could also be used for comparisons against other RL approaches. Due to the lack of explainability and formal verifiability of common RL techniques compared to GFTs, the resulting comparison would be purely performance based.

Another important extension of this work would be to extend the formal verification methodology to include portions of the Starcraft 2 dynamics. Doing so would allow for reasoning about higher level behaviors of the system. In this work, only properties about the GFT itself are verified, while inclusion of dynamic models for portions of Starcraft 2 would allow for interesting temporal specifications to be evaluated. E.g. if dynamics are included for unit damage, damage inflicted by attacks, cool downs, unit movements, etc., specifications could be created to reason about, say, whether it's possible for any friendly units to be lost, or finding guaranteed minimums. The value of doing this is exceptional as it can provide definitive evidence of baseline performance, but of course is much more difficult than verification of the AI system without dynamics.

5. CONCLUSION

In conclusion, a GFT model was developed and trained for a particular scenario and then verified against four behavioral specifications. Post-training, the model did not adhere to three of these specifications, and counter-examples were found from the formal methods tools utilized. For these cases, the GFT was evaluated over scenarios within the Starcraft 2 environment which demonstrated the specific failure modes detailed in the counterexamples. Modifications to the system were then made for each specification until the system was

proven to be adherent to these safety specifications. The resulting GFT is then guaranteed to be adherent to specifications over all input values while being explainable and performant. While this study does not intend to demonstrate performance of an entire Starcraft 2 game controller, it demonstrates the capability of a Fuzzy Logic-based AI system to be trained and proven to adhere to safety specifications in a specific subset of the control actions within this game that represent mission/safety-critical elements.

DECLARATIONS

Authors' contributions

Made contributions to conception and design of the work, developed most associated code for Starcraft integration and reinforcement learning, performed data analysis and figures of interest, manuscript writing and related tasks: Ernest N

Contributed to parts of the conception and design, implemented the formal verification techniques towards Fuzzy Systems, performed analysis and translation of formal specifications, manuscript writing and related tasks: Arnett T

Created the interfaces needed to easily integrate the Thales's toolkit with Python environments such as the SC2 interfaces used in this work, manuscript writing and related tasks: Phillips Z

Availability of data and materials

While the resultant GFT AI model and the Psion and EVE software cannot be shared openly, the Starcraft 2 map files utilized in the scenarios shown in this study could be. They are not currently hosted, but can be made available upon request.

Financial support and sponsorship

None.

Conflicts of interest

All authors are employees of Thales Avionics Inc., from which two software packages that are commercially available were utilized in this research.

Ethical approval and consent to participate

Not applicable.

Consent for publication

Not applicable.

REFERENCES

1. Zhao Y, Wang H, Xu N, Zong G, Zhao X. Reinforcement learning-based decentralized fault tolerant control for constrained interconnected nonlinear systems. *Chaos, Solitons & Fractals* 2023;167:113034. DOI
2. Tang F, Niu B, Zong G, Zhao X, Xu N. Periodic event-triggered adaptive tracking control design for nonlinear discrete-time systems via reinforcement learning. *Neural Netw* 2022;154:43-55. DOI
3. Silver D, Huang A, Maddison CJ, et al. Mastering the game of Go with deep neural networks and tree search. *Nature* 2016;529:484-9. DOI
4. Gunning D, Aha D. DARPA's explainable artificial intelligence (XAI) program. *AIMag* 2019;40:44-58. DOI
5. Ross TJ. Fuzzy logic with engineering applications. John Wiley & Sons; 2009. DOI
6. Castro JL. Fuzzy logic controllers are universal approximators. *IEEE Trans Syst, Man, Cybern* 1995;25:629–35. DOI
7. Buckley J, Siler W, Tucker D. A fuzzy expert system. *Fuzzy Sets and Systems* 1986;20:1–16. DOI

8. Coleman CP, Godbole D. A comparison of robustness: fuzzy logic, PID, and sliding mode control. In: Proceedings of 1994 IEEE 3rd International Fuzzy Systems Conference. IEEE; 1994. pp. 1654–59. DOI
9. Moral A, Castiello C, Magdalena L, Mencar C. Explainable Fuzzy Systems. Springer; 2021. DOI
10. Arnett TJ. Verification of genetic fuzzy systems [MS Thesis]. University of Cincinnati; 2016. DOI
11. Ernest ND. Genetic fuzzy trees for intelligent control of unmanned combat aerial vehicles. University of Cincinnati; 2015. DOI
12. Herrera F. Genetic fuzzy systems: taxonomy, current research trends and prospects. *Evol Intel* 2008;1:27-46. DOI
13. Fleck DE, Ernest N, Adler CM, et al. Prediction of lithium response in first-episode mania using the LITHium Intelligent Agent (LITHIA): pilot data and proof-of-concept. *Bipolar Disord* 2017;19:259-72. DOI
14. Ernest N, Carroll D, Schumacher C, et al. Genetic fuzzy based artificial intelligence for unmanned combat aerial vehicle control in simulated air combat missions. *J Def Manag* 2016;;6:2167-0374. DOI
15. Thales. Thales GFT AI Toolkit. Thales; 2022. Available from: https://www.thalesgroup.com/en/markets/aerospace/big-data-aerospace/genetic-fuzzy-tree-ai-toolkit-critical-decisions. [Last accessed on 20 Mar 2023]
16. Marques-Silva J. Practical applications of boolean satisfiability. In: 2008 9th International Workshop on Discrete Event Systems. IEEE; 2008. pp. 74–80. DOI
17. Hinchey MG, Bowen JP. Applications of formal methods. vol. 1. Prentice Hall New York; 1995. DOI
18. Ernest N, Kunkel B, Arnett T. An investigation into the impact of system transparency on work flows of fuzzy tree based AIs. In: North American Fuzzy Information Processing Society Annual Conference. Springer; 2020. pp. 349–59. DOI
19. Moura Ld, Bjørner N. Z3: An efficient SMT solver. In: International conference on Tools and Algorithms for the Construction and Analysis of Systems. Springer; 2008. pp. 337–40. DOI
20. Gacek A, Backes J, Whalen M, Wagner L, Ghassabani E. The JKind model checker. In: International Conference on Computer Aided Verification. Springer; 2018. pp. 20–27. [DOI
21. Mamdani EH, Assilian S. An experiment in linguistic synthesis with a fuzzy logic controller. *Int J Man-Mach Studies* 1975;7:1–13. DOI
22. Scapin D, Cisotto G, Gindullina E, Badia L. Shapley Value as an Aid to Biomedical Machine Learning: a Heart Disease Dataset Analysis. 2022 22nd IEEE International Symposium on Cluster, Cloud and Internet Computing (CCGrid) 2022:933–39. DOI
23. Heuillet A, Couthouis F, Díaz-Rodríguez N. Collective EXplainable AI: Explaining Cooperative Strategies and Agent Contribution in Multiagent Reinforcement Learning With Shapley Values. *IEEE Comput Intell Mag* 2022;17:59–71. DOI
24. Burnysc2. Burnysc2 python-SC2 Python Package. Github; 2022. Available from: https://github.com/BurnySc2/python-sc2. [Last accessed on 20 Mar 2023]
25. Wikipedia. Progress in artificial intelligence. Wikimedia Foundation; 2022. Available from: https://en.wikipedia.org/wiki/Progress_in_artificial_intelligence#Current_performance. [Last accessed on 20 Mar 2023]

Cui *et al*. *Complex Eng Syst* 2023;3:3
DOI: 10.20517/ces.2022.57

Complex Engineering Systems

Research Article

Open Access

Parameters optimization of electro-hydraulic power steering system based on multi-objective collaborative method

Taowen Cui[1,2], Shuaiyin Wang[1], Yuan Qu[2], Xiang Chen[2]

[1]Intelligent Vector Technology Control Lab, Chery Automobile Company Limited, Wuhu 241000, Anhui, China.
[2]School of Automotive and Transportation Engineering, Hefei University of Technology, Hefei 230041, Anhui, China.

Correspondence to: Dr. Taowen Cui, School of Automotive and Transportation Engineering, Hefei University of Technology, Hefei 230041, Anhui, China. E-mail:nuaa_ctw@126.com

How to cite this article: Cui T, Wange S, Qu Y, Chen X. Parameters optimization of electro-hydraulic power steering system based on multi-objective collaborative method. *Complex Eng Syst* 2023;3:3. http://dx.doi.org/10.20517/ces.2022.57

Received: 20 Dec 2022 **First Decision:** 19 Jan 2023 **Revised:** 3 Feb 2023 **Accepted:** 17 Feb 2023 **Published:** 9 Mar 2023

Academic Editors: Hamid Reza Karimi, Serdar Coskun **Copy Editor:** Fangling Lan **Production Editor:** Fangling Lan

Abstract

Electro-hydraulic power steering (EHPS) systems are widely used in commercial vehicles due to their adjustable power assist and energy-saving advantages. In this paper, a dynamic model of the EHPS system is developed, and quantitative expressions for three evaluation indexes, steering road feel, steering sensibility and steering energy loss, are derived for the first time. A multi-objective collaborative optimization model of the EHPS system is then established, which consists of one total system and three parallel subsystems, based on collaborative optimization theory. Considering the coupled variables of each subsystem, the total system is optimized by a multi-objective algorithm, while the subsystems are optimized by a single-objective algorithm. The optimization results demonstrate that the average frequency domain energy of the steering road feel is increased by 69.1%, the average frequency domain energy of steering sensitivity is reduced by 19.2%, and steering energy consumption is reduced by 10.8% compared to the initial value. The non-dominated sorting genetic algorithm-II (NSGA-II) shows superior comprehensive performance compared to the other two multi-objective algorithms, and the optimization performance can be further improved by setting appropriate algorithm parameters.

Keywords: Electro-hydraulic power steering, multi-objective optimization, collaborative optimization, non-dominated sorting genetic algorithm-II

1. INTRODUCTION

As the focus on driving experience increases, research into vehicle steering systems has also gained attention. Traditional hydraulic power steering (HPS) systems provide assistance torque through an engine and offer a clear road feel, but have the disadvantage of high energy consumption. Electric power steering (EPS) systems provide adjustable assistance torque through a motor and have lower energy consumption, but the power-assisted range of EPS systems is narrow, limiting their application in vehicles with heavy front axle loads. Electric-hydraulic power steering (EHPS) systems combine the advantages of both systems, providing better road feel and lower energy consumption. Thus, EHPS systems have been widely used in commercial vehicles.

In recent years, research into EHPS systems has mainly focused on the control aspect[1–6]. Neural network control algorithms have been applied to the steering assist control of EHPS systems to improve the driver's experience[7]. Kim *et al.* proposed a design method for the steering motor speed of EHPS systems based on driver perception, which improved the driver's steering road feel and eliminated the catch-up effect[8]. Lin *et al.* proposed a slip frequency control method for the steering motor of EHPS systems to effectively improve the response speed and accuracy of the steering motor[9]. Ye *et al.* simplified the EHPS system and introduced the H2/H∞ control method to control the power assistance, which improves the anti-interference performance of the steering system[10]. Hur *et al.* analyzed the characteristics of the interior permanent-magnet synchronous motor of EHPS systems and proposed precise control and real-time response control methods for the motor[11].

However, current research rarely focuses on the steering experience of EHPS systems, and the optimization of the overall EHPS system is rarely reported. The evaluation indexes of EHPS systems involve not only steering flexibility and road feel, but also steering economy and other aspects with coupled effects[12–14]. Therefore, the optimization of the EHPS system is essentially a multi-objective optimization problem (MOP).

Traditional multi-objective optimization algorithms usually set different weights for different indicators and sum them, thus transforming multi-objective optimization into single-objective optimization[15]. However, these optimization algorithms show poorer performance in solving too many optimization objectives and non-convex optimization problems, and are prone to falling into local optima[16]. As such, a number of intelligent optimization algorithms, such as non-dominated sorting genetic algorithm (NSGA) and NSGA-II, have been proposed and applied to satellite design and other fields[17,18]. Additionally, the collaborative optimization (CO) method can effectively solve complex optimization problems, with the obvious advantages of simplifying system decoupling and achieving parallel computation[19–21]. The complex optimization model is divided into several subsystems according to the optimization objectives, and the coupling variables in the subsystems are coordinated by the consistency constraint[22]. This is convenient for concurrent design, which is consistent with the modern industrial design structure[23–25].

In this paper, steering road feel, steering sensitivity, and steering energy loss are taken as evaluation indexes. Considering the coupling factors of each subsystem, the multi-objective collaborative optimization method of the EHPS system is explored.

The rest of the paper is organized as follows. The dynamic model of the EHPS system is established in Section 2, and the three evaluation indexes of the steering system are derived for the first time. Section 3 establishes the multi-objective collaborative optimization model of the EHPS system and shows the multi-objective optimization results. Conclusions are given in Section 4.

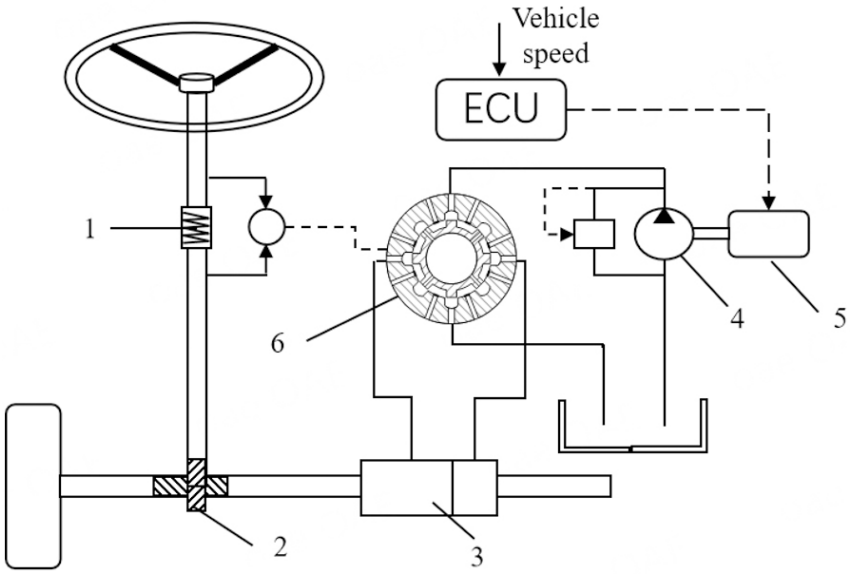

Figure 1. Structure of EHPS system. 1-Torque sensor; 2-rack and pinion;3-hydraulic cylinder; 4- hydraulic pump; 5-drive motor; 6-rotary valve.

2. SYSTEM DYNAMIC MODEL

The EHPS system consists of two parts: mechanical and hydraulic. The mechanical part includes a sequential connection of the steering wheel, steering column, rack and pinion, *etc*. The hydraulic part includes the oil tank, hydraulic pump, drive motor, rotary valve, and hydraulic cylinder. According to the vehicle speed and steering wheel torque, the drive motor drives the hydraulic pump at a certain speed to supply oil to the rotary valve and form a pressure difference on both sides. This pressure difference then provides adjustable assistance for the steering system through the hydraulic cylinder.

The EHPS system structure is shown in Figure 1.

2.1. Steering model

The dynamics model of the EHPS system can be expressed as follows, which includes the steering wheel model, drive motor model, rack and pinion model, and steering resistance torque model [2,8].

$$\begin{cases} J_{sw}\ddot{\theta}_{sw} + B_{sw}\dot{\theta}_{sw} = T_{sw} - T_s \\ J_m\frac{d\omega}{dt} + B_d\omega = T_m - T_c \\ m_o\ddot{x}_o + B_o\dot{x}_o = F_{ss} + F_h - F_r \\ T_r = \frac{2dk_1}{n_1}\left(\frac{a\omega_r}{u} + E_1\phi + \beta - \delta\right) \end{cases} \tag{1}$$

where

$$\begin{cases} F_h = A_p\left(\frac{\rho}{8\left(C_qA_2\right)^2}\left(Q_s - A_p\frac{dx_r}{dt}\right)^2 - \frac{\rho}{8\left(C_qA_1\right)^2}\left(Q_s + A_p\frac{dx_r}{dt}\right)^2\right) \\ q = 2p_b\left[\pi\left(R_2^2 - R_1^2\right) - \left(R_2 - R_1\right)Zt\right] \\ p_S = \frac{\rho}{8\left(C_qA_1\right)^2}\left(Q_s + A_p\frac{dx_r}{dt}\right)^2 + \frac{\rho}{8\left(C_qA_2\right)^2}\left(Q_s - A_p\frac{dx_r}{dt}\right)^2 \\ T_c = \frac{qP_s}{2\pi k_p} \end{cases}$$

2.2. Steering performance indexes

Considering the performance requirements of the EHPS system, steering road feel, steering sensibility, and steering energy loss are taken as the evaluation indexes. The quantitative formulas of the three evaluation indexes are derived as follows.

2.2.1 Steering road feel

In this paper, steering road feel is defined as a transfer function from steering resistance torque T_r to steering wheel torque T_{sw}, which reflects the efficiency of transmitting torque fluctuations from the road surface to the driver. Besides, the steering wheel angle θ_{sw} is defined as 0 to reduce a degree of freedom and facilitate the analysis of the steering system.

It is assumed that the torque sensor can be simplified as a torsion bar spring, and the measured value of the torque sensor could be computed by

$$T_s = K_s\left(\theta_{sw} - \theta_p\right) = -K_s\theta_p \tag{2}$$

where T_{sw} is torque obtained by torque sensor.

According to the current control strategy, the current can be given by

$$I = KT_s \tag{3}$$

The torque T_m provided by the motor can be given by

$$T_m = -K_aKK_s\theta_p \tag{4}$$

Where K_a is the torque coefficient of the motor, K is power gain coefficient.

According to (1)-(4), steering road feel can be computed as follows.

$$E(s) = \frac{T_{sw}(s)}{T_r(s)} = \frac{K_sq}{X_1s^2 + Y_1s + Z_1} \tag{5}$$

where

$$\begin{cases} X_1 = \mathrm{m}_r r_p^2 q + n_2 J_m A_p r_p \\ Y_1 = B_r q r_p^2 + n_2 B_m A_p r_p + \frac{\rho q^2 n \eta_v A_p^2 r_p^2}{2C_q^2 A_1^2} \\ Z_1 = A_p r_p K K_a K_s + q K_{TT} \end{cases}$$

Generally, the effective road information frequency domain range is 0-40 Hz. Thus, steering road feel is measured by its average frequency power within this range.

$$S_c = \frac{1}{2\pi\omega_0}\int_0^{\omega_0} |E(j\omega)|^2 d\omega \tag{6}$$

2.2.2 Steering sensibility

Steering sensitivity reflects the response speed of a vehicle to steering action and has an important impact on vehicle safety at high speed.

The vehicle three degree of freedom differential equation can be described as[17]

$$\begin{cases} I_z\dot{\omega}_r - I_x\ddot{\phi} = N_r\omega_r + N_\beta\beta + N_\phi\phi + N_\delta\delta \\ mu\left(\omega_r + \dot{\beta}\right) - m_sh\ddot{\phi} = Y_r\omega_r + Y_\beta\beta + Y_\phi\phi + Y_\delta\delta \\ I_x\ddot{\phi} - m_su\left(\omega_r + \dot{\beta}\right)h - I_x\dot{\omega}_r = L_p\dot{\phi} + L_\phi\phi \end{cases} \tag{7}$$

where

$$
\begin{aligned}
&N_r = -2\frac{a^2k_1+b^2k_2}{u} && N_\beta = -2ak_1 + 2bk_2\\
&N_\phi = -2aE_1k_1 + 2bE_2k_2 && N_\delta = 2ak_1\\
&Y_r = -2\frac{k_1a-k_2b}{u} && Y_\beta = -2\left(k_1+k_2\right)\\
&Y_\phi = -2k_1E_1 - 2k_2E_2 && Y_\delta = 2k_1\\
&L_\phi = -[2k_1E_1h + 2k_2E_2h + 2(C_{21}+C_{23}+\frac{C_{a1}+C_{a2}}{d^2})d^2 - m_sgh]\\
&L_p = -2\left(D_{21}+D_{23}\right)d^2
\end{aligned}
$$

The following formula can be obtained by Laplace transformation of the above formula

$$
\begin{cases}
\frac{\omega_r(s)}{\delta(s)} = \frac{A_3s^3+A_2s^2+A_1s+A_0}{B_4s^4+B_3s^3+B_2s^2+B_1s+B_0}\\
\frac{\beta(s)}{\delta(s)} = \frac{F_3s^3+F_2s^2+F_1s+F_0}{B_4s^4+B_3s^3+B_2s^2+B_1s+B_0}\\
\frac{\phi(s)}{\delta(s)} = \frac{H_2s^2+H_1s+H_0}{B_4s^4+B_3s^3+B_2s^2+B_1s+B_0}
\end{cases}
\tag{8}
$$

where

$$
\begin{aligned}
A_3 &= -muI_xN_\delta + h^2um_s^2N_\delta - huI_{xz}m_sY_\delta\\
A_2 &= muL_pN_\delta + I_xN_\delta Y_\beta - I_xN_\beta Y_\delta\\
A_1 &= muL_\phi N_\delta - L_pN_\delta Y_\beta + L_pN_\beta Y_\delta - \text{ hum }_sN_\phi Y_\delta + h_sN_\delta Y_\phi\\
A_0 &= -L_\phi N_\delta Y_\beta + L_\phi N_\beta Y_\delta\\
B_4 &= muI_{xz}^2 - muI_xI_z + h^2uI_zm_s^2\\
B_3 &= muI_zL_p + muI_xN_r - h^2um_s^2N_r + hI_{xz}m_sN_\beta + huI_{xz}m_sY_r - I_{xz}^2Y_\beta + I_xI_zY_\beta\\
B_2 &= muI_zL_\phi - muL_pN_r - muI_xN_\beta + h^2um_s^2N_\beta + muI_{xz}N_\phi + I_xN_\beta Y_r - I_zL_pY_\beta\\
&\quad -huI_{xz}m_sY_\beta - I_xN_rY_\beta + huI_zm_sY_\phi\\
B_1 &= -muL_\phi N_r + muL_pN_\beta - L_pN_\beta Y_r + h^{hum_s}N_\phi Y_r - I_zL_\phi Y_\beta + L_pN_rY_\beta - I_{xz}N_\phi Y_\beta\\
&\quad - \text{ hum }_sN_rY_\phi + I_{xz}N_\beta Y_\phi\\
B_0 &= muL_\phi N_\beta - L_\phi N_\beta Y_r + L_\phi N_rY_\beta - \text{ hum }_sN_\phi Y_\beta + \text{ hum }_sN_\beta Y_\phi\\
F_3 &= -hI_{xz}m_sN_\delta + I_{xz}^2Y_\delta - I_xI_zY_\delta\\
F_2 &= muI_xN_\delta - h^2um_s^2N_\delta - I_xN_\delta Y_r + I_zL_pY_\delta + huI_{xz}m_sY_\delta + I_xN_rY_\delta\\
F_1 &= -muL_pN_\delta + L_pN_\delta Y_r + I_zL_\phi Y_\delta - L_pN_rY_\delta + I_{xz}N_\phi Y_\delta - I_{xz}N_\delta Y_\phi\\
F_0 &= -muL_\phi N_\delta + L_\phi N_\delta Y_r - L_\phi N_rY_\delta + hum_sN_\phi Y_\delta - hum_sN_\delta Y_\phi\\
H_2 &= -muI_{xz}N_\delta - huI_zm_sY_\delta\\
H_1 &= -\text{ hum }_sN_\delta Y_r + I_{xz}N_\delta Y_\beta + \text{ hum }_sN_rY_\delta - I_{xz}N_\beta Y_\delta\\
H_0 &= \text{ hum }_sN_\delta Y_\beta - \text{ hum }_sN_\beta Y_\delta
\end{aligned}
$$

According to Formula (1) and (8), the transfer function from the rotation angle of steering wheel $\theta_{sw}(s)$ to the rotation angle of front wheel $\delta(s)$ can be expressed as

$$
\frac{\delta(s)}{\theta_{sw}(s)} = \frac{A_pr_pKK_aK_s + K_sq}{X_2s^2 + Y_2s + Z_2 + \frac{q2dk_1}{n_2}\left(\frac{a}{u}\frac{w_r(s)}{\delta(s)} + \frac{\beta(s)}{\delta(s)} + E_1\frac{\phi(s)}{\delta(s)}\right)}
\tag{9}
$$

where

$$
\begin{cases}
\mathrm{X}_2 = \mathrm{m}_rr_p^2qn_1 + n_1n_2J_mA_pr_p\\
Y_2 = \left(B_rqr_p^2 + n_2B_mA_pr_p + \frac{\rho q^2n\eta_vA_p^2r_p^2}{2C_q^2A_1^2}\right)n_1\\
Z_2 = \left(A_pr_pKK_aK_s + K_sq\right)n_1 - \frac{2qdk_1}{n_1}
\end{cases}
$$

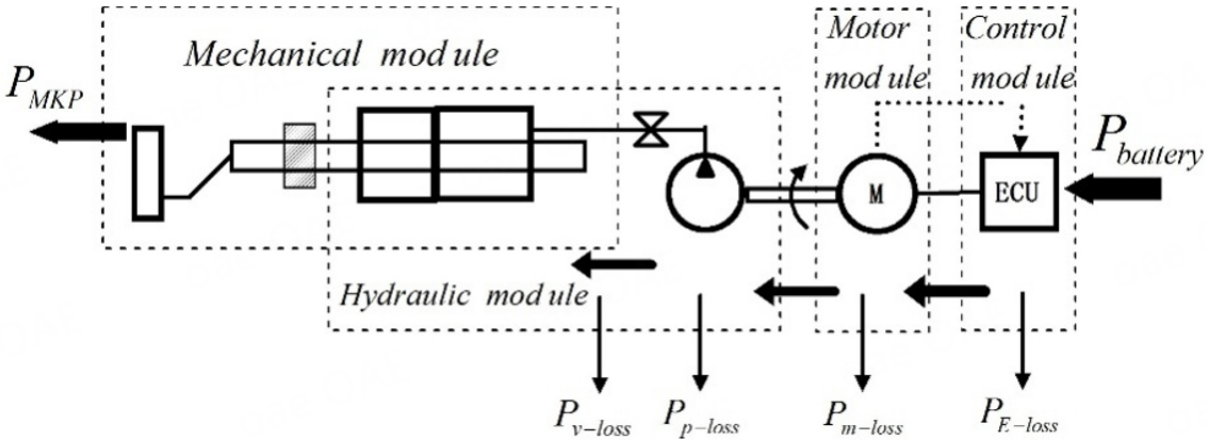

Figure 2. The schematic diagram of energy flow.

In this paper, the transfer function from the yaw velocity $\omega_r(S)$ to steering wheel $\theta_s(S)$ is defined as the steering sensitivity, expressed as

$$\frac{\omega_r(s)}{\theta_{sw}(s)} = \frac{\omega_r(s)}{\delta(s)} \frac{\delta(s)}{\theta_{sw}(s)} \tag{10}$$

Similar to steering road feel, the steering sensibility is also measured by the average frequency power in the range of 0-40 Hz and computed as

$$F_l = \frac{1}{2\pi\omega_0} \int_0^{\omega_0} \left| \frac{\omega_r(s)}{\theta_h(s)} \right|_{j=j\omega}^2 d\omega \tag{11}$$

2.2.3 Steering energy loss

Compared with traditional HPS systems, energy consumption of EHPS systems is greatly reduced. However, it still has a huge potential for energy saving. The schematic diagram of the energy flow of the EHPS system is shown in Figure 2.

The total energy of the steering system is supplied by the battery. One part of the energy is supplied to the ECU,and the energy loss is denoted as P_{E-loss}. The other part is supplied to the drive motor, which drives the hydraulic pump according to the ECU command. The energy loss of the drive motor is denoted as P_{m-loss}. The hydraulic pump pumps the hydraulic oil into rotary valve, and the energy losses of the two are denoted as P_{p-loss} and P_{v-loss}, respectively[9,14]. Thus, the total energy loss can be calculated as

$$P = P_{E-loss} + P_{m-loss} + P_{p-loss} + P_{v-loss} \tag{12}$$

where

$$\begin{cases} P_{E-\text{loss}} = R_a i^2 + \frac{U_s^2}{R_{\text{elec}}} \\ P_{m-\text{loss}} = \left[\frac{\frac{B_v n\pi}{30} + T_{Lo}}{K_a} r_a + \frac{k_e n\pi}{30} - K_a \omega(t) \right] i \\ P_{p-\text{loss}} = \frac{\rho}{8C_q^2} \left[\left(\frac{Q_S - A_P \dot{\theta} P r_P}{A_2} \right)^2 + \left(\frac{Q_S + A_P \dot{\theta} P r_P}{A_1} \right)^2 \right] (qn - Q_S) \\ P_{v-\text{loss}} = \frac{\rho}{8(C_q A_1)^2} \left(\frac{Q_s}{4} + A_p \frac{dx_r}{dt} \right)^3 + \frac{\rho}{8(C_q A_2)^2} \left(\frac{Q_s}{4} - A_p \frac{dx_r}{dt} \right)^3 \\ i = \frac{J_m}{K_a} \frac{d\omega(t)}{dt} + \frac{B_d}{K_a} \omega(t) + \frac{T_c}{K_a} \end{cases}$$

Table 1. The basic parameter of EHPS system

Name	Value	Name	Value
m/kg	4495	C_{21}/(N•m/rad)	14,130
m_s/kg	3350	C_{23}/(N•m/rad)	71,200
I_x/kg•m^2	2510	C_{a1}/(N•m•s/rad)	4,000
I_{xz}/kg•m^2	2810	C_{a1}/(N•m•s/rad)	3,800
I_z/kg•m^2	18800	d/m	0.23
k_1/(N/rad)	-2900	J_{sw}/kg•m^2	0.04
k_2/(N/rad)	-2900	C_q	0.62

Table 2. The initial value and range of each variable

Design variable	Initial value	Lower	Upper
A_p (m^2)	$1.2*10^{-4}$	$0.5*10^{-4}$	$2*10^{-4}$
p_b (m)	0.008	0.003	0.01
K_s (N/m)	80	30	150
J_m/kg•m^2	$5*10^{-3}$	10^{-3}	10^{-2}
r_p (m)	0.05	0.01	0.1
w (m)	10^{-3}	10^{-4}	$2*10^{-3}$

3. INTEGRATION OPTIMIZATION

As mentioned above, the optimization of EHPS system involves three evaluation indexes, steering road feel, steering sensitivity, and steering energy loss. Therefore, A multi-objective collaborative optimization model has been built, which simplifies the system decoupling, and the multi-objective optimization algorithm is applied to the model for a Pareto optimal solution set. Besides, the basic parameters of the EHPS system are shown in Table 1.

3.1. Optimization model

Based on collaborative optimization theory, the main system is divided into three independent subsystems, which is convenient for parallel computation and reduces the optimization time. In the main system, three optimization objectives, steering road feel, steering sensibility and energy loss, are optimized by multi-objective optimization algorithm. Besides, the consistency constraint of design parameters is taken as the optimization goal of each subsystem, and the sequential quadratic programming (NLPQL) algorithm is used to optimize each system.

In this paper, the effective area of piston A_p, the moment of inertia of motor J_m, the stiffness coefficient K_s, the stator thickness p_b, the gap width of rotary valve and the radius of the rack and pinion r_p are selected as the optimization variables. The initial value and design scope of each variable are given in Table 2.

The main system of optimization model is given by

$$\begin{cases} Minimize \quad P \\ Minimize \quad F_l \\ Maximize \quad S_c \\ Design \quad Variable \quad Bounds: \\ \qquad 3 \le T_p \le 5 \\ Z_L \le Z\left(A_p, p_b, K_s, J_m, r_p, w\right) \le Z_U \\ \qquad R_{1,2,3} \le 0.01 \end{cases} \tag{13}$$

where T_p is effective power torque, which is computed by

$$T_p = A_p r_p p_{ab} \tag{14}$$

where

$$\begin{cases} p_{ab} = \frac{\rho}{8\left(C_q A_{f2}\right)^2}\left(qn\eta_v - A_p r_p \dot{\theta}_p\right)^2 - \frac{\rho}{8\left(C_q A_{f1}\right)^2}\left(qn\eta_v + A_p r_p \dot{\theta}_p\right)^2 \\ A_{f1} = NL[w + R\left(\theta_z - \theta_p\right)] \\ A_{f2} = NL[w - R\left(\theta_t - \theta_p\right)] \end{cases}$$

The first subsystem named as energy loss is given by

$$\begin{cases} Minimize \\ R_1 = \left(1 - A'_p/A_p\right)^2 + \left(1 - p'_b/p_b\right)^2 \\ \quad + \left(1 - J_m/J'_m\right)^2 + \left(1 - r'_p/r_p\right)^2 + \left(1 - w'/w\right)^2 \\ Design \quad Variable \quad Bounds: \\ \quad 3 \le T'_p \le 5 \\ \quad x_L \le x\left(A'_p, p'_b, K'_s, J'_m, r'_p, w'\right) \le x_U \end{cases} \tag{15}$$

The second subsystem named as road feel is given by

$$\begin{cases} Minimize \\ R_2 = \left(1 - A''_p/A_p\right)^2 + \left(1 - p''_b/p_b\right)^2 \\ \quad + \left(1 - r''_p/r_p\right)^2 + \left(1 - J_m/J''_m\right)^2 + \left(1 - K''_s/K_s\right)^2 \\ Design \quad Variable \quad Bounds: \\ \quad 3 \le T''_p \le 5 \\ \quad x_L \le x\left(A''_p, p''_b, K''_s, J''_m, r''_p\right) \le x_U \end{cases} \tag{16}$$

The third subsystem named as steering sensibility is given by

$$\begin{cases} Minimize \\ R_3 = \left(1 - A'''_p/A_p\right)^2 + \left(1 - p'''_b/p_b\right)^2 + \left(1 - K'''_s/K_s\right)^2 \\ \quad + \left(1 - J'''_m/J_m\right)^2 + \left(1 - r'''_p/r_p\right)^2 + \left(1 - w'''/w\right)^2 \\ Design \quad Variable \quad Bounds: \\ \quad 3 \le T'''_p \le 5 \\ \quad x_L \le x\left(A'''_p, p'''_b, K'''_s, J'''_m, r'''_p, w'''\right) \le x_U \end{cases} \tag{17}$$

According to the above models, the multi-objective collaborative optimization model of EHPS is showed in Figure 3.

3.2. Multi-objective optimization algorithm

The NSGA-II algorithm has excellent global search performance and is often used in multi-objective optimization. On the one hand, the NSGA-II introduces an elite strategy in the process of ranking, which avoids the loss of non-dominated individuals in the evolution process and speeds up the convergence speed of the algorithm. On the other hand, the NSGA-II improves the crowded-comparison approach, which ensures the diversity of the next generation and enhances the global exploratory capability of the algorithm.

The main steps of NSGA-II algorithm can be depicted as follows.

(1) Generate the initial population P_0 at random and the size of P_0 is N;

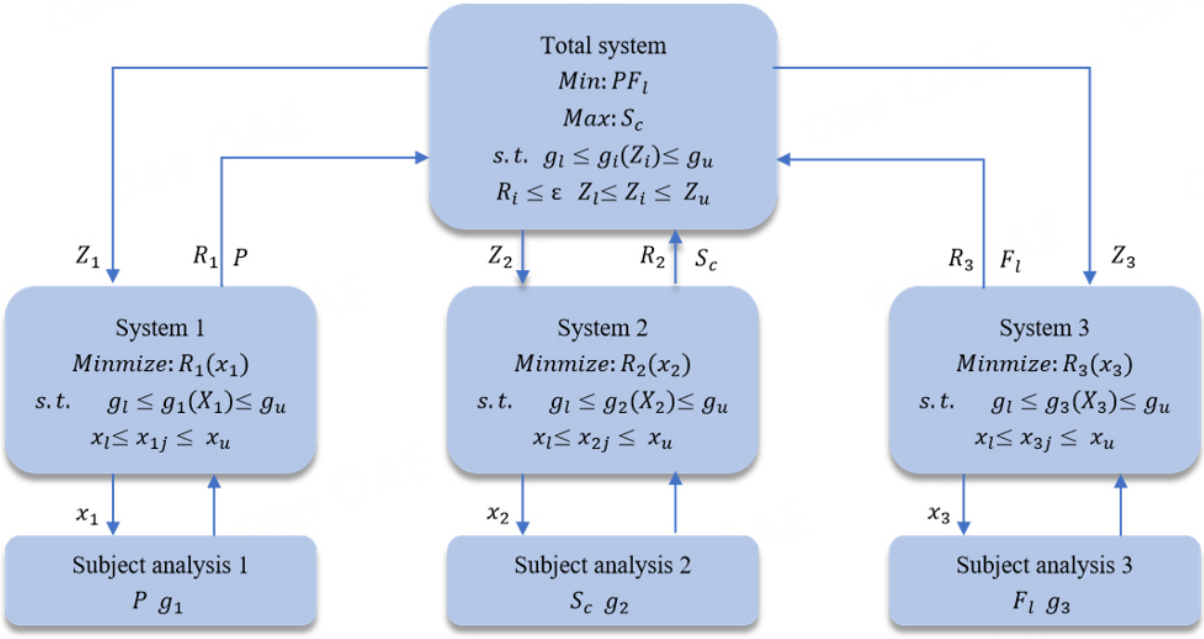

Figure 3. Optimization model of EHPS.

(2) Calculate the fitness degree of each individual by fitness function, sorting all individuals according to non-dominated regulation;

(3) Generate the next population $Q_t(t) \geq 1$ by crossover and mutation, and the size of Q_t is N. Forming a new population R_t consisted of P_t and Q_t;

(4) Calculate the fitness degree and crowd degree for each individual. Then, select N individuals to constitute a new population P_{t+1} according to the non-dominated regulation;

(5) $t = t + 1$;

(6) Run Step 3 to Step 5 repeatedly until t equals to the maximum generation.

The flowchart of the NSGA-II algorithm is shown in Figure 4.

3.3. Optimization results

According to the established multi-objective collaborative optimization model of the EHPS system, the NSGA-II is applied to the main system for the overall optimization of evaluation indexes, and the NLPQL algorithm is applied to each subsystem for the consistency of design variables. Additionally, the multi-objective particle swarm optimization algorithm (MOPSO) and NCGA multi-objective optimization algorithms are applied to the main system, and the NSGA-II algorithm is used to optimize the whole EHPS system. The solution set distribution of the optimization results is shown in Table 3, and the multi-objective optimization results are shown in Table 4.

Table 4 shows the distribution of the Pareto solutions obtained by different multi-objective algorithms. It should be noted that all algorithms are executed 2000 times.

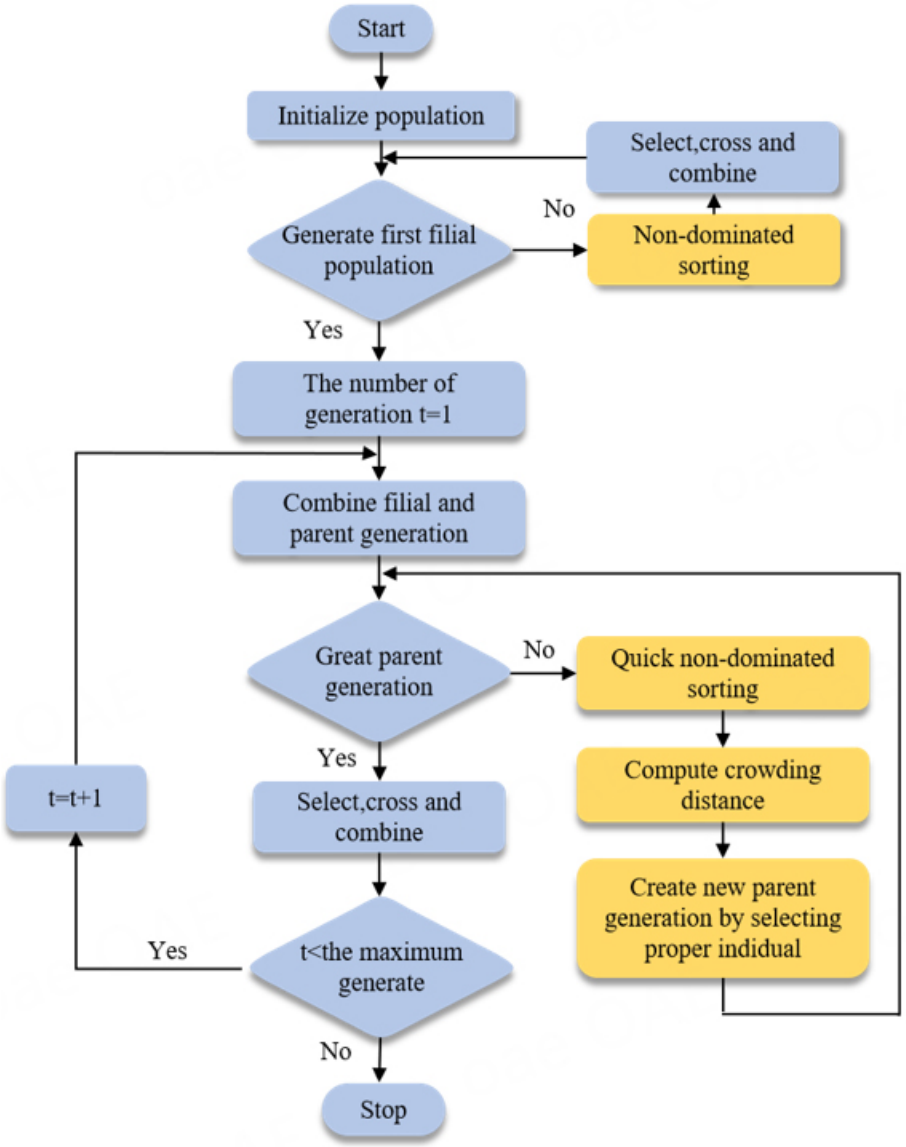

Figure 4. The flowchart of NSGA-II.

Firstly, multi-objective optimization method and multi-objective collaborative optimization method are compared. The distribution of the Pareto solutions obtained by only the NSGA-II is similar to the result by the NSGA-II with CO. 278 Pareto solutions are obtained by the NSGA-II with CO, and form a near-complete Pareto front. However, the number of Pareto solutions (104) obtained by the multi-objective optimization (NSGA-II) is too few to form a near-complete Pareto front. Furthermore, due to the insufficient number of solutions, poor non-dominant solutions cannot be eliminated, resulting in a low quality of the optimization solution set. Thus, it could be concluded that the multi-objective collaborative optimization has better solution set diversity and higher solution quality than the multi-objective optimization.

Secondly, the results obtained by CO combing with different multi-objective algorithms are compared. The MOPSO gets 53 Pareto solutions, while the NCGA and the NSGA-II have 269 and 278 Pareto solutions, respectively. Due to the neighborhood cultivation mechanism of the NCGA algorithm, excellent parent generations could be preserved in the next generation, which guarantees more Pareto solutions obtained, and the Pareto solutions distribution is more concentrated. In terms of NSGA-II algorithm, the elitist strategy is introduced;

Table 3. The distribution of Pareto solutions

	Pareto solutions
NSGA-II	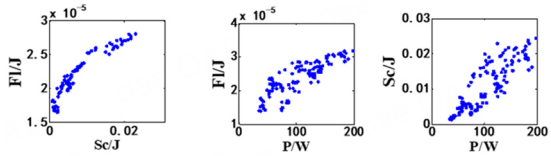
NSGA-II (CO)	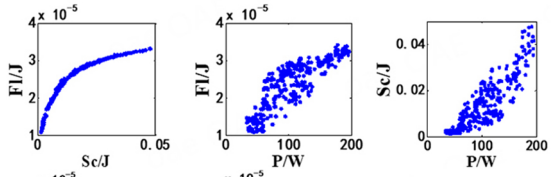
MOPSO (CO)	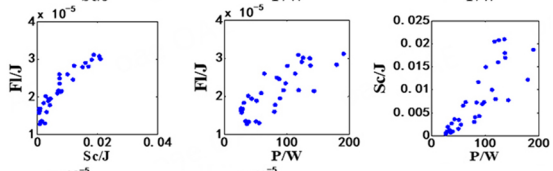
NCGA (CO)	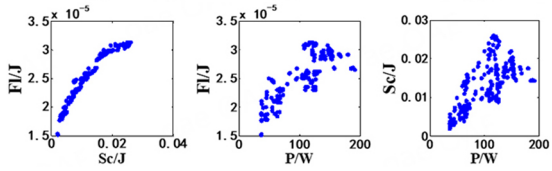

Table 4. Optimal result

Design variable	Initial value	NSGA-II	NSGA-II (CO)	MOPSO (CO)	NCGA (CO)
A_p (m^2)	$1.2*10^{-4}$	$1.21*10^{-4}$	$1.79*10^{-4}$	$1.24*10^{-4}$	$1.50*10^{-4}$
p_b (m)	0.008	0.0034	0.0044	0.0035	0.0042
K_s (N/m)	80	32.45	31.7	41.4	36.2
J_m (kg· m^2)	$6*10^{-3}$	$1.26*10^{-3}$	$1.82*10^{-3}$	$1.12*10^{-3}$	$1.78*10^{-3}$
r_p (m)	0.06	0.037	0.032	0.034	0.021
w (m)	10^{-3}	$5.88*10^{-4}$	$6.76*10^{-4}$	$5.59*10^{-4}$	$5.27*10^{-4}$
F_l (J)	$3.24*10^{-5}$	$2.81*10^{-5}$	$2.65*10^{-5}$	$2.61*10^{-5}$	$3.13*10^{-5}$
S_c (J)	0.016	0.023	0.027	0.021	0.026
P (W)	132.41	124.46	118.28	120.24	116.34

thus, excellent parent generations information could also be preserved in the next generation. Meanwhile, the sorting method based on crowding distance ensures that the Pareto solutions are distributed uniformly.

The optimization results are shown in Table 4. Through the multi-objective collaborative optimization method, the average frequency domain energy of steering sensibility is 2.65×10^{-5} J, which is decreased by 19.2% compared with the initial value. The average frequency domain energy of the steering road feel is 0.027 J, and it is 1.69 times bigger than the initial value. Moreover, the steering energy loss is reduced to 118.28 W, which is reduced by 10.8% compared to the initial value. Besides, compared to the results by only the NSGA-II algorithm, the optimization objectives have been further improved by the NSGA-II algorithm with CO. The average frequency domain energy of steering sensitivity is further reduced by 5.69%. The average frequency domain energy of the steering road feel is further increased by 17.39%, and the steering energy loss is further reduced by 5.00%. Furthermore, the optimization by the NSGA-II algorithm with CO has the best comprehensive performance compared with the results obtained by CO with the other two multi-objective algorithms.

The Bode diagram of the steering road feel step response is shown in Figure 5. The amplitude in the 0-40 Hz range has been improved compared to that before optimization. Especially for the NSGA-II with CO method, it gets the highest average frequency domain energy among the optimization algorithms, which means that

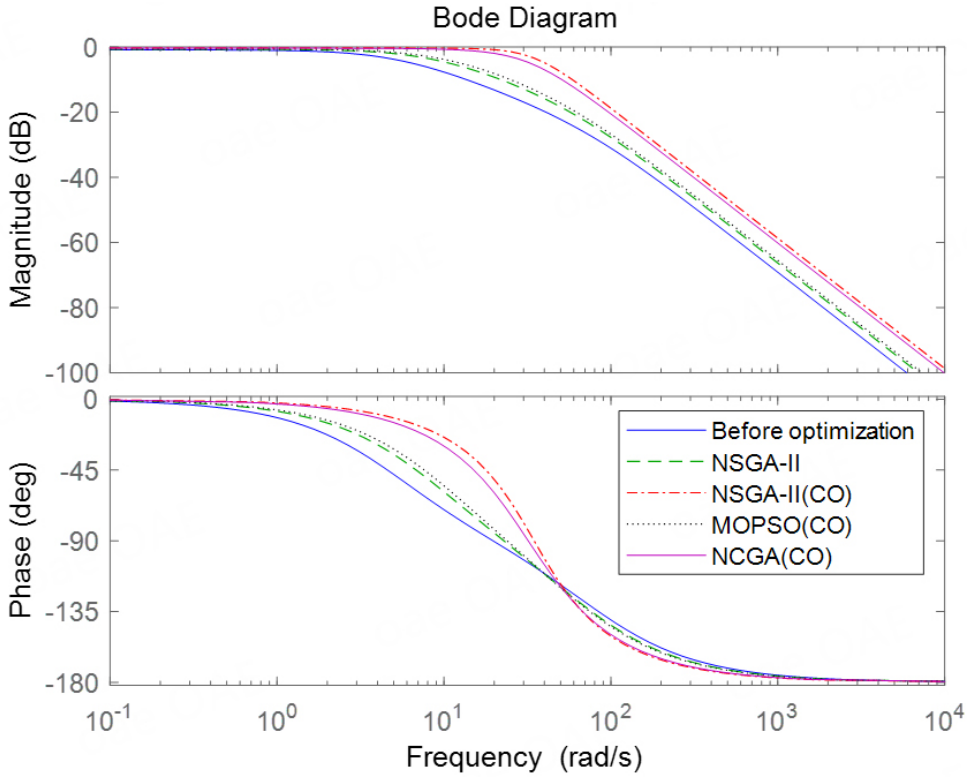

Figure 5. Step response Bode diagram of steering road feel.

the information from the 0-40 Hz range of the road surface can be transmitted to the driver better.

The Bode diagram of the steering sensibility step response is shown in Figure 6. Although the NSGA-II with CO method does not obtain the least steering sensibility, the optimization result obtained is still greatly improved compared to that before optimization.

Therefore, it could be concluded that multi-objective collaborative optimization can improve the steering road feel and reduce the steering sensitivity while improving the economy of the steering system. At the same time, the collaborative optimization of NSGA-II with CO has better solution sets diversity and comprehensive optimization results.

4. CONCLUSIONS

(1) On the basis of the EHPS system dynamics model and energy flow analysis, the evaluation index formula of the steering system is derived for the first time, including steering road feel, steering sensibility, and steering energy loss. In addition, considering the coupling relationship between subsystems, a multi-objective collaborative optimization model is established to achieve parallel computing.

(2) The multi-objective collaborative optimization further improves the performance of the EHPS system compared with the multi-objective optimization. Besides, the NSGA-II algorithm shows the best comprehensive performance in optimizing the design parameters of the EHPS system in the comparison of CO combing with multi-objective algorithms.

(3) The optimization results show that the EHPS system is optimized successfully and multiple evaluation in-

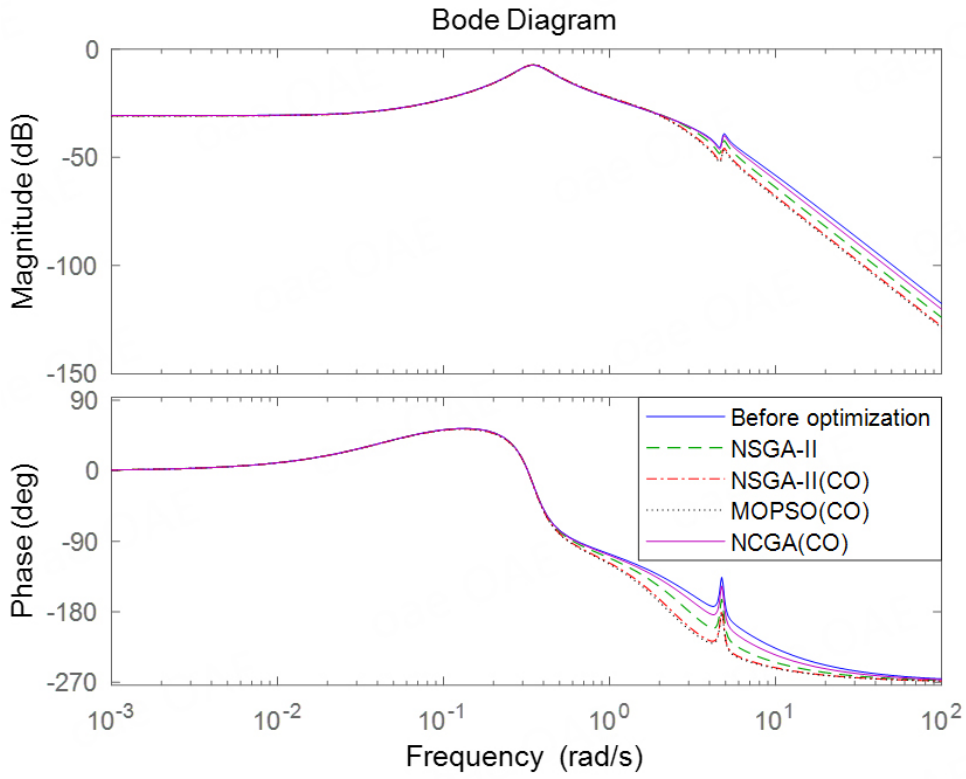

Figure 6. Step response Bode diagram of steering sensibility.

dexes could be improved simultaneously. Besides, the optimization is beneficial for promoting the application of the EHPS system in the area of power steering and also serves as a good example for the optimization of electric power steering systems and active steering systems.

DECLARATIONS

Acknowledgments

The authors would like to thank the reviewers for their thoughtful comments and efforts towards improving our manuscript.

Authors' contributions

Conceptualization: Cui T
Experiment and analyze data: Cui T, Wang S
Manuscript drafting: Cui T, Chen X
Manuscript edition and review: Cui T, Wang S, Qu Y, Chen X

Availability of data and materials

Not applicable.

Financial support and sponsorship

The research presented within this article is supported by the Fundamental Research Funds for the Central Universities (Grant No. Jz2021HGQA0286).

Conflicts of interest

All authors declared that there are no conflicts of interest.

Ethical approval and consent to participate

Not applicable.

Consent for publication

Not applicable.

Copyright

Appendix for Nomenclature

REFERENCES

1. Liu C, Wang C, Zhao W, Guo Z. Displacement characteristics hierarchical control of electro-hydraulic compound steering for commercial vehicle. *J Mech Eng Sci* 2022;236:6395-409. DOI
2. Guo ZQ, Wu HX, Zhao WZ, et al. Coordinated control strategy for vehicle electro-hydraulic compound steering system. *J Automot Eng* 2020;235:732-43. DOI
3. Du H, Zhang QM, Chen SM, et al. Modeling, simulation, and experimental validation of electro-hydraulic power steering system in multi-axle vehicles. *J Automot Eng* 2019;233:317-32. DOI
4. Zhang L, Wang Z, Ding X, Li S, Wang Z. Fault-tolerant control for intelligent electrified vehicles against front wheel steering angle sensor faults during trajectory tracking. *IEEE Access* 2021;9:65174-86. DOI
5. Ding X, Wang Z, Zhang L. Hybrid control-based acceleration slip regulation for four-wheel-independent-actuated electric vehicles. *IEEE Trans Transp Electrific* 2021;7:1976-89. DOI
6. Zhang L, Zhang Z, Wang Z, Deng J, Dorrell DG. Chassis coordinated control for full X-by-wire vehicles-a review. *Chin J Mech Eng* 2021;34:1-25. DOI
7. Du H, Wang L, Chen JD, et al. Adaptive fuzzy radial basis function neural network integral sliding mode tracking control for heavy vehicle electro-hydraulic power steering systems. *J Automot Eng* 2020;234:872-86. DOI
8. Lin L, Wang W, Liu ZQ. Modeling and simulation of slip frequency control for induction motor in electric vehicle EHPS system. *Appl Mech Mater*2014;635-7:1251-5. DOI
9. Kim SH, Min CS, Chong NC. Development of EHPS motor speed map using HILS system. *IEEE Trans Veh Technol* 2013;62:1553-67. DOI
10. Ye M, Wang Q, Jiao S. Robust H_2/H_∞ control for the electrohydraulic steering system of a four-wheel vehicle. *Math Probl Eng* 2014;4:1-12. DOI
11. Hur J. Characteristic analysis of interior permanent-magnet synchronous motor in electrohydraulic power steering systems. *IEEE Trans Industr Inform* 2008;55:2316-23. DOI
12. Cui TW, Zhao WZ, Wang CY. Parametric optimization of a steering system based on dynamic constraints collaborative optimization method. *Struct Multidiscipl Optim* 2020;61:787-802. DOI
13. Zhao WZ, Wang CY, Li YJ, et al. Integrated optimisation of active steering and semi-active suspension based on an improved memetic algorithm. *Int J Veh Des* 2015;67:388-405. DOI
14. Crews JH, Mattson MG, Buckner GD. Multi-objective control optimization for semi-active vehicle suspensions. *J Sound Vib* 2011;330:5502-16. DOI
15. Chen S, Shi T, Wang D, Chen J. Multi-objective optimization of the vehicle ride comfort based on kriging approximate model and NSGA-II. *J Mech Sci Technol* 2015;29:1007-18. DOI
16. Deb A, Srinivas GR, Chou CC. Development of a practical multi-disciplinary design optimization (MDO) algorithm for vehicle body design. *SAE Tech Pap* 2016;1:1537. DOI
17. Cui TW, Zhao WZ, Tai K. Optimal design of electro-hydraulic active steering system for intelligent transportation environment. *Energy* 2021;214:118911. DOI
18. Zhou PZ, Du JB, Lv ZH. Simultaneous topology optimization of supporting structure and loci of isolators in an active vibration isolation system. *Comput Struct* 2018;194:74-85. DOI
19. Zhao WZ, Wang YQ, Wang CY. Multidisciplinary optimization of electric-wheel vehicle integrated chassis system based on steady endurance performance. *J Clean Prod* 2018;186:640-51. DOI
20. Martins JRRA, Lambe AB. Multidisciplinary design optimization: a survey of architectures. *AIAA J* 2013;51:2049-75. DOI
21. Park EJ, Luz LFD, Suleman A. Multidisciplinary design optimization of an automotive magnetorheological brake design. *Comput Struct* 2008;86:207-16. DOI

22. Zadeh PM, Toropov VV, Wood AS. Metamodel-based collaborative optimization framework. *Struct Multidiscipl Optim* 2009;38:103-15. DOI
23. Zhou G, Ma ZD, Cheng A, et al. Design optimization of a runflat structure based on multi-objective genetic algorithm. *Struct Multidiscipl Optim* 2015;51:1-9. DOI
24. Huang H, An H, Wu W, Zhang L, Wu B, Li W. Multidisciplinary design modeling and optimization for satellite with maneuver capability. *Struct Multidiscipl Optim* 2014;50:883-98. DOI
25. Mitra AC, Patil MV, Banerjee N. Optimization of vehicle suspension parameters for ride comfort based on RSM. *J Inst Eng* 2015;96:165-73. DOI

Huang *et al. Complex Eng Syst* 2023;3:2
DOI: 10.20517/ces.2022.43

Complex Engineering Systems

Research Article

Open Access

Generation of high definition map for accurate and robust localization

Zhengjie Huang[1], Sijie Chen[1], Xing Xi[1], Yanzhou Li[1], Ya Li[2], Shuanglin Wu[3]

[1]School of Automation, Guangdong University of Technology, Guangzhou 510006, Guangdong, China.
[2]Ningbo Artificial Intelligence Institute, Shanghai Jiaotong University, Ningbo 315000, Zhejiang, China.
[3]State Key Laboratory of Acoustics, Institute of Acoustics, Chinese Academy of Sciences, Beijing 100190, China.

Correspondence to: Dr. Yanzhou Li, School of Automation, Guangdong University of Technology, No.100, Waihuan Xi Road, Guangzhou 510006, Guangdong, China. E-mail: lyz19921207@163.com

How to cite this article: Huang Z, Chen S, Xi X, Li Y, Li Y, Wu S. Generation of high definition map for accurate and robust localization. *Complex Eng Syst* 2023;3:2. http://dx.doi.org/10.20517/ces.2022.43

Received: 17 Oct 2022 **First Decision:** 24 Nov 2022 **Revised:** 2 Dec 2022 **Accepted:** 11 Jan 2023 **Published:** 31 Jan 2023

Academic Editor: Hamid Reza Karimi **Copy Editor:** Fanglin Lan **Production Editor:** Fanglin Lan

Abstract

This paper presents a framework for generating high-definition (HD) map, and then achieves accurate and robust localization by virtue of the map. An iterative approximation based method is developed to generate a HD map in Lanelet2 format. A feature association method based on structural consistency and feature similarity is proposed to match the elements of the HD map and the actual detected elements. The feature association results from the HD map are used to correct lateral drift in the light detection and ranging odometry. Finally, some experimental results are presented to verify the reliability and accuracy of autonomous driving localization.

Keywords: High definition map, factor graph optimization, localization, reprojection error

1. INTRODUCTION

In recent years, vehicle localization has been treated as an important part of an autonomous driving system. However, conventional odometry methods have drift problems with long-term use. An inertial navigation system (INS) will likely fail in scenarios with poor GNSS signals, such as tunnel and urban canyon scenarios [1]. For the sake of more accurate localization, multisensor fusion is developed to compensate for the respective deficiencies of various sensors. HD maps, as stable prior information, can provide reliable location constraints.

Fusion localization methods based on HD maps have been a significant research hotspot in recent years.

For HD maps, some computer-aided generation methods have emerged[2,3]. However, lane lines obtained using these methods are a series of 2-dimensional point sets, which occupy large storage space and do not carry elevation information. Some researchers store road features in point clouds and use point cloud registration methods to determine vehicle positions[4,5]. However, point cloud formats have disadvantages such as high coupling, difficulty in maintaining, and unfavorable object classification. For localization, some researchers reduce localization errors by matching road surface features, e.g. manhole covers[6–12]. However, the visibility of road features is easily affected by illumination, which makes the matching performance differ greatly at different times and results in unstable localization.

In this paper, the main work focuses on two aspects: First, a computer-aided generation method for HD maps is proposed. Currently, most papers consider the lane lines are in 2D plane when the lane line fitting is implemented. These methods are almost unusable in scenarios such as overpasses and culverts[13–16]. To broaden the use of HD maps, it is necessary to develop 3D fitting lane lines. Second, an accurate multisensor fusion localization method using generated HD map and existing odometry is proposed. It is worth noting that cumulative errors will occur if the localization method is only based on odometry. Thus, a positional constraint that has no connection with error is required to correct the estimated position. The contributions of this paper are summarized as follows:

1. We propose a method based on an iterative approximation to generate the 3D curve of lane lines. The spatial parameterized curve fitted by the proposed algorithm, which is global C^1 continuous, has broader applicability than the 2D curve equation. This method not only effectively reduces the number of parameters of the spline curve but also ensures the accuracy of the curve.
2. We separate the lanes and store them in a particular HD map format instead of holding them as semantic information in a point cloud. For the HD maps nonuniform sampling point problem, a method based on numerical integration is proposed to achieve uniform sampling over the arc length.
3. We propose a method to associate the elements in the HD map and the other elements in the perception results.In this paper, the basic elements of the HD map and the complete feature associations are formulated with their respective similarity evaluation metrics, considering the matching time, similarity and local structure consistency.
4. We transform the localization problem of fusing HD maps into a graph optimization problem. Based on the HD map and perceptual image feature association results, a lateral constraint is applied to the odometry localization results, and accurate, low-cost localization results are obtained.

2. RELATED WORKS

2.1. Generation of lane curve equations

Chen *et al.*[14] demonstrated that a cubic Hermite spline (CHS) can describe line segments, arc curves, and clothoids simultaneously and is a good choice for fitting lane lines. A CHS has at least C^1 continuity, which is more accurate in describing lane curves than a traditional segmented linear fold representation. Its uniform form allows fitting any lane curves parametrically using a sequence of feature points. Jo *et al.*[15] proposed a B-spline fitting method based on the optimal smoothing technique. Zhang *et al.*[16] proposed a lane line fitting method that considered a vehicle model to generate globally C^1 continuous lane lines that match the driving trajectory. Gwon *et al.*[17] proposed a segmented polynomial fitting method with sequential approximation, which outperformed B-spline and clothoid curves in terms of computational efficiency and modifiability.

2.2. Existing HD map formats

There is no unified standard for HD map formats, and various institutions and companies use different formats. The OpenDRIVE standard, developed by the Association for Standards in Automation and Measurement Sys-

tems (ASAM), has been used in simulations for some time and has good landing performance in some assisted driving models. The Navigation Data Standard (NDS) is a standard format for vehicle-level navigation databases jointly developed and published by vehicle manufacturers and automotive suppliers. The NDS format enables sharing of navigation data between different systems by separating the navigation data from the navigation software. Although OpenDRIVE and NDS are formats developed by more authoritative organizations, they need to be more open, as they provide only partial information to most developers. Therefore it is challenging to use them in practice[18,19].

Apollo OpenDRIVE is a modified version of OpenDRIVE to accompany the Baidu Apollo autonomous driving system. Instead of using geometric elements, it uses sequences of points to represent road elements. In addition, Apollo OpenDRIVE stores reference lines on the map and then describes the lane lines relative to the reference lines. This allows Apollo OpenDRIVE to express maps with higher accuracy than OpenDRIVE for the same map file size and also facilitates some calculations in the subsequent planning module.

In 2018, Poggenhans *et al.*[20] released the open source Lanelet2. Based on the OpenStreetMap (OSM) format, Lanelet2 has been extended and allowed direct access to many of the open source tools that accompany OSM. Benefiting from its complete toolkit, open architecture, and easily editable features, Lanelet2 not only allows the storage of information about roads, road signs, light poles, and buildings with precise geometry but also enables lane level and traffic-compliant routing.

2.3. Multisensor fusion localization

GNSS are widely spread in intelligent transport systems and offer a low-cost, continuous and global solution for positioning[21]. It can provide a more stable location. GNSS localization system has obvious disadvantages: significant errors and easy to be obscured. Therefore, scholars have increasingly recognized multisensor fusion as necessary in recent years. Simultaneous localization and mapping (SLAM) is a technology that constantly builds and updates environmental information by sensing things in an unknown environment while tracking their position in the background. SLAM is generally divided into light detection and ranging (LiDAR)-based SLAM, such as LOAM[22], LeGO-LOAM[23], LINS[24], and LIO-SAM[25], and vision-based SLAM, such as ORB-SLAM[26], VINS[27,28]. If the localization relies solely on LiDAR or cameras, position estimation errors will accumulate over a long time and distance. An HD map, as a globally consistent data source, can also provide reliable global location constraints. Multisensor fusion localization algorithms combined with HD map lane-level localization algorithms will be more accurate and have great potential.

2.4. Localization based on HD map

Scholars continue to reduce the error by matching pavement marking features or lane line curvature based on existing localization[6–12]. However, the visibility of road markings is affected by light. The visibility of different markings on the same road segment varies greatly at different periods, making it difficult to achieve stable positioning performance. At the same time, these efforts do not consider the common function of road elements in localization and planning, and these methods can only use the generated road elements in localization.

3. SYSTEM OVERVIEW

The proposed system consists of three parts. The first part is lane line fitting. An inverse lane line perspective mapping method combined with ground equations is discussed. An iterative approximation-based process of fitting piecewise CHS curves is proposed. This method satisfies the requirement of small data storage and ensures the continuity of lanes.

The second part is the HD map postprocessing. The data structure and coordinate system required for the HD

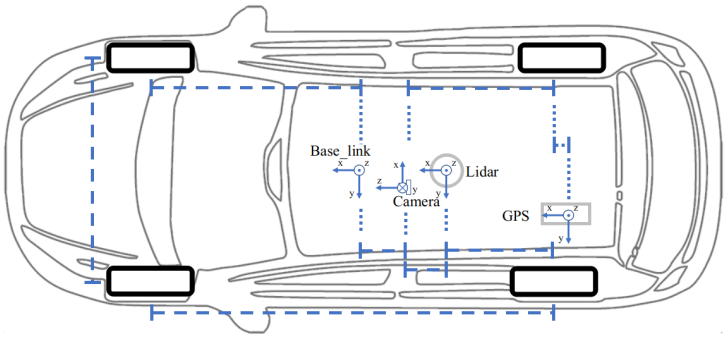

Figure 1. The coordinate system of the vehicle.

Figure 2. Lane detection data.

map are discussed. We use a numerical integration method to calculate the parametric curve arc lengths. In this way, the parametric scale equidistant curves are transformed into arc-length scale middle curves, making the curve structure more uniform.

The third part is a fusion localization method based on HD maps and odometry. A method for feature association between current HD map information and the camera's real-time perceptual features is investigated. A respective similarity evaluation metric is formulated for different essential elements in the HD map. According to the accumulated confidence smoothing, the results are smoothed on the time scale and converted into a graph optimization problem. Finally, the amount of computation for graphics optimization is reduced using a sliding window method and improved keyframe selection.

The KITTI dataset is used for autonomous driving and mobile robot research [29]. This study uses only camera 2 and the synchronized and corrected data in the KITTI dataset. Therefore, we add some definitions based on KITTI's original definitions. Taking camera 2 as the origin to establish a camera coordinate system, the intersection of the vertical line from the midpoint of the front and rear axles of the vehicle (the middle of the four wheels) to the ground and the ground is taken as the vehicle center point, and the base_link coordinate system is established. The positive direction of the x-axis is forward along the vehicle's driving path, the y-axis points to the left side of the vehicle's driving direction, and the z-axis is vertical upward. The vehicle's coordinate system is shown in Figure 1.

4. HD MAP GENERATION

We discuss the generation of HD maps with the lane line detection results already available from existing experimental data, and the test images are from the KITTI dataset [29]. An example of lane line data is shown in Figure 2. The lane line data are stored as line segments. Each segment is a lane consisting of several points.

4.1. Inverse perspective mapping with ground equation

The projection equation of the camera is as follows:

$$Z_{\mathrm{c}}\begin{bmatrix}\boldsymbol{P}_{\mathrm{uv}}\\1\end{bmatrix}=\boldsymbol{K}\boldsymbol{P}_{\mathrm{c}}=\boldsymbol{K}\boldsymbol{T}_{\mathrm{cb}}\boldsymbol{P}_{\mathrm{b}} \tag{1}$$

where $\boldsymbol{P}_{\mathrm{c}}=[X_{\mathrm{c}},Y_{\mathrm{c}},Z_{\mathrm{c}}]^{\mathrm{T}}$ is the coordinates of a point under the camera coordinate system, and $\boldsymbol{K}$ is the intrinsic matrix of the camera. $\boldsymbol{Z}_{\mathrm{c}}$ is the z-axis coordinate of the actual ground point in the camera coordinate system. $\boldsymbol{P}_{\mathrm{b}}$ is the coordinates of a point in the vehicle coordinate system, $\boldsymbol{P}_{\mathrm{uv}}=[u,v]^{\mathrm{T}}$ is the coordinates of a point in the pixel coordinate system, $\boldsymbol{T}_{\mathrm{cb}}$ represents transformation matrix from the camera to the vehicle coordinate system.

We calculate the ground equations in the LiDAR coordinate system as follows[30]:

$$\boldsymbol{n}_{\mathrm{l}}^{\mathrm{T}}\boldsymbol{P}_{\mathrm{l}}=\boldsymbol{n}_{\mathrm{l}}^{\mathrm{T}}\boldsymbol{T}_{\mathrm{lc}}\boldsymbol{P}_{\mathrm{c}}=\boldsymbol{n}_{\mathrm{c}}^{\mathrm{T}}\boldsymbol{P}_{\mathrm{c}}=-D \tag{2}$$

where $\boldsymbol{n}_{\mathrm{l}}$ is the vector normal to the ground plane in the LiDAR coordinate system, and $\boldsymbol{T}_{\mathrm{lc}}$ is the transformation matrix from the LiDAR to the camera coordinate system. $\boldsymbol{P}_{\mathrm{l}}$ is the point in the radar coordinate system. $\boldsymbol{n}_{\mathrm{c}}$ is the vector normal to the ground plane in the camera coordinate system.

Combining (1) and (2),

$$Z_c\begin{bmatrix}\boldsymbol{P}_{\mathrm{uv}}\\1\\0\end{bmatrix}=\begin{bmatrix}f_x&0&c_x&0\\0&f_y&c_y&0\\0&0&1&0\\A&B&C&D\end{bmatrix}\boldsymbol{P}_{\mathrm{c}}=\boldsymbol{M}\boldsymbol{T}_{\mathrm{cb}}\boldsymbol{P}_{\mathrm{b}} \tag{3}$$

where $\boldsymbol{M}$ is:

$$\boldsymbol{M}=\begin{bmatrix}\boldsymbol{K}&\boldsymbol{0}\\\boldsymbol{n}_{\mathrm{c}}^{\mathrm{T}}&D\end{bmatrix} \tag{4}$$

The physical meaning of D is the offset of the plane in the direction of the normal vector (after normalizing the normal vector $\boldsymbol{n}$). In the camera coordinate system, D in the ground equation cannot be zero. Therefore, it can be assumed that $\boldsymbol{M}$ is full rank.

Since the matrix $\boldsymbol{M}$ varies with the ground equation, its inverse matrix must be calculated for each subsequent frame, and the program overhead is significant. From the chunk matrix property, we can further obtain the following:

$$\frac{1}{Z_c}\boldsymbol{P}_{\mathrm{c}}=\begin{bmatrix}\boldsymbol{K}^{-1}&\boldsymbol{0}\\-D^{-1}\boldsymbol{n}_{\mathrm{c}}^{\mathrm{T}}\boldsymbol{K}^{-1}&D^{-1}\end{bmatrix}\begin{bmatrix}\boldsymbol{P}_{\mathrm{uv}}\\1\\0\end{bmatrix} \tag{5}$$

From (5), the program only needs to compute $\boldsymbol{K}^{-1}$ once in the initialization phase. Then, it is just a matter of computing $\boldsymbol{n}'^{\mathrm{T}}$ and D^{-1} in each subsequent frame of the program.

4.2. Piecewise cubic hermite spline fitting

A CHS curve is a cubic polynomial curve determined by the starting point p_0, the ending point p_1, the slope of the starting point d_0, and the slope of the ending point d_1. The equation of a parametric cubic polynomial curve is defined as:

$$\mathrm{F}_i(\boldsymbol{p}_i,\boldsymbol{p}_{i+1},\boldsymbol{d}_i,\boldsymbol{d}_{i+1},t)=\boldsymbol{P}_i\boldsymbol{H}\boldsymbol{t}=\begin{bmatrix}\boldsymbol{p_i}\\\boldsymbol{p_{i+1}}\\\boldsymbol{d_i}\\\boldsymbol{d_{i+1}}\end{bmatrix}^{\mathrm{T}}\begin{bmatrix}1-3t^2+2t^3\\3t^2-2t^3\\t-2t^2+t^3\\-t^2+t^3\end{bmatrix} \tag{6}$$

(6) represents the equation of the i-th segment of a CHS curve. A CHS curve has global C^1 continuity[16].

The problem of fitting the i-th segment of the curve to N_i points can be transformed into a minimization problem:

$$\min \sum_{k=0}^{N_i} \mathrm{err} = \min \sum_{k=0}^{N_i} \left\| \mathrm{F}_i(\boldsymbol{p}_i, \boldsymbol{p}_{i+1}, \boldsymbol{d}_i, \boldsymbol{d}_{i+1}, \boldsymbol{t}_i) - \boldsymbol{p}_{\boldsymbol{k}} \right\| \tag{7}$$

It is evident that in each segment of the curve except the first one, only the endpoint tangent vector $\boldsymbol{d}_{i+1}$ needs to be fitted. In (7), fitting a parametric curve equation needs to consider multiple minimization problems at the same time.

An algorithm for fitting a piecewise spatial CHS curve is proposed based on the idea of asymptotic approximation, as shown in the Algorithm 1. The main idea of the algorithm is to cyclically optimize $\boldsymbol{d_i}$, $\boldsymbol{d_{i+1}}$ and $\boldsymbol{t}$. That is, one parameter is optimized while keeping the other two parameters unchanged until each parameter is optimized N_{iter} times. To achieve global C^1 continuity, the vector tangent to the starting point of subsequent curves adopts the endpoint tangent vector of the previous segment. In this paper, $\mathrm{F}_i(\boldsymbol{d}_i)$ means that other quantities are left unchanged, and only $\boldsymbol{d}_i$ is changed, and the same is true for other variables. In this paper, the optimizer uses L-BFGS-B[31].

$$\begin{cases} \underset{\boldsymbol{d}_0, \boldsymbol{d}_1}{\arg\min} \sum_{k=0}^{N_0} \left\| \mathrm{F}_0(\boldsymbol{d}_0, \boldsymbol{d}_1) - p_k \right\| & i = 1 \\ \underset{\boldsymbol{d}_{i+1}}{\arg\min} \sum_{k=0}^{N_i} \left\| \mathrm{F}_i(\boldsymbol{d_{i+1}}) - p_k \right\| & i = 2, 3, \ldots N \end{cases} \tag{8}$$

Algorithm 1 CHS Curve Fitting with Asymptotic Approximation

N: Total number of curve segments.
i: The i-th curve, $i \in [1, N]$.
N_i: Point set size.
k: The k-th point in the set of points, $k \in [1, N_i]$.
t_k: The parameter corresponding to the kth point.
$\boldsymbol{t}_i$: The column vector consisting of t_k.
N_{iter}: Number of iterations.
for $i \in [1, N]$ **do**
  Initialization : $\boldsymbol{p}_i, \boldsymbol{p}_{i+1}$
  for $j \in [1, N_{\mathrm{iter}}]$ **do**
    $\boldsymbol{t}_i$ = L-BFGS-B $\left(\underset{\boldsymbol{t}}{\arg\min} \sum_{k=1}^{N_i} \mathrm{F}_i(\boldsymbol{t}_k) \right)$
    if $i == 1$ **then**
      $\boldsymbol{d}_i$ = L-BFGS-B $\left(\underset{\boldsymbol{d}_i}{\arg\min} \sum_{k=1}^{N_i} \mathrm{F}_i(\boldsymbol{d}_i) \right)$
    end if
    $\boldsymbol{d}_{i+1}$ = L-BFGS-B $\left(\underset{\boldsymbol{d}_{i+1}}{\arg\min} \sum_{k=1}^{N_i} \mathrm{F}_i(\boldsymbol{d}_{i+1}) \right)$
  end for
end for
return F

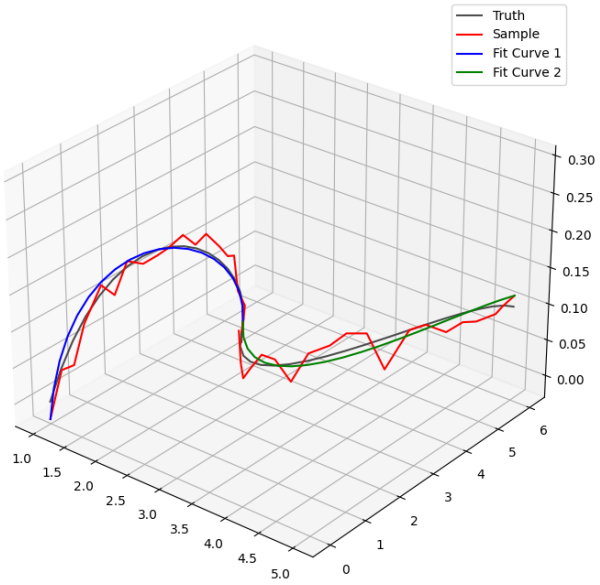

Figure 3. Curve fitting.

The traditional piecewise cubic Hermite interpolating polynomial (PCHIP)[32] algorithm fits a set of curves with four parameters every two points, so the number of parameters to be fitted increases exponentially with an increasing number of sampling points. The asymptotic approximation of the CHS curve fitting algorithm proposed in this section adds several sampling points to the curve fitting equation as constraint terms, which can effectively reduce the total number of parameters while ensuring that the curve is as close as possible to the remaining sampling points. As shown in Figure 3, the gray line is the actual curve, the red line is composed of 20 sampling points, and the blue and green lines are the curves fitted by the algorithm in this study. The smooth and continuous connection between the blue and green lines is evident in Figure 3. This shows that the algorithm's results in this study can still guarantee a certain accuracy in the case of more serious disturbances. This accuracy satisfies the need for lane line fitting.

4.3. Intersection completions

Considering that some roads prohibit left or right turns, it is not feasible to fix intersections through geometric relationships. In this study, we evaluate the intersection connection using the trajectory information of the vehicle driving. The vehicle driving trajectory is superimposed on the set of lane points. When the lane points near the vehicle driving route are less than a threshold value, the intersection is considered to be at that point.

The parameters of a CHS curve equation in an intersection (called virtual lanes) can be determined by combining the endpoint of the departure lane and its tangent vector with the start point of the entry lane and its tangent vector. That is, for the equation of virtual lanes at this intersection, the equation of a lane line in intersection F_I satisfies $F_I = F(\boldsymbol{p}_{prev}, \boldsymbol{p}_{next}, \boldsymbol{d}_{prev}, \boldsymbol{d}_{next}, t)$, where $\boldsymbol{p}_{prev}$ and $\boldsymbol{p}_{next}$ are the endpoint coordinates of the starting lane and the start point coordinates of the target lane, respectively, and $\boldsymbol{d}_{prev}$ and $boldsymbold_{next}$ are the endpoint tangent vector of the starting lane and the start point tangent vector of the target lane.

4.4. Arc length equalization of curves

In Lanelet2, a sequence of points is used to describe lane lines. This storage method has some advantages; path-planning algorithms with some processing can use this point sequence. In addition to manual adjustment to edit HD maps, they must also manipulate the point sequence and cannot be operated on the parameterized curve. In contrast, some scenarios require global smoothing of curves, such as lane visualization drawing.

Therefore, lane parameters and point sequences are stored in the map file in this study. Optimizing the curve equation after parameter t does not have a physical meaning. To make the spacing of sampling points on each section of the lane consistent, the arc length of the curve needs to be calculated and used to re-extract the equidistant sampling points.

The CHS arc lengths can be calculated from the following equation:

$$s = \int_0^1 g(t)\,\mathrm{d}t = \int_0^1 \sqrt{x'(t)^2 + y'(t)^2 + z'(t)^2}\,\mathrm{d}t = \int_0^1 \sqrt{\boldsymbol{t'}^{\mathrm{T}}\boldsymbol{H}^{\mathrm{T}}\boldsymbol{P}^{\mathrm{T}}\boldsymbol{P}\boldsymbol{H}\boldsymbol{t'}}\,\mathrm{d}t \tag{9}$$

(9) is an elliptic integral, which is difficult to calculate by ordinary methods. In this study, the Gauss-Kronrod quadrature method [33] is used to simplify the integration calculation process.

We use the G7-K15 method, a 7-point Gauss rule with a 15-point Kronrod rule, apply it to (9), and use the rules of the upper and lower limits of the integral transformation to calculate the arc length from t_0 to t_1:

$$\int_{t_0}^{t_1} g(x)\,\mathrm{d}x = \int_{-1}^{1} \frac{t_1 - t_0}{2} g\left(\frac{x+1}{2}(t_1 - t_0) + t_0\right)\mathrm{d}x \approx \sum_{i=1}^{15} w_i \frac{t_1 - t_0}{2} g\left(\frac{x_i + 1}{2}(t_1 - t_0) + t_0\right) \tag{10}$$

(10) can be used to calculate the arc length of the lane curve, which is not only used for equidistant sampling but also in intersection steering scenarios. The arc length can also be used to calculate curvature, which is convenient for planning.

5. LOCALIZATION BASED ON AN HD MAP

There are a variety of complex road environments in the cities, such as tunnels, overpasses, and urban canyons. These environments make GNSS-based localization less reliable. Some odometry fusing methods have emerged to solve the problem of GNSS failure. However, due to odometry drift, these methods cannot meet the localization requirements in scenarios where there is a long-term lack of effective global position information [34]. Although point cloud map relocalization based on the iterative closest point (ICP) [35], normal distribution transform (NDT) [36] and other methods is very effective, a very large point cloud map becomes a major challenge that affects practical use. An HD map contains various semantic features, while lane lines and traffic signs have good recognition both day and night. To explore the global localization method combining an HD map and IMU, two problems need to be solved. First, the elements in the HD map are associated with the elements detected using other sensors. Second, the pose is estimated based on the feature association results.

5.1. Reprojection

Reprojection refers to projecting the coordinates of a corresponding point in 3D space back to the pixel plane according to the currently estimated pose. The error between the reprojected and actual pixel coordinates is called the reprojection error and is often used as an indicator to evaluate the pose. Based on the position of the lane in the map, the known a priori knowledge of the HD map is projected onto the camera image by combining the intrinsic and extrinsic parameters of the camera. The evaluation of a pose metric is obtained by differencing the a priori map element positions and the coordinates of the matching perceptual results. Ideally, the distance between the two should be zero. The optimal camera pose can be obtained by optimizing the camera pose using a nonlinear optimization method to minimize this evaluation metric so that the optimal vehicle pose can be calculated.

First, referring to the transcendental vehicle pose $\boldsymbol{T}_{\mathrm{bw}}$, combined with (3), the representation of a feature point

$\boldsymbol{P}_{\mathrm{w}}$ in the world coordinate system at the coordinates $\boldsymbol{P}_{\mathrm{uv}}$ in the pixel plane system can be obtained.

$$\boldsymbol{p}_{uv} = h(\boldsymbol{T}_{\mathrm{bw}}, \boldsymbol{p}_{\mathrm{w}}) = \frac{1}{Z_c}\boldsymbol{K}\boldsymbol{T}_{\mathrm{cb}}\boldsymbol{T}_{\mathrm{bw}}\boldsymbol{p}_{\mathrm{w}} \tag{11}$$

where $\boldsymbol{T}_{\mathrm{cb}}$ is the transformation matrix from the vehicle coordinate system to the camera coordinate system, $\boldsymbol{T}_{\mathrm{bw}}$ is the transformation matrix from the world coordinate system to the vehicle coordinate system, and Z_c is the z axis coordinate of the feature point in the camera coordinate system, K is the camera internal parameter matrix. According to (11), the elements in the HD map are projected into the pixel plane.

5.2. Feature association

To use an HD map for localization, the location of objects detected by the sensors on the HD map needs to be known. This step is called feature association. Feature association locates HD map elements that match the features detected in the camera images. The correct selection of map features can significantly improve the localization results. In this study, we choose lane line elements as map features. This is because lane line features are easy to detect, have a long duration, and have good reflection properties, and have a high detection success rate in environments such as nighttime. The map elements are reprojected to the pixel plane (map features), and the distance between the detected elements (perceptual features) is calculated and used to evaluate the localization results.

Define the perceptual feature x as consisting of kind x^l and shape x^b, i.e. $x = \{x^l, x^b\}$. For lane line perception feature x, the slope difference of lanes on the same road section is very small. There is a possibility that distant lanes may be included in the HD map reprojection process by mistake. To better distinguish lane lines on the same road section, the shape is defined to consist of a sequence of lane line points x^s and their slopes x^d: $x^b = \{x^s, x^d\}$.

Based on the consistency of the local structure, the map feature reprojection error is calculated. Then, coarse matching of features and HD map perceptual features is performed. If the reprojection error is too large, the gap between the map and perceptual features is considered too large and will not be matched and optimized. The algorithm continues only when the error is less than a certain threshold. Define the map feature as y and given camera perceptual feature x, consider the confidence x^c that a feature belongs to a certain class with probability $P(x^l|y^l)$ given by the target detection module. Assuming that the shape detection noise obeys a normal distribution, this is combined with computing the feature's likelihood probability $P(x|y)$.

$$P(x|y) = P(x^l|y^l)P(x^c|y^l, x^l)P(x^b|y^b) \tag{12}$$

For the lane lines, define the likelihood probability $P(x^b|y^b)$ of the shape.

$$P(x^b|y^b) = \omega e^{-\frac{1}{2}\left(\frac{x_i^d - y_i^d}{\sigma_d}\right)^2} + (1-\omega)e^{-\frac{1}{2}\left(\frac{\bar{x}^p - \bar{y}^p}{\sigma_p}\right)^2} \tag{13}$$

where y^d and x^d are the slopes of the lane lines in the map feature and the perceptual feature, respectively, and $\bar{x}^p$ and $\bar{y}^p$ are the average coordinates of the sampling points of the lane lines on the x-axis in the map feature and the perceptual feature, respectively. σ_d is the variance of the lane slope. If the likelihood probability $P(x|y)$ is greater than a certain threshold Th, this map feature and the perceptual feature are considered as a pair of coarse matches $z_{ij} = \{x_i, y_j\}$ for the same feature.

Considering the map structure consistency, the perceptual feature structure should be similar to the map feature structure. After coarse matching, the distance between two of each map feature and the distance between two of the matching perceptual features is calculated, as shown in Figure 4. These two sets of distances are

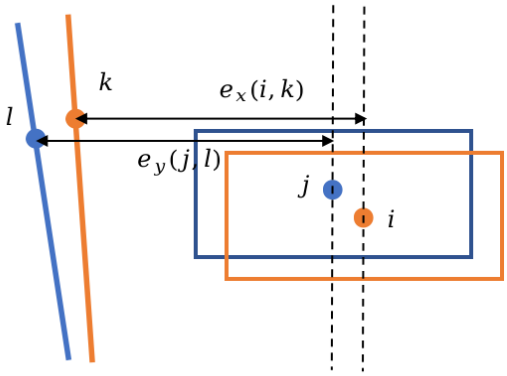

Figure 4. Edge similarity definition

called the structural features of the map features and the structural features of the perceptual features. The difference in the structural features is used as a measure to assess the similarity between a given frame's perceptual feature structure and the map feature structure.

Define the matching matrix $\boldsymbol{D} \in \mathbb{R}^{N_n \times N_m}$, where the element $d_{ij} = 1$ indicates that the perceptual feature x_i matches the map feature y_j; otherwise, $d_{ij} = 0$. Define that in two feature pairs d_{ij} and d_{kl}, the edge $e_x(i,k)$ denotes the horizontal distance between perceptual features x_i and x_k, and similarly, the edge $e_y(j,l)$ denotes the horizontal distance between map features y_j and y_l. Then, the similarity between the perceptual feature structure and map feature structure s_t in a certain frame is shown in (14).

$$s = \frac{1}{N_e} \sum_{i=1}^{N_n} \sum_{j=1}^{N_m} \sum_{k=1}^{N_n} \sum_{l=1}^{N_m} d_{ij} d_{kl} \exp\left(\left(\frac{e_y(j,l) - e_x(i,k)}{2\sigma_e} \right)^2 \right) \tag{14}$$

where N_n and N_m are the total numbers of perceptual features and map features after reprojection, respectively. $d_{ij}d_{kl}$ denotes the requirement that this edge exists for both map features and perceptual features. N_e is the number of all possible edges that satisfy the above requirement.

Considering the number of matches, structural consistency, and reprojection error, the feature matching problem can be expressed as a multi-order map matching problem.

$$\hat{\boldsymbol{D}} = \arg\max_{\boldsymbol{D}} \ \omega_1 N_d + \omega_2 s + \omega_3 \frac{1}{N_d} \sum_{i=1}^{N_n} \sum_{j=1}^{N_m} d_{ij} P(x_i | y_j) \tag{15}$$

where N_d is the number of feature matching pairs. $P(x_i|y_j)$ and s can be calculated by (12) and (15). ω_1, ω_2, ω_3 are the weight parameters.

5.3. Factor graph optimization

Define known sensor measurements $Z = \{z_i\}_{i=1}^{N_z}$, map feature measurements $Y = \{y_j\}_{j=1}^{N_m}$, where $l_j \in \mathbb{R}^3$, and pose estimates $X = \{x_t\}_{t=1}^{N_x}$, where $x_t \in SE(2)$. The HD map-based localization can be expressed as a maximum a posteriori probability (MAP) estimation as follows:

$$\hat{X} = \arg\max_{X} P(X|Z,Y) \tag{16}$$

This MAP estimation can be decomposed into two subproblems, feature association and pose estimation, to

create a feature association $D = \{d_t\}_{t=1}^{N_d}$ between the perceptual measurements and map feature measurements. It is obtained as follows:

$$\hat{X}, \hat{D} = \arg\max_{X,D} P(X, D|Z, Y) = \arg\max_{X,D} P(X|D, Z, Y)P(D|X, Z, Y) \tag{17}$$

We use factor graphs to optimally fuse odometry z^o and map feature measurements z^l from feature matching. It is more difficult to solve the posterior distribution directly, and with the matching relationship $\hat{D}$ already estimated, using Bayes' theorem, (17) can be written as

$$\hat{X} = \arg\max_{X} P(X|Z, Y, \hat{D}) = \arg\max_{X} P(X)P(Z|X, Y, \hat{D}) \tag{18}$$

The above equation splits the MAP estimation into the product of the maximum likelihood estimate (MLE) and the prior. Therefore, (17) can be equated to an MLE problem. Therefore, the pose X optimization problem can be constructed based on the odometry z^o and the feature matching pair (called landmarks) z^l obtained in the previous section. The error term consists of the odometry error e^o and the observation error e^y. The observation error e^y can be composed of the coordinate error e^l of the landmark and the map error e_j^m. Therefore, we divide the error term into three parts: odometry error e^o, landmark error e^l and map error e_j^m.

Assume that the noise satisfies a normal distribution. The odometry error optimization term can be defined as:

$$\sum_k e^o(x_{k-1}, x_k, z_k^o)^{\mathrm{T}} \Omega_k^o e^o(x_{k-1}, x_k, z_k^o) \tag{19}$$

where Ω_k^o is the information matrix, and the odometry error $e^o(x_{k-1}^p, x_k^p, z_k^o)$ can be expressed as the difference between the current pose $x_k^{p\mathrm{T}}$ after performing the transformation z_k^o on the pose x_{k-1}^p for the previous frame:

$$e^o(x_{k-1}^p, x_k^p, z_k^o) = x_k^{p\mathrm{T}} x_{k-1}^p z_k^o \tag{20}$$

The landmark error optimization term can be defined as:

$$\sum_k e^l(x_k^p, x^l, z_k^l)^T \Omega_k^l e^l(x_k^p, x^l, z_k^l) \tag{21}$$

where the landmark error can be represented by the difference between the x-axis coordinates of the perceptual features and map features:

$$e^l(x_k^p, x^l, z_k^l)^{\mathrm{T}} = \left[\frac{1}{Z_k^c} \boldsymbol{K} \boldsymbol{T}_{\mathrm{cb}} x_k^{p\mathrm{T}} x^l - z_k^l \right]_0 \tag{22}$$

The map error optimization term can be described as[37]:

$$\sum_k e_k^m(x^l)^{\mathrm{T}} \Omega_k^m e_k^m(x^l) = \frac{\gamma(c)}{r^2} \sum_k (x^l - m_k)^{\mathrm{T}} (x^l - m_k) \tag{23}$$

where $\gamma(c)$ is the inverse-chi-squared distribution function, r is the radius, and m_k is the location of the kth frame map feature.

When the error of a particular edge is significant, the growth rate of the Mahalanobis distance in the above equation is substantial. Therefore, the algorithm will try to preferentially adjust the estimates associated with this edge and ignore the effect of other advantages. This study uses the Huber kernel function $H(x)$ to adjust the error term and reduce the impact of erroneous data.

Combining (19), (21), and (23), the pose optimization function is obtained as follows:

$$\begin{aligned}\hat{X} = \arg\min_{X} &\sum_{k} H\left(e^{o}(x_{k-1}^{p}, x_{k}^{p}, z_{k}^{o})^{\mathrm{T}}\Omega_{k}^{o}e^{o}(x_{k}^{p}, x_{k}^{p}, z_{k}^{o})\right) \\ &+\sum_{k} H\left(e^{l}(x_{k}^{p}, x^{l}, z_{k}^{l})^{\mathrm{T}}\Omega_{k}^{l}e^{l}(x_{k}^{p}, x^{l}, z_{k}^{l})\right) \\ &+\frac{\gamma(c)}{r^{2}}\sum_{k}(x^{l}-m_{k})^{\mathrm{T}}(x^{l}-m_{k})\end{aligned} \tag{24}$$

6. EXPERIMENTS AND RESULTS

We validated the proposed localization algorithm through a series of experiments. First, the KITTI dataset is gradually simplified to fit a single parametric curve based on various lane characteristics. The curve equation of each lane line is calculated based on the three-time Hermite spline curve fitting algorithm proposed in this paper. Then, after intersection complementation and manual adjustment of elements, an HD map corresponding to the KITTI dataset is generated. Finally, based on the original odometry, the priori HD map information and the fused HD map localization algorithm proposed are used to further constrain the vehicle's lateral position.

6.1. Curve fitting

To fit the lane lines, we must extract the lane points. The first step uses the ground plane fitting (GPF) algorithm [30] to calculate the ground equation. The coordinates of the lane lines on the image in the camera coordinate system $\boldsymbol{P}_{\mathrm{c}}$ are calculated according to (5). Using the localization data of the GNSS/INS system as vehicle position true value $\boldsymbol{P}_{\mathrm{b}}$, the lane line recognition results of each frame are stitched and the same road section with different lane lines are stored as different categories. The StatisticalOutlierRemoval (SOR) filter [38] is used to filter some misdetected outliers. This step also excludes some poorly detected road sections together, which are reflected as different colors in different lane line maps, as shown in Figure 5(a).

The second step uses density-based spatial clustering of applications with noise (DBSCAN) [39] clustering to divide the closely spaced points (distance less than a certain threshold) into the same cluster. This search threshold needs to be slightly greater than the lane spacing and less than the distance between adjacent lanes at an intersection. This enables the clustering algorithm to search for adjacent lanes and ensure that the intersection area can be used for segmentation. Because of the large number of point clouds, the KD-Tree search algorithm is used rather than a traditional traversal search. Through DBSCAN clustering, the lane lines are divided into 19 areas, as shown in Figure 5(b).

In the third step, the lanes are divided via DBSCAN clustering using the information of different lanes in the same road recorded in the first step. Then the lanes are divided according to the category attribute for each segment, as shown in Figure 5(c). A unique ID is assigned to each lane here for subsequent lane completion.

The curve fitting process is shown in Figure 6, where the upper left, middle and right are X-Y, X-Z, and Y-Z views, respectively, which show that the fitting effect is relatively good. The spatial curve can describe the original lane line point set better.

The middle subplot of Figure 6 shows the fitting effect of parameter t, indicating the variation of the error of all parameters $\boldsymbol{t}_{\mathrm{i}}$ with the number of iterations. After four iterations, the error of most parameters $\boldsymbol{t}_{\mathrm{i}}$ decreases to below 1.0. The lower subplot shows the variation of the total error during the iterative calculation, and the error is stable after two iterations. The 3D view of this lane line fitting effect is shown in Figure 7.

This study determines the intersection connection based on the vehicle path to solve the problem that there

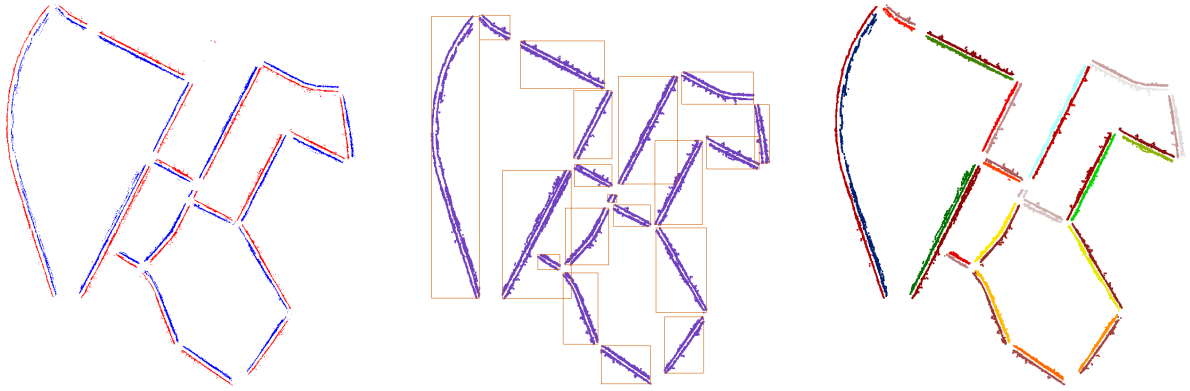

(a) Original lane data (b) Cluster division of lane (c) Cluster division with class

Figure 5. Extract lane points.

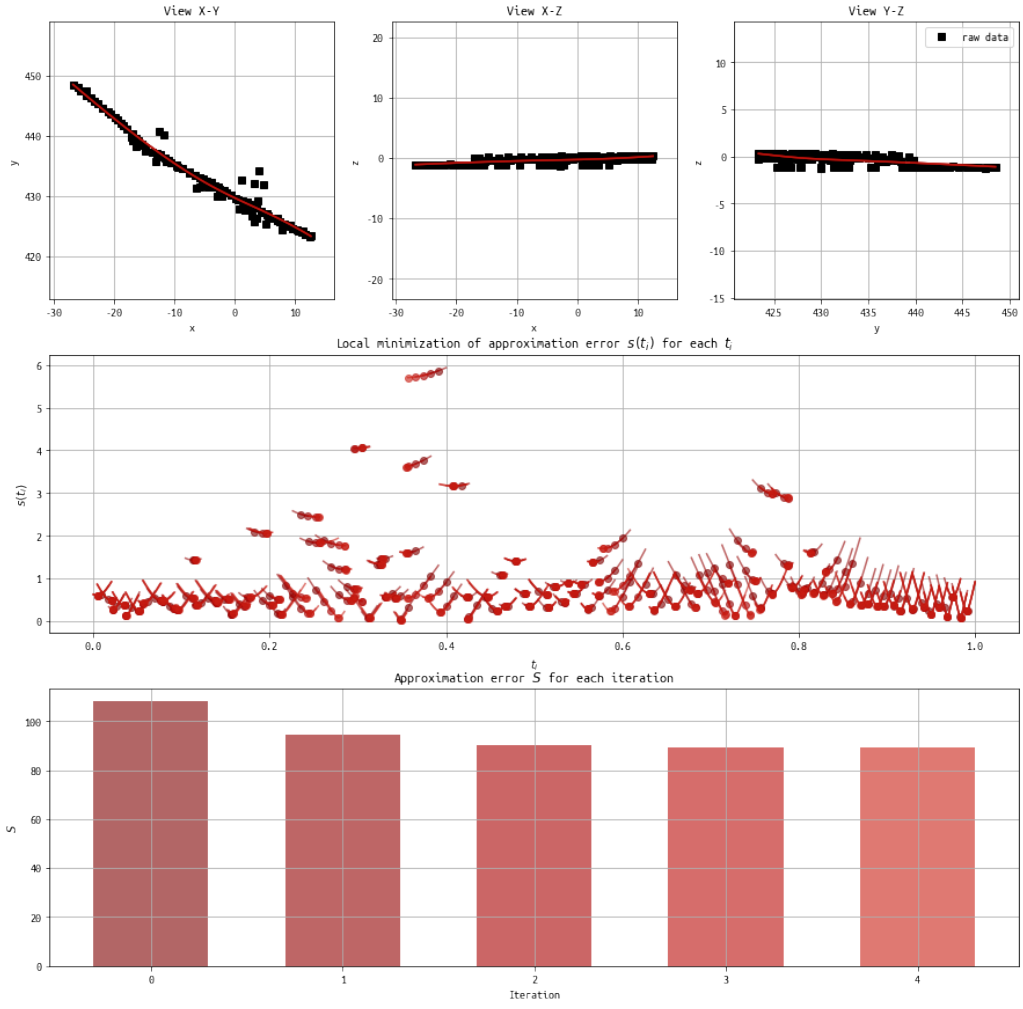

Figure 6. Curve fitting process.

may be no left turn or right turn on the road. The intersection topology is selected by combining the IDs assigned to each lane. The algorithm completes the virtual lane lines of the intersection.

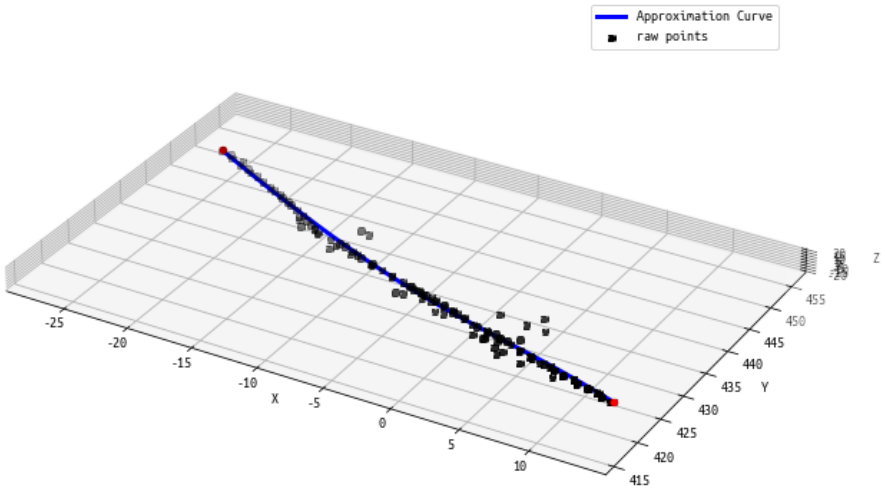

Figure 7. Single lane fitting result.

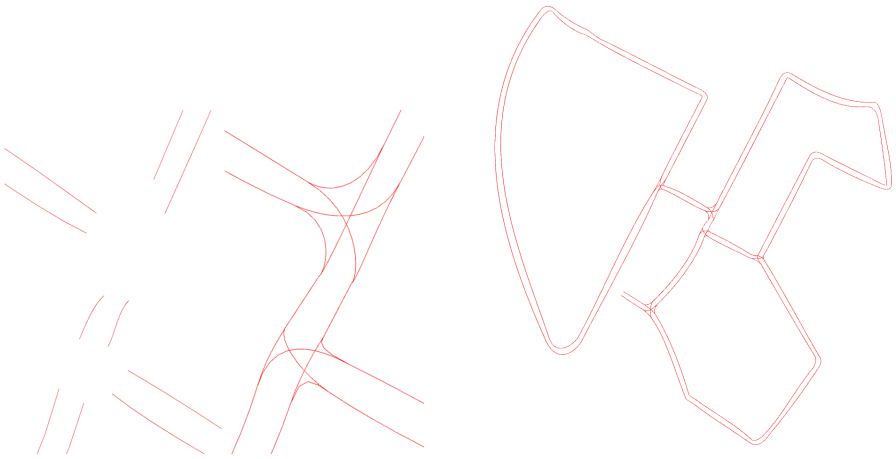

(a) Crossing fitting before and after comparison (b) Global lane fitting result

Figure 8. Lane Fitting Process

The results before and after intersection completion are shown in Figure 8(a). The final lanes for the entire area are shown in Figure 8(b), and the overall lane fit is relatively good. To create an HD map, further manual adjustment of the lane curve is also required, and complements other elements on the map, such as sidewalks and various traffic signs.

6.2. HD map production

The vehicle's starting point is defined as the map origin, and the GPS coordinates of the origin (48.982 545 °W, 8.390 366 °E) are recorded. To obtain higher projection accuracy, the European ETRS89 coordinates are used in this study. The coordinate system parameters are shown in Table 1.

We import the long-axis flattening of the Earth ellipsoid defined by the ETRS coordinate system in Table 1 into the Geographiclib geographic coordinate library for calculation. The coordinates of the initial point in the MGRS geographic coordinate system are 32UMV-55394.36-25694.44, of which the area number is 32UMV, the distance to the east is 55394.36 m, the distance to the north is 25 694.44 m, and the grid north angle is −0.5°.

Table 1. ETRS89 coordinate System

Name	Value
EPSG number	EPSG:25832
Prime meridian	Greenwich
Earth's ellipsoid	GRS 1980 (long axis: 6,378,137 m, flat rate: 298.257,222)

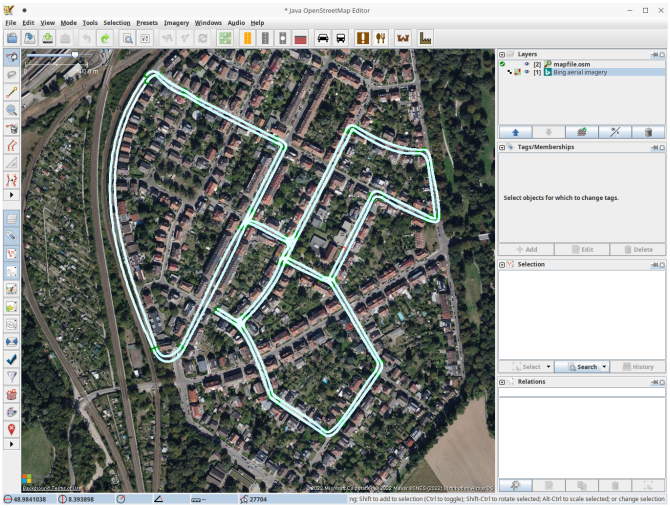

Figure 9. The lanelet2 map.

The MGRS coordinates of the lane lines and initial points shown in Figure 8(b) are stored in the Lanelet2 file. After opening the Lanelet2 file with the JOSM professional map software, the Mapbox satellite map is loaded as the base map. As shown in Figure 9, the converted coordinates can be recognized and displayed correctly by the professional mapping software. The road shapes overlap with the roads in the satellite map.

Figure 8(b) shows that some intersections are poorly fitted. The elements, such as stop lines and crosswalks, are not identified. Therefore, some elements that were missed by mistake were manually adjusted, the lane shape was fine-tuned, and pedestrian crossing markings and some traffic signs were added. Figure 10 shows the effect of manual labeling of some intersections. After adjusting the lane lines, a new curve equation needs to be refitted for this lane using the method in Part IV. Finally, the lane curve is optimized using a numerical integration method to approximate the arc-length isometric sampling.

6.3. Localization experiment

Following the previous preparations, the next step is to conduct a localization experiment. The points of the HD map are projected in the image coordinate system using formula (11). Considering the actual lanes in the camera image orientation, only the lanes located in the lower half of the image are kept, as shown in Figure 11. Since the virtual lane (blue) in the figure should not be involved in matching and optimizing the position attitude, only the actual lane (red) is reserved for lane matching and position optimization. The horizontal red lanes on both sides result from the projection of the nearby road, not the current road. The algorithm filters the possible lanes by radius and then projects them into the image. The final lanes involved in matching are shown in Figure 12.

Because the inertial guidance odometry in the KITTI dataset is relatively accurate, it does not reflect the effect of the localization algorithm well. In this paper, we use the LOAM [22] algorithm as a laser odometry and match the HD map with the actual detection results using the method proposed in Part V. The obtained matching results are added to the Georgia Tech Smoothing and Mapping (GTSAM) [40] optimization as roadmap con-

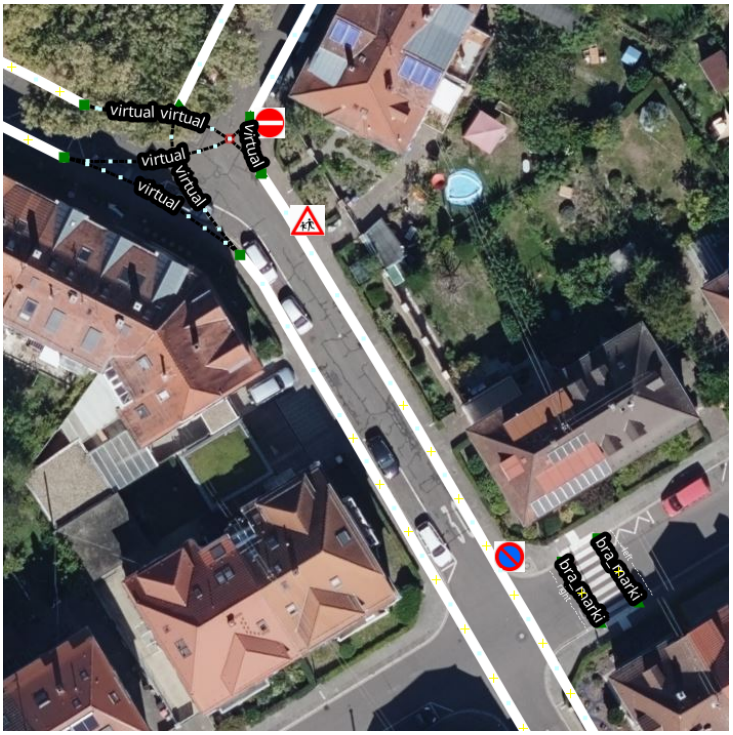

Figure 10. Manual marking.

Figure 11. The reprojection of HD map.

Figure 12. Available lanes for matching and optimizationp.

straints. To test the effect of fused localization, the fused HD map localization algorithm designed in this study is compared with the comparison of the actual value, as shown in Figure 13.

The metric commonly used in academia to evaluate trajectories is the root-mean-square deviation (RMSE):

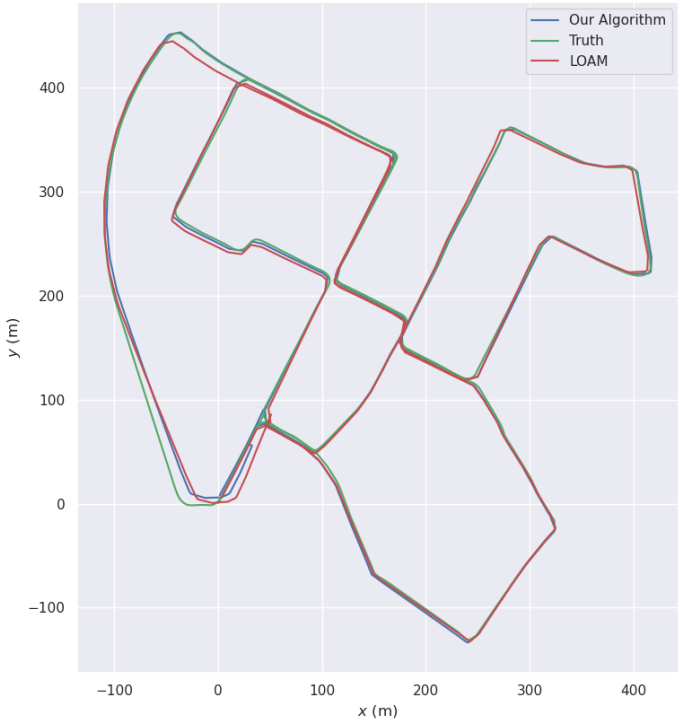

Figure 13. Comparison between our algorithm, LOAM and the ground truth.

Table 2. Localization error

Algorithm	RMSE	Min APE error	Max APE error
Algorithm of this paper	4.3361m	0.6679m	15.1492m
LOAM	12.5518m	1.1545m	21.8804m

$$\mathrm{RMSE} = \sqrt{\frac{1}{N}\sum_{i=1}^{N}\mathrm{APE}^2} \tag{25}$$

The absolute pose error (APE) considers only translational errors:

$$\mathrm{APE} = \left\|\mathrm{trans}(\boldsymbol{T}_{gt,i}^{-1}\boldsymbol{T}_{est,i})\right\| \tag{26}$$

In this study, the EVO [41] toolkit is used to evaluate the trajectory error of the proposed localization algorithm, and the results are shown in Table 2.

Figure 13 shows the comparison of the effect of the proposed algorithm and the LOAM algorithm. The proposed localization algorithm has a more significant improvement compared to the pure LOAM distance meter. As seen, the error in the localization effect of incorporating the HD map remains small most of the time. A horizontal offset can be seen in the upper left part of the road where the HD map does not exist. Because the leftmost road is long and has a particular curvature, the localization of the fused HD map needs to be improved for the forward direction. The LiDAR odometer has a large offset on the lower left side of the road,

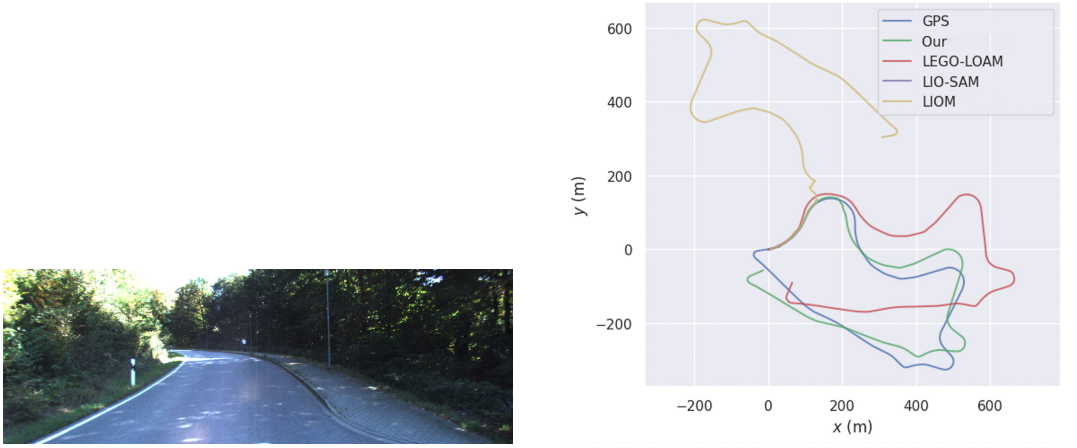

(a) Experimental scenes (b) Localization results

Figure 14. Robustness test.

so the algorithm developed in this study also has a large offset. This problem can be solved by subsequently considering adding more road elements.

6.4. Robustness test

Now, we compare the localization performance of the method in this paper with other methods. Since the road in the experimental scenes is lined with trees, the features extracted by LiDAR from the dense foliage are very noisy. In the experimental scenes, the GPS localization is correct because the GPS signal completely covers the experimental data set. We treat the GPS measurements here as ground truth. Figure 14(b) shows the localization results of the method in this paper with other methods in this case. LIOM lacks a pre-processing method to filter out reliable features, so its results are far from the correct ones. The unsatisfactory LIO-SAM results are due to unreliable features that severely affect the matching between keyframes. The method in this paper can obtain more accurate results than other methods.

7. CONCLUSION

In this paper, an iterative approximation-based method is proposed to generate the 3D curves of lane lines. For the problem of uneven sampling points in HD maps, a method based on numerical integration is proposed to achieve uniform sampling over the arc length. Based on the feature association results of the HD map and the perceptual image, lateral constraints are applied to the odometer localization results to obtain accurate and low-cost localization results. Experimental results show that the proposed method can generate HD maps and achieve high-precision localization. Future work will try to consider the lateral serial numbers of lane lines for clustering. Larger thresholds are easier to cluster on lane points with the same serial number. The radius threshold of lane points with different serial numbers is reduced so that the clustering can be clustered along the direction of lane lines, which can solve the problem of intermittent lane lines. To improve the practicality of this method, we will continue to explore the detection of more road elements, the generation of topological relationships for complex road sections (e.g., traffic circles), and the automatic association methods of traffic signs and lanes in the future. The main sensors used in this system are LiDAR and camera, which are sensitive to rain and snow occlusion. Therefore, the present system is not robust in rain and snow environment. In the subsequent work, thanks to the graphical optimization framework, we can easily add GPS measurement constraints to the position map. This can overcome the effect of rain and snow environment on the system to some extent. Cloudy weather is still one of the important challenges for GPS localization systems. In future

work, we will add kinematic model constraints to improve GPS localization results.

DECLARATIONS

Authors' contributions

Writing-Original Draft and conceptualization: Huang Z
Technical Support: Chen S
Validation and supervision: Xi X, Li Y
Investigation: Li Y, Wu S

Availability of data and materials

Not applicable.

Financial support and sponsorship

This work was supported by the Open fund of State Key Laboratory of Acoustics under Grant SKLA202215.

Conflicts of interest

All authors declared that there are no conflicts of interest

Ethical approval and consent to participate

Not applicable

Consent for publication

Not applicable

REFERENCES

1. Jeong J, Cho Y, Shin YS, Roh H, Kim A. Complex urban dataset with multi-level sensors from highly diverse urban environments. *Int J Robot Res* 2019;38:642-57. DOI
2. Azimi SM, Fischer P, Körner M, Reinartz P. Aerial LaneNet: lane-marking semantic segmentation in aerial imagery using wavelet-enhanced cost-sensitive symmetric fully convolutional neural networks. *IEEE Trans Geosci Remote Sensing* 2019;57:2920-38. DOI
3. Fischer P, Azimi SM, Roschlaub R, Krauß T. Towards HD maps from aerial imagery: robust lane marking segmentation using country-scale imagery. *IJGI* 2018;7:458. DOI
4. Cheng W, Yang S, Zhou M, et al. Road Mapping and Localization Using Sparse Semantic Visual Features. *IEEE Robot Autom Lett* 2021;6:8118-25. DOI
5. Qin T, Zheng Y, Chen T, Chen Y, Su Q. RoadMap: A light-weight semantic map for visual localization towards autonomous driving. arXiv:210602527 [cs] 2021 Jun. Available from: http://arxiv.org/abs/2106.02527. [Last accessed on 29 Jan 2023]
6. Hosseinyalamdary S, Peter M. LANE LEVEL LOCALIZATION; USING IMAGES AND HD MAPS TO MITIGATE THE LATERAL ERROR. *Int Arch Photogramm Remote Sens Spatial Inf Sci* 2017;XLII-1/W1:129-34. DOI
7. Matthaei R, Bagschik G, Maurer M. Map-relative localization in lane-level maps for ADAS and autonomous driving. In: 2014 IEEE Intelligent Vehicles Symposium Proceedings. MI, USA: IEEE; 2014. pp. 49–55. Available from: http://ieeexplore.ieee.org/document/6856428/. [Last accessed on 29 Jan 2023]
8. Nedevschi S, Popescu V, Danescu R, Marita T, Oniga F. Accurate Ego-Vehicle Global Localization at Intersections Through Alignment of Visual Data With Digital Map. *IEEE Trans Intell Transport Syst* 2013;14:673-87. DOI
9. Qu X, Soheilian B, Paparoditis N. Vehicle localization using mono-camera and geo-referenced traffic signs. In: 2015 IEEE Intelligent Vehicles Symposium (IV); 2015. pp. 605–10. DOI
10. Tao Z, Bonnifait P, Frémont V, Ibañez-Guzman J. Mapping and localization using GPS, lane markings and proprioceptive sensors. In: 2013 IEEE/RSJ International Conference on Intelligent Robots and Systems; 2013. pp. 406–12. DOI
11. Welzel A, Reisdorf P, Wanielik G. Improving urban vehicle localization with traffic sign recognition. In: 2015 IEEE 18th International Conference on Intelligent Transportation Systems; 2015. p. 5. DOI
12. Xiao Z, Yang D, Wen T, Jiang K, Yan R. Monocular Localization with Vector HD Map (MLVHM): A Low-Cost Method for Commercial IVs. *Sensors (Basel)* 2020;20:1870. DOI

13. Jo K, Lee M, Kim C, Sunwoo M. Construction process of a three-dimensional roadway geometry map for autonomous driving. *Proceedings of the Institution of Mechanical Engineers, Part D: Journal of Automobile Engineering* 2017;231:1414-34. DOI
14. Chen A, Ramanandan A, Farrell JA. High-precision lane-Level road map building for vehicle navigation. In: IEEE/ION Position, Location and Navigation Symposium; 2010. pp. 1035–42. DOI
15. Jo K, Sunwoo M. Generation of a precise roadway map for autonomous cars. *IEEE Trans Intell Transport Syst* 2014;15:925-37. DOI
16. Zhang T, Arrigoni S, Garozzo M, Yang Dg, Cheli F. A lane-level road network model with global continuity. *Transportation Research Part C: Emerging Technologies* 2016;71:32-50. DOI
17. Gwon GP, Hur WS, Kim SW, Seo SW. Generation of a precise and efficient lane-level road map for intelligent vehicle systems. *IEEE Trans Veh Technol* 2017;66:4517-33. DOI
18. Godoy J, Artuñedo A, Villagra J. Self-Generated OSM-Based Driving Corridors. *IEEE Access* 2019;7:20113-25. DOI
19. Jiang K, Yang D, Liu C, Zhang T, Xiao Z. A flexible multi-layer map model designed for lane-level route planning in autonomous vehicles. *Engineering* 2019;5:305-18. DOI
20. Poggenhans F, Pauls JH, Janosovits J, et al. Lanelet2: a high-definition map framework for the future of automated driving. In: 2018 21st International Conference on Intelligent Transportation Systems (ITSC). Maui, HI: IEEE; 2018. pp. 1672–79. Available from: https://ieeexplore.ieee.org/document/8569929/. [Last accessed on 29 Jan 2023]
21. Marais J, Ambellouis S, Flancquart A, et al. Accurate localisation based on GNSS and propagation knowledge for safe applications in guided transport. *Procedia - Social and Behavioral Sciences* 2012;48:796-805. DOI
22. Zhang J, Singh S. LOAM: Lidar odometry and mapping in real-time. In: Robotics: Science and Systems. vol. 2. Berkeley, CA; 2014. pp. 1–9.
23. Shan T, Englot B. Lego-loam: Lightweight and ground-optimized lidar odometry and mapping on variable terrain. In: 2018 IEEE/RSJ International Conference on Intelligent Robots and Systems (IROS). IEEE; 2018. pp. 4758–65. DOI
24. Qin C, Ye H, Pranata CE, et al. LINS: a lidar-inertial state estimator for robust and efficient navigation. In: 2020 IEEE International Conference on Robotics and Automation (ICRA). IEEE; 2020. pp. 8899–906. DOI
25. Shan T, Englot B, Meyers D, et al. Lio-sam: Tightly-coupled lidar inertial odometry via smoothing and mapping. In: 2020 IEEE/RSJ International Conference on Intelligent Robots and Systems (IROS). IEEE; 2020. pp. 5135–42. DOI
26. Campos C, Elvira R, Rodríguez JJG, M Montiel JM, D Tardós J. ORB-SLAM3: an accurate open-source library for visual, visual–inertial, and multimap SLAM. *IEEE Trans Robot* 2021;37:1874-90 DOI
27. Qin T, Li P, Shen S. Vins-mono: A robust and versatile monocular visual-inertial state estimator. *IEEE Trans Robot* 2018;34:1004-20. DOI
28. Qin T, Shen S. Online temporal calibration for monocular visual-inertial systems. In: 2018 IEEE/RSJ International Conference on Intelligent Robots and Systems (IROS). IEEE; 2018. pp. 3662–69. DOI
29. Geiger A, Lenz P, Stiller C, Urtasun R. Vision meets robotics: the KITTI dataset. *Int J Robot Res* 2013;32:1231–37. DOI
30. Zermas D, Izzat I, Papanikolopoulos N. Fast segmentation of 3D point clouds: a paradigm on LiDAR data for autonomous vehicle applications. In: 2017 IEEE International Conference on Robotics and Automation (ICRA). Singapore, Singapore: IEEE; 2017. pp. 5067–73. Available from: http://ieeexplore.ieee.org/document/7989591/. [Last accessed on 29 Jan 2023]
31. Byrd RH, Lu P, Nocedal J, Zhu C. A limited memory algorithm for bound constrained optimization. *SIAM J Sci Comput* 1995;16:1190-208. DOI
32. Fritsch FN, Carlson RE. Monotone piecewise cubic interpolation. *SIAM J Numer Anal* 1980;17:238-46. DOI
33. Kronrod AS. Nodes and weights of quadrature formulas. New York: Consultants Bureau 1965. DOI
34. Wang H, Xue C, Zhou Y, Wen F, Zhang H. Visual semantic localization based on HD map for autonomous vehicles in urban scenarios. In: 2021 IEEE International Conference on Robotics and Automation (ICRA). Xi'an, China: IEEE; 2021. pp. 11255–61. Available from: https://ieeexplore.ieee.org/document/9561459/. [Last accessed on 29 Jan 2023]
35. Besl PJ, McKay ND. Method for registration of 3-D shapes. In: Sensor fusion IV: control paradigms and data structures. vol. 1611. Spie; 1992. pp. 586–606. DOI
36. Biber P, Straßer W. The normal distributions transform: a new approach to laser scan matching. In: Proceedings 2003 IEEE/RSJ International Conference on Intelligent Robots and Systems (IROS 2003)(Cat. No. 03CH37453). vol. 3. IEEE; 2003. pp. 2743–48. DOI
37. Wilbers D, Merfels C, Stachniss C. Localization with sliding window factor graphs on third-Party maps for automated driving. In: 2019 International Conference on Robotics and Automation (ICRA). Montreal, QC, Canada: IEEE; 2019. pp. 5951–57. Available from: https://ieeexplore.ieee.org/document/8793971/. [Last accessed on 29 Jan 2023]
38. Rusu RB, Marton ZC, Blodow N, Dolha M, Beetz M. Towards 3D Point cloud based object maps for household environments. *Robot Auton Syst* 2008;56:927-41. DOI
39. Ester M, Kriegel HP, Sander J, Xu X. A density-Based algorithm for discovering clusters in large spatial databases with noise. In: Proceedings of the Second International Conference on Knowledge Discovery and Data Mining. KDD'96. AAAI Press; 1996. pp. 226–31. DOI
40. Dellaert F. Factor graphs and GTSAM: a hands-on introduction. Georgia Institute of Technology; 2012. DOI
41. Grupp M. Evo: Python package for the evaluation of odometry and SLAM.; 2017. Available from: https://github.com/MichaelGrupp/evo. [Last accessed on 29 Jan 2023]

Li *et al. Complex Eng Syst* 2023;3:1
DOI: 10.20517/ces.2022.46

Complex Engineering Systems

Review

Open Access

Review on key technologies of green power supply for port microgrid

Guangdi Li[1], Tong Wang[1], Bowen Zhou[1], Zhaoxia Xiao[2], Shijie Yan[1], Boyu Liu[3]

[1]College of Information Science and Engineering, Northeastern University, Shenyang 110819, Liaoning, China.
[2]College of Electrical Engineering, Tianjin Polytechnic University, Tianjin 300387, China.
[3]School of Electrical Engineering and Telecommunications, UNSW Sydney, NSW 2052, Australia.

Correspondence to: Dr. Guangdi Li, College of Information Science and Engineering, Northeastern University, NO. 3-11, Wenhua Road, Heping District Shenyang, Shenyang 110819, Liaoning, China. E-mail: liguangdi@ise.neu.edu.cn

How to cite this article: Li G, Wang T, Zhou B, Xiao Z, Yan S, Liu B. Review on key technologies of green power supply for port microgrid. *Complex Eng Syst* 2023;3:1. https://dx.doi.org/10.20517/ces.2022.46

Received: 11 Nov 2022 **First Decision:** 15 Dec 2022 **Revised:** 26 Dec 2022 **Accepted:** 1 Jan 2023 **Published:** 31 Jan 2023

Academic Editor: Hamid Reza Karimi **Copy Editor:** Fangling Lan **Production Editor:** Fangling Lan

Abstract

With the development of ship electrification, the demand for energy in ports is increasing. The location and natural resources of ports also create conditions for the development of ship electrification. This paper firstly analyzes the current development status of floating solar power generation technology and offshore wind power generation technology, summarizes the obstacles facing the development of offshore power generation platforms, introduces the materials and structures that can be used for floating power generation platforms, and then introduces the port microgrid topology from three aspects of AC microgrid (AC), DC microgrid (DC) and AC/DC hybrid microgrid (AC/DC) hybrid structure, and compares the three structures. Then the existing control methods are reviewed from the perspective of port capacity planning and the application of distributed control in port energy planning is emphasized. Finally, port energy management strategies are introduced from the perspective of multiple time scales, and relevant cases are listed, and the advantages and disadvantages of management strategies under different time scales are compared. At the end of the paper, several advanced smart ports are given as examples, and the new energy used by each port and its development scale are analyzed, and the future clean and efficient ports are envisioned.

Keywords: Floating power supply platform, ports, microgrid topology, capacity planning, energy management

1. INTRODUCTION

Maritime transport plays a key role in international communication. It is estimated that 90% of the world's trade in goods is carried out by sea. However, most ships use fossil fuels to meet their energy needs, resulting in the emission of pollutant gases, particulate matter, and greenhouse gases (GHG)[1]. The development of clean and renewable energy and large-scale use of port power and charging facilities are the main measures to achieve the port carbon reduction target. Considering the waiting ships outside the port, it is necessary to further extend the port.

In 2015, Norway launched its first fully electric ferry, adding to the growing number of fully electric ships. In such containers, electricity can be generated from renewable resources and storage systems, such as batteries and supercapacitors[2]. Singapore's Jurong Port has a 9.5 MWP solar power system that generates more than 12 million kWh a year and meets 60% of the power demand at the port. Hamburg Port[3] has implemented the overall plan of "Smart Port Energy". One of the sub-projects is the Altona Cruise terminal shore power project. Shore power facilities are connected to the 10 kV medium-high voltage main grid of Hamburg, and the power is transmitted to the terminal frequency converter station through cables, which can provide 12 MVA/6.6 KV/60 Hz or 12 MVA/11 KV/60 Hz power to cruise ships. Shore power facilities are powered by renewable energy, reducing CO_2 emissions by more than half. The microgrids of ports such as Bayonne Tarnos in France, Long Beach in the United States, and Mytilene in Greece also include photovoltaic (PV) power generation systems and wind turbines (WT), which use renewable energy to generate electricity, meet the power demand of critical loads in emergency situations and are used for cold ironing of cargo ships to reduce the emission of polluting gases.

At present, China's ports have only a small amount of renewable energy installed, and the research on the renewable energy network for shore power supply is still in the primary stage. "Ming Qing", the world's largest 400,000-ton super mine ship in Dongjiakou Port (Qingdao)in Shandong Province, China, has successfully connected to the dock shore electricity, marking that the China port is the first in the world to realize the full application of shore electricity for the 400,000-ton super mine ship. The Laotangshan Wharf at Zhoushan Port[4] has completed the first hybrid port power system of high and low voltage in Zhoushan City, with a total capacity of 4030 kVA, which can simultaneously meet the power supply demand of two bulk cargo ships of 150,000 tons and two bulk cargo ships of 50,000 tons. The terminal of Section C in the Beijiang port area of Tianjin Port has been put into operation, which is the first "smart zero-carbon" terminal in the world. The facilities and equipment are driven by electricity, and the "integration of scenery and storage and loading" system realizes the independent supply of green electricity, with zero carbon emission in the whole process. The berth of Nanjing Longtan Port adopts low-voltage shore power and builds 4 sets of 100kVA shore power connection devices, 4 sets of 200 kVA shore power connection devices, and 2 sets of 300 kVA shore power connection devices, with a total capacity of 1800 kVA. Shanghai Port, Guangzhou Port, Qingdao Port, and many other ports have carried out power projects to develop the green intelligent control system.

The literature on "cold-ironing[5]" and "shore power supply[6]"introduces that the onshore power grid supplies power to the berthed ship, avoiding the use of diesel generators on the ship. To reduce the carbon footprint of cold-ironing ships and avoid fossil fuel generation in the main grid, renewable energy, solar panels, wind turbines, and storage options have been increasingly considered[7]. Sadeghi *et al.* proposed the design and optimization of a hybrid renewable energy system (HRESs) with power-sharing capability, using multi-objective particle swarm optimization (MOPSO) and multi-objective Crow search (MOCS) to solve the problem studied so that the system has good economic benefits and reliability[8]. In order to manage these elements, more and more attention has been paid to the development of microgrids in port areas in

the last decade. While microgrids have been widely developed worldwide in different areas (cities, remote communities, islands, *etc.*), they are still rare in port areas. This is because of the diversity of port loads (refrigerated containers, quay cranes, ship cold-irons, buildings, *etc.*) and other reasons related to energy management, load forecasting difficulties, and megawatt power demand[9]. In addition, the development of microgrids involves huge investments due to the use of storage solutions and renewable energy sources, leading to problems of investment cost-sharing between authorities and port owners and the management of microgrids from both commercial and energy perspectives[10,11].

This paper summarizes and analyzes the research progress of green power supply technology in port microgrids, and its organizational structure is as follows. The first part introduces the current development status of port green power supply technology, and the second part introduces different power systems, describes photovoltaic power generation in detail, and lists some running cases. The third part introduces the DC microgrid, AC micro power grid, and the scenery storage integration of micro AC/DC hybrid power grid and compares three kinds of systems, and the fourth part introduces the port capacity of micro power grid planning and the existing methods. The fifth part introduces the distributed control method and multi-time scale energy management strategy of port microgrids, and the sixth part lists the existing cases in the world. The last section summarizes the findings and prospects the future research directions.

2. FLOATING WIND-PV-STORAGE POWER SUPPLY PLATFORM

2.1. Floating offshore wind power platform

Offshore wind farms are offshore wind power plants in water depths of about 10 meters, and electricity is generated by turning wind turbines. Compared with onshore wind farms, offshore wind farms have the advantages of not occupying land resources, basically unaffected by topography, higher wind speed, more abundant wind energy resources, larger wind turbine capacity (3-5 MW), and higher annual utilization hours. However, the construction of offshore wind farms is also technically difficult, and the construction cost is generally 2 to 3 times that of onshore wind farms.

In recent years, the UK, Germany, Denmark, the United States, Japan, and other western countries have accelerated the research of offshore wind speed. Chen *et al.* introduce the general situation of the early development of offshore wind in these countries, describe the main characteristics and trends in the development of offshore wind, enumerate the German electric field and the ocean buoyancy postures in typical cases such as wind turbine experiment[12]. Luo *et al.* review the offshore wind power grid general topology structure, offshore wind reliability evaluation methods and indexes, models of offshore wind power, collection systems in offshore wind farms, the reliability evaluation method of offshore wind power is proposed, the failure probability of different components in the offshore wind power grid and fault repair time for each component[13]. On this basis, the operational reliability improvement technology of offshore wind power is discussed from the aspects of the system and components. Ge *et al.* introduce key technologies of intelligent operation control and maintenance of offshore wind farms[14], including offshore wind power prediction technology, offshore wind power operation control technology, offshore wind power equipment maintenance and management technology, and the comprehensive utilization of offshore wind power and sea area. In addition, the differences between offshore wind power and onshore wind power are analyzed according to the factors of offshore weather environment, resource characteristics, geographical location, equipment operation, and so on. Based on this, the challenges and possible solutions in the above technology fields are summarized, and the research status and achievements of these technologies are analyzed and summarized. Li *et al.* present a flexible high-voltage large-capacity DC transformer topology[15], explored based on the active bridge arm and thyristor valve group, the diode valve combination way of the new converter. This combines the thyristor valve, diode group, and low conduction loss, high

power density, advantages of the series configuration, special characteristics of the voltage of the active bridge arm, and highly controllable current waveforms. Thus, with high-efficiency flexible commutation, highly controllable power conversion, and the input and output DC current smooth, there is no need to install a filter. Compared with the existing flexible DC power transmission modular multilevel converter offshore platform, the technical economy of the proposed DC transformer topology is illustrated.

Offshore wind power is the focus of renewable energy development in China at present and in the next few decades. However, compared with onshore wind power, offshore wind power faces challenges such as high life-cycle electricity cost and the large impact of large-scale grid connection, and digitalization and intelligence are the key to solving the above problems. The full DC offshore wind farm proposed by Li *et al.* is a cutting-edge technology supporting the large-scale and far-reaching development of offshore wind power[15], which is expected to improve the gathering and sending efficiency of wind power and reduce the volume of offshore platforms. The 100 kV/100 MW DC transformer is a technical bottleneck for the full DC offshore wind farm to be broken urgently. Research on key technologies of intelligent operation control and maintenance of offshore wind farms can provide support and reference for reducing cost and increasing efficiency of offshore wind power and large-scale safe and economic grid connection.

2.2. Floating photovoltaic power generation platform

In recent years, photovoltaic power generation technology has developed significantly. Considering issues such as land costs, transmission costs, and water competition between power generation and agricultural production, there is an increasing number of studies on floating PV. The offshore environment can make full use of sunlight and is an ideal location for building photovoltaic power plants. Using floating technology to install a solar photovoltaic system on the water is a new idea. A floating photovoltaic power station adopts photovoltaic power station technology and floating technology, which has great development potential.

Agrawal *et al.* evaluated the technical potential of floating solar photovoltaic power generation through simulation, and discussed the development of floating solar photovoltaic technology from the aspects of future photovoltaic potential, water saving and land-saving potential, and took Rajghat dam in southern Uttar Pradesh, India as an example to estimate its annual power generation and reduced water evaporation[16]. Trapani and Redón Santafé reviewed various floating PV projects realized between 2007 and 2013 and envisaged future projects installed on the ocean using a composite laminated film material, which will make the structure flexible and be able to adapt to the waves in the ocean and inundation of the submersible array in adverse weather conditions[17]. Oliveira-Pinto and Stokkermans noted that the experience from inland floating solar energy projects can be used to expand and migrate from inshore to offshore conditions, explore floating methods in the marine environment, and investigate photovoltaic technology and solar power for floating in marine conditions[18]. That paper also discussed the currently available technologies, challenges and risks of the design and construction of the projects in the marine environment. Floating in the sea is more flexible than a conventional rigid glass module, and thus Sahu *et al.* introduced several key elements and put forward a hexagon photovoltaic array, which enables the whole system to follow the movements of the waves, thus minimizing the waves caused damages[19]. At the same time, the effect of these parts and all kinds of design schemes are further described[19].

2.3. Photovoltaic power supply platform with energy storage

Wind speed is affected by weather, geography, and other factors, while its size and wind direction will change regularly, and photovoltaic output is also closely related to weather changes. The change in light intensity and temperature will affect the size of output, resulting in great randomness, volatility, and intermittence of wind power and photovoltaic output. Scenery installed capacity of the entire network

capacity is small, and scenery output fluctuations do not cause a negative influence on the power grid. However, as the scene is increasingly connected to the electricity grid capacity, the influence of randomness, volatility, and intermittent scenery output characteristics on the safety and stability of power system operation is more and more significant, greatly reducing the power quality. It considerably affects the grid connection of wind power generation and the frequency modulation and peak regulation of the power grid. The development of energy storage technology makes it possible to solve the output fluctuation of wind power generation.

Ning *et al*. introduced the basic principle of energy storage to smooth the output fluctuation of wind-power generation[20], expounded the research status of energy storage system control methods when wind-power generation fluctuation is smooth, and summarized the similarities and differences of various existing methods. Zhao and Cui introduced the photovoltaic system capacity ratio analysis optimization calculation using the leveling of the KWH cost concepts. The optimal energy storage system configuration and the project yield of this method were verified when compared with the optical storage system under different storage configurations and the existing load power and PV systems under the optimization calculation[21]. Gao *et al*. established eight kinds of wind-wind-load composite Copula models by combining the actual offshore wind farm power, photovoltaic power plant power and grid load, and proposed a hybrid time-varying Copula model based on rattan structure, which can more accurately describe the high-dimensional wind-wind-load dependence structure[22]. Sun *et al*. established the coordination relationship model between photovoltaic and energy storage systems[23], carried out the coordination optimization of energy storage devices under different output conditions of renewable energy, and proposed the voltage stability control method of regional power grid based on the coordination of distributed photovoltaic and energy storage. Recent studies in[24,25] proposed a method for different photovoltaic units and hybrid energy storage units to cooperatively suppress the bus voltage fluctuation and keep the load side voltage stable.

Although the floating power supply platform is predicted to have great development prospects, various limitations prevent the technology from being used commercially on a large scale. The near harbor is a complex environment that requires a consideration of the external environment such as geographical factors, climatic environment, solar emissivity, and so on, and requires the components to be able to withstand saltwater, strong ocean currents, waves, and wind. The current low maturity of the industry leads to a lack of direct reference standards for design in port environments. However, the industry can look to more established industries such as offshore oil and gas, or offshore renewable energy (MRE) such as offshore wind.

3. TOPOLOGICAL STRUCTURE DESIGN OF MICROGRID SYSTEM NEAR PORT

In the past decade, maritime transport has been responsible for nearly 90% of the world's overseas trade and logistics, accounting for 3% to 5% of total greenhouse gas emissions. This could rise to 18% by 2050, according to research by the International Maritime Organization (IMO). There is an urgent need for a more efficient maritime transport system, improving the efficiency of all the subsidiary energy subsystems. Today, seaport microgrids are seen as a viable way to improve overall system flexibility as well as mitigate growing environmental concerns. However, with the trend of electrification, the connection between port and ship is no longer limited to logistics but extended to power, which makes future maritime transport management a complex transport-power multi-microgrid coordination problem. Seaport microgrid is a representative and promising technology for shaping future green maritime transportation.

3.1. Harbor AC microgrid

The offshore wind power is connected to the onshore power grid. When charging, the ship is connected to shore power through AC/DC converter, and all the energy is transmitted to the ship through AC connection. The AC/DC converter, which charges the battery, is placed on the boat in a similar way to an on-board electric car charger. For small battery-powered fishing and recreational boats, shore-charging with a standard three-phase 400 V AC plug is the most common solution, which is also common in industrial environments. However, dedicated infrastructure should be built for passenger or car ferries that need more electricity to recharge the batteries on board. The power rating required for port infrastructure may vary depending on the number of ships calling at the port and the capacity of the batteries on board.

Karimi *et al.* described a charging system based on AC shore power[26]. Figure 1A shows a DC marine propulsion system based on AC shore power. In addition to the grid interface, there is a fixed battery storage system, which is usually slowly charged from the grid. Charging at night or off-peak hours not only reduces the strain on the local grid but also takes advantage of cheaper electricity. Transformer T12 is a 50 Hz transformer that reduces the grid voltage to the shore bus voltage and isolates the shore bus from the grid. The converter C15 acts as a charger and is responsible for rectifying the energy received from the shore. The C12 converter is directly connected to the onboard battery B11 to control the transfer of power during charge and discharge. Similarly, the converter C17 controls the energy of the onshore battery B12. In addition, the converter C16 acts as a rectifier when the onshore battery is charged and an inverter when the shipboard battery is charged. To reduce costs, some onboard propulsion systems have battery packs connected directly to the main bus, eliminating the need for a DC/DC converter. At this point, C15 controls the charging power. However, for multi-bus propulsion systems, each bus should have a dedicated charging converter, such as the C15, which controls the charging power balance of each onboard battery pack. Figure 1B shows the AC ship propulsion system based on AC shore power. The shore charging system is the same as that in (a), but it is connected to the AC propulsion system. An AC charging solution for an AC propulsion system requires synchronizing the voltage, phase, and frequency of the onboard power system to the onshore grid prior to connection. To avoid the synchronization process and to shorten the time, a dedicated active or passive rectifier, C27, can be used instead of a converter, C21. For the system in Figure 1B, a shipboard transformer can be added to provide current isolation or to adjust the voltage between the AC grid and the shore bus, but adding on-board transformers would result in higher costs and lower energy efficiency.

3.2. Harbor DC microgrid

At present, the mainstream ships use low-voltage AC power supply, and its shore power system also uses low-voltage AC systems. However, with the continuous enhancement of the functions of various types of ships and the increase of electrical equipment, medium pressure ships will become the main trend of ships in the future. The ship integrated power system represents the future development direction of the ship power system, and its power transmission and distribution subsystem adopts the medium voltage DC distribution network.

Compared to AC microgrids, DC grids have greater reliability and efficiency, simpler controls, and natural interfaces with renewable energy sources, as well as electronic load and energy storage systems. Dragicevic *et al.* studied typical power supply hardware topologies and their applicability to different emerging smart grid applications, and outlined the current state of development of DC MG protection and grounding technologies, but did not solve the problem of arc not being naturally extinguished due to DC current breakdown[27].

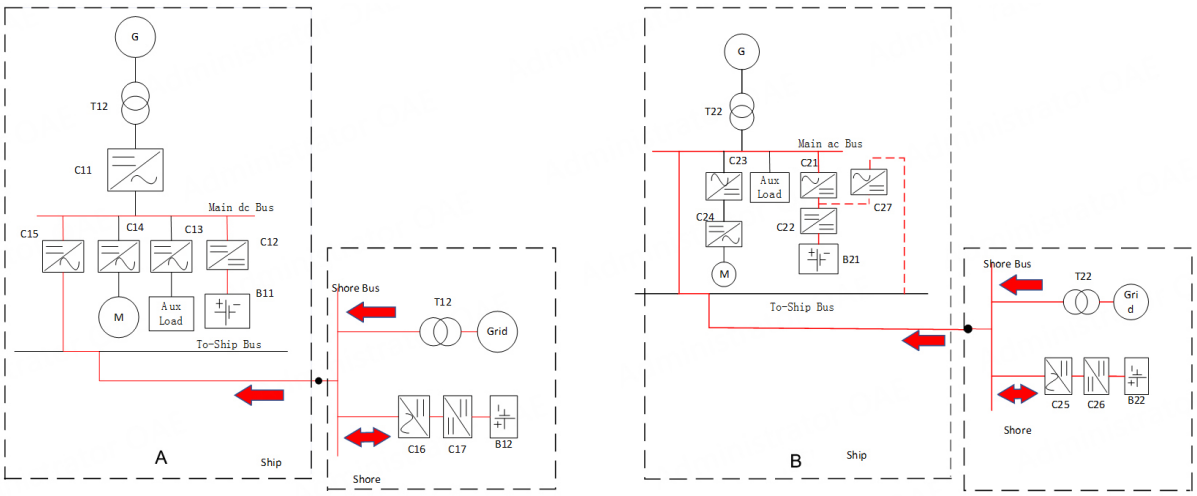

Figure 1. Marine propulsion system based on AC shore power.

Figure 2A depicts a DC marine propulsion system based on DC shore power. By comparing the power converters in Figures 1A and 2A, it is clear that the shipborne converter C15 has been replaced by the land-based C35. In this scheme, the charger converter (C32) can be removed, and the shipboard battery pack can be connected directly to the DC main bus. Onshore DC/DC converters can be installed at plugs to control charging power and reduce ship weight. Figure 2B depicts an AC marine propulsion system based on DC shore power. The ship bus is connected to the input end of the converter C42, so the charging path is the same as in Figure 2A

3.3. Harbor AC/DC hybrid microgrid

Hybrid AC-DC microgrids are a promising alternative to existing distribution systems to achieve near/net zero energy building goals. However, hybrid microgrid has increasingly high requirements for compact structure, seamless integration of distributed generators and load, and flexibility of control, which cannot be fully met by traditional grid architecture. Yu *et al.* proposed an integrated, reconfigurable AC-DC hybrid microgrid architecture and its layered control strategy with flexible control[28]. Yu *et al.* proposed a scalable and reconfigurable cluster architecture for hybrid microgrids and the corresponding decentralized control method[29].

Due to the gradual popularization of medium voltage direct current (MVDC) ships, namely the diversification of new energy sources in the port area, the future port is actually an AC/DC hybrid power system, as shown in Figure 3. Table 1 compares the advantages and disadvantages of the three microgrids.

4. CAPACITY PLANNING OF MICROGRID SYSTEM NEAR PORT

How to plan the capacity of photovoltaic and energy storage will directly affect the cost and benefit of grid-connected optical storage microgrid. Effectively solving this problem can greatly impact the promotion of new energy microgrids. However, capacity planning research based on limited historical data faces two major difficulties: firstly, photovoltaic power generation is uncertain, and it is difficult to accurately estimate its corresponding probability distribution; secondly, the photovoltaic power generation has high dimensionality, that is, the photovoltaic power generation situation of each day and time period in a longer dispatch period should be considered. Therefore, Xu *et al.* put forward the research idea of dimensionality reduction based on scene clustering analysis and then proposed an optimization method to deal with the uncertainty of photovoltaic power generation[30]. Wang *et al.* proposed a flexible DC grid capacity planning

Table 1. Comparison of microgrid structure

	DC	AC	AC/DC
Advantage	Simple renewable energy grid, high reliability and efficiency, simple control	Long-distance transmission and voltage conversion are convenient, power generation equipment is simple, and arc is easy to extinguish	Suitable for a variety of renewable energy generation
Disadvantage	The development of DC microgrid protection and grounding technology is limited	Complex to control and use	The cost is high, the structure is complex, and the control is difficult

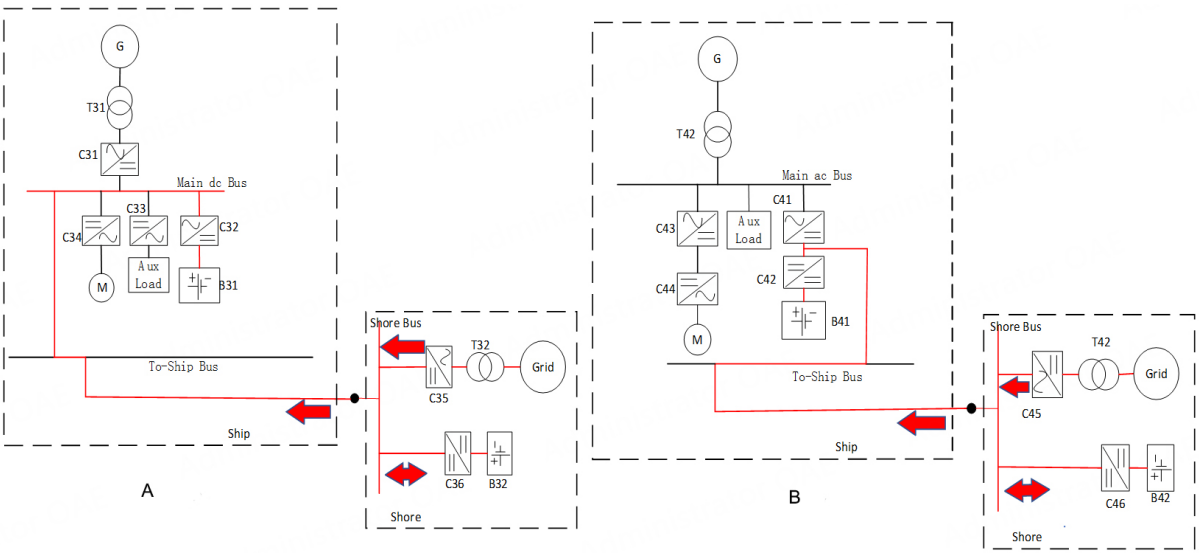

Figure 2. Marine propulsion system based on DC shore power.

method for large-scale new energy access[31], and proposed a joint optimization model that comprehensively considered the output characteristics of energy storage power sources, DC grid transmission capacity, and new energy generation constraints. Ju *et al.* proposed a two-tier robust wind and firewood storage capacity planning model by comprehensively considering the cost parameters[32], wind energy resource uncertainty, and standby demand in the planning process of independent microgrids. Aiming to solve the typical day selection problem of microgrid capacity planning, Zhong *et al.* and Guo *et al.* constructed a comprehensive evaluation index system for typical day selection and proposed a two-stage planning capacity allocation method[33,34].

The first result of the OptimaGRID project determines the scale of renewable resources based on the availability and local needs of renewable energy resources[35]. The design is suitable for a microgrid in the Tanos area of Bayonne Port, which contains a 150 KW photovoltaic array and two 50 KW wind turbines. The 800 KWh REDOX battery has a maximum power of 126.6 kW and an annual energy of 96 MWh. Finally, HOMER and EUROSTAG software are used to determine whether the amount of the microgrid power supply meets the demand of the port and test its dynamic operation. But the system cannot meet the requirements of cold ironing. In order to ensure the continuity of service, Parise *et al.* compare the structure of microgrid and the layout of power generation system[36], so as to ensure the power supply of critical loads in emergency situations in terms of energy management. The power grid includes photovoltaic and wind power generation equipment, with an annual energy of 150-200 MWh and a maximum power of 140 MW. Gennitsaris and Kanellos proposed a multi-agent real-time demand side management system[37] (including reefer containers, berth ships, wind turbines, *etc.*) applicable to cold ironing of freezers in commercial ports

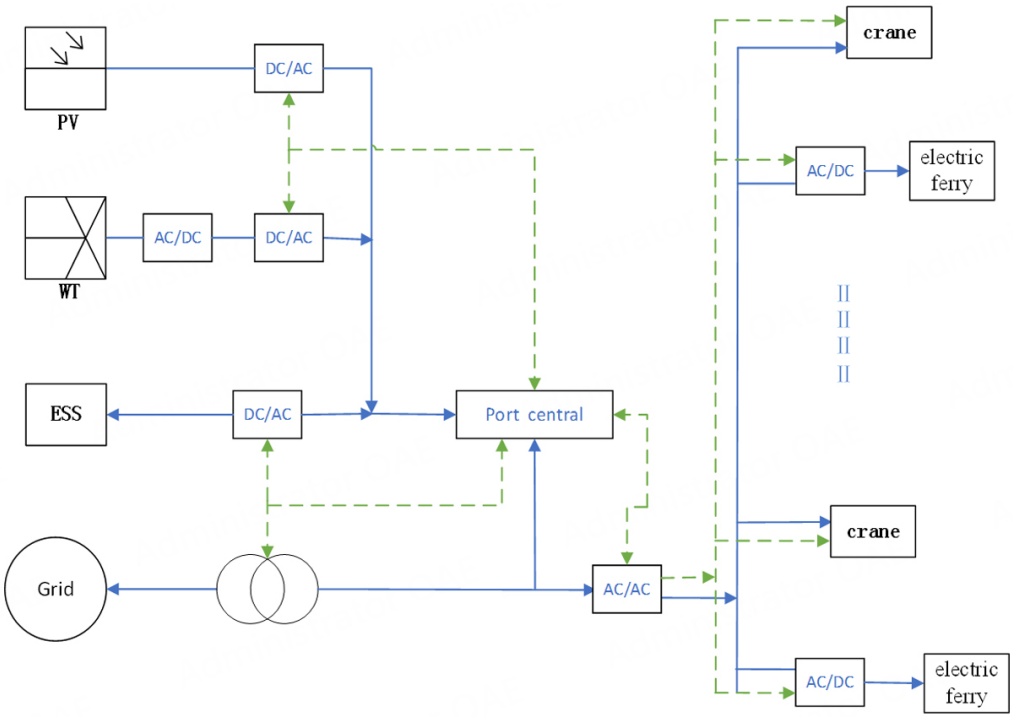

Figure 3. AC/DC hybrid microgrid topology.

and ships, and designed the required communication lines. The system has a maximum power of 30 MW and the required communication lines are designed to minimize operating costs, pollutant emissions and wind power fluctuations. Gutierrez-Romero *et al.* design port power grids that meet the requirements of onshore power supply and RES scale based on the needs of different types of ships[38]. Considering the available area of PV, its output power can reach 9.7 MW, onshore wind turbine 36.3 MW and offshore wind turbine 16 MW, with a daily output of 314 MWh and a maximum power of 13.1 MW. Cold ironing of ships via land power and the use of the RES system can reduce carbon dioxide emissions from moored auxiliary generators by 10,000 tons per year. These three systems include a cold ironing system but no energy storage system. The microgrid referred to Kotrikla *et al.* contains a 5 MW PV system and a 6 MW wind turbine with a daily output of 22 MW hours and a maximum power of 900 kW[39]. While the system also has no energy storage, it connects the surplus of renewable generation to the onshore grid to power other loads. Renewable energy provides the energy needed for cold ironing through the main grid at low power without storage. Ahamad *et al.* introduce the optimal design of microgrid, give the size and energy planning of microgrid, and evaluate the performance of microgrid for load power supply[40]. The integrated system consists of a 200 KW PV, a 4.95 MW wind generator and a 465 MWh grid-connected battery, with a daily output of 39 MWh and a maximum power of 5.2 MW. The optimization results and sensitivity were analyzed by using the HOMER software. Wang *et al.* propose a two-stage optimization framework to solve the optimal design problem of a seaport hybrid renewable energy system[41]. Kumar *et al.* propose a microgrid suitable for electric ferry charging and cold ironing, which includes a 33 MW photovoltaic power generation device, a 30 MW wind turbine, and a 35 MWh lithium-ion battery[42]. However, the system is limited due to line congestion, battery power and capacity.

5. INTELLIGENT CONTROL METHOD AND ENERGY MANAGEMENT STRATEGY OF NEAR PORT MICROGRID SYSTEM

Because the port scale expands unceasingly, the traditional port will bring more energy consumption and harmful gas emissions, noise, such as environmental pollution. Marine exhaust has become one of the major air pollution sources in China's port cities. Construction of green ports and improving port energy using clean purification rate are around the corner. It is necessary to adjust measures to local conditions for the development of distributed photovoltaic (PV) in the harbor and distributed wind. Exploring effective energy management strategies is one of the key aspects when constructing a port microgrid in the future.

5.1. Distributed control method

A harbor microgrid is designed to manage all energy-related issues within a harbor area. However, so far, research on this topic has been limited. Ahamad *et al.* modeled the harbor microgrid and simulated the steady-state and transient behaviors of the harbor microgrid when it provides shore power supply to berthing ships[40]. As the ship enters and leaves the port continuously, there will always be an insertion operation, which may bring a large pulse to the power grid. From this perspective, seaport controls are similar to electric car charging stations. However, since the port microgrid is usually composed of many subsystems, most of which operate independently, the traditional centralized control framework may lead to inefficiency. Distributed control architecture has great advantages in realizing real-time coordination and is not restricted by the above problems. Distributed scheme distributes computing and communication burden to distributed controller and has stronger robustness to communication failure. At present, distributed framework has been widely used in distributed control and automation of land-based power systems. Because of this huge advantage, the distributed control method is also suitable for the control of harbor microgrids. It has good flexibility for network reconfiguration, and its voltage/frequency adjustment facilitates plug and play of the ship in cold ironing mode.

Zhong *et al.* analyzed the problems caused by voltage overlimit and network loss increase caused by large-scale distributed new energy generation access to the safe and stable operation of the distribution network and proposed a data-driven distributed voltage control method for high-proportion new energy generation cluster[43]. Li *et al.* and Deng *et al.* studied the impact of large-scale new energy access on the distribution network and proposed different methods[44,45]. Ma *et al.* and Liu *et al.* put forward a new distributed control method for the current and voltage sharing problem of a DC microgrid[46,47]. Yang *et al.* and He *et al.* applied distributed control technology to port lighting control[48,49], which improved the intelligent management level of port lighting control and reduced the energy consumption of port lighting facilities.

5.2. Energy management for demand response at multiple time scales

Renewable energy generation and load demand change in real time, and thus considering multi-time scale energy management has gradually become the mainstream[50]. Roy *et al.* list the main components of port microgrid, and then review the research on the scale and energy management of port microgrid[51].

For the study of energy management at a long time scale, Chen *et al.* adopt stochastic energy network theory to deal with the power balance problem to optimize the capacity of islanded microgrid for the uncertainty of source and charge[52]. Hu *et al.* propose a two-stage day-ahead energy management strategy including centralized control and distributed control[53]. Li *et al.* consider day-ahead load forecasting and renewable energy forecasting and set the interval as 1 h to propose a distribution optimization strategy[50]. Huang *et al.* propose a scheduling framework based on the two-level model, which adopts the advanced real-time two-stage stochastic optimization method combined with the TOF price mechanism to fully coordinate the energy management decisions of various market stakeholders[54].

For energy management research on a short time scale, in order to improve the system operation reliability and reduce network losses, the drooping slop-reactive power joint optimization is carried out based on the day-ahead scheduling results[55]. Xiao *et al.* establish an intra-day rolling optimal scheduling model based on the model predictive control method to ensure that the microgrid has a certain adjustable capacity while consuming renewable energy[56]. For studies on shorter time scales. Gong *et al.* divide microgrid energy management into five-time scales: 1 day ahead, 30 min to 1 h within the day, 5 to 15 min, 1 min and real-time scheduling, which make the scheduling plan more accurate and reduce the pressure of real-time adjustment[57].

In the study of real-time energy management, Bao *et al.* comprehensively consider different generation side resources to establish a real-time scheduling model and improve the prediction accuracy of wind power[58]. Ma *et al.* develop a real-time and cost-effective residential load scheduling framework[59], whose cost-effectiveness can vary with different consumption patterns and is very sensitive to load behavior. Arun *et al.* propose a heuristic algorithm for real-time load scheduling, which aims to reduce the electricity bill while keeping the total consumption under the maximum demand limit[60]. Ye *et al.* solve the real-time demand-side management problem of microgrids equipped with renewable energy and storage systems, and show that game-theoretic energy scheduling supported by communication networks can smooth the peak-to-average ratio (PAR) of power consumption[61].

In the selection of multiple time scales, the selection of a long time scale is generally 1 day, and the selection of a short time scale is different. A dense time scale will increase the solution time of the scheduling plan, while a sparse time scale will increase the pressure of real-time adjustment. Therefore, it is necessary to select an appropriate time scale for energy management research of microgrids. Table 2 lists the advantages and disadvantages of different time scale controls.

6. SOME COMMERCIALLY OPERATIONAL CASES IN THE WORLD

Jurong Port was built in 1963 and has served Singapore as its main port of entry for more than 50 years. Sunseap Leasing, a unit of Singapore's leading solar system developer Sunseap Group, has partnered with the port to develop the 76,000-square-metre system, which sits atop the Jurong Harbor Warehouse. With a solar power system of 9.5 MWP, the port generates more than 12 million kWh of electricity per year, which is expected to provide 60% of the port's total electricity demand and reduce carbon dioxide emissions by up to 5200 tons per year. The port will further integrate 5 MWp's photovoltaic modules and eventually become the world's first zero-carbon footprint port. Due to the intermittency of PV integration, 10,000 to 15,000 MWh of PV energy per year will remain untapped until 2018. Therefore, Jurong Port urgently needs microgrid technology to facilitate the integration of renewable energy[62].

The port of Hamburg and the city of Hamburg have invested in renewable energy since the German city of Hamburg pioneered wind energy in the early 1990s. Wind energy has been central to Hamburg's renewable energy strategy, with the port area accounting for half of wind energy production and the city also participating in the development of offshore wind farms. Large turbines are being tested off the coast at Cuxhaven and Brunsbuttel, and the scheme is playing a major role in boosting renewable energy in the ports to facilitate the development of solar facilities on the docks and warehouse roofs. Two units are already in service. Hamburg's port also uses solar thermal energy. The HPA office's hot water is generated by a solar thermal unit on the roof, saving 56,000 kW/h of electricity per year.

The Netherlands Energy Research Centre, the Netherlands Institute for Applied Scientific Research, the Netherlands Institute of Oceanography, the ABU Dhabi National Energy Company, and the Ocean Energy

Table 2. Compare multiple time scale management

	Length of time	Advantage	Disadvantage
Long time scale	One day or more than 24 h	Take into account more aspects, and reduce the pressure of real-time adjustment	Limited time domain selection
Short time scale	Not sure (hours, minutes)	Smaller error, more accurate	Not in time
real-time	Within a minute, a few seconds	The response is faster and timelier	The control is complex and error-prone

Table 3. The case of current operation

Country	Harbor	Load	RES
Denmark	Copenhagen[40]	E = 38 MWh/day P_{max} = 5.2 MW	PV (200 KW) WT (4.95 MW)
Greece	Mytilene[39]	E = 22 MWh/day P_{max} = 900 kW	PV (5 MW) WT (6 MW)
USA	Long Beach[36]	E = 150-200 MWh/day P_{max} = 140 MW	PV, WT
Spain	Cartagena[38]	E = 314 MWh/day P_{max} = 13.1 MW	PV (until 9.7 MW) WT (onshore: 36.3 MW; Offshore: 16 MW)
Singapore	Jurong port	E = 200 MWh/day	PV, WT

Company affiliated with the Delft University of Technology, the Netherlands, jointly developed, constructed and operated the world's first offshore floating photovoltaic power station (Bellini,8.5 kW modular PV system). It has been in operation since November 2019 and has successfully withstood multiple storms. The pilot program aims to expand to 50 KWp in the short term and will be tested for a year[63]. Table 3 shows some existing examples of WT and PV generation at some ports.

7. CONCLUSIONS

The development of floating technology and renewable energy generation technology has solved the problem of port energy shortage. However, the floating technology is greatly affected by wind and waves, and the floating power generation platform only stays near the port. Port load capacity is large, and energy management is complex. Flotsam and energy management strategies suitable for ports are being explored. Future renewable energy generation at ports will involve deep sea areas, and thus the use of offshore wind power and energy management will need to be more coordinated. This paper reviews the current utilization of renewable energy and intelligent control strategies of smart seaports. In the future, efficient control strategies of smart seaports will be used to improve energy conversion efficiency and build clean ports.

DECLARATIONS

Acknowledgments

Special thanks to the Intelligent Electrical Science and Technology Research Institute, Northeastern University (China), for providing technical support for this research.

Authors' contributions

Made substantial contributions to conception and design of the study: Li G, Wang T, Zhou B
Provided administrative, technical, and material support: Xiao Z, Yan S, Liu B

Availability of data and materials

Not applicable.

Financial support and sponsorship

This work was supported in part by the State Key Laboratory of Alternate Electrical Power System with Renewable Energy Sources under Grant LAPS21007, in part by the Guang-dong Basic and Applied Basic Research Foundation under Grant 2021A1515110778, in part by the Fundamental Research Funds for the Central Universities Grant N2104014, in part by the Joint Funds of the National Natural Science Foundation of China under Grant U22B20115.

Conflicts of interest

All authors declared that there are no conflicts of interest.

Ethical approval and consent to participate

Not applicable.

Consent for publication

Not applicable.

REFERENCES

1. Wang B. Analysis of greenhouse gas emissions from water transport of cargo ships. *Low Carbon World* 2016;30:229-30. (In Chinese) DOI
2. Hmam S, Olivier JC, Bourguet S, Loron L, Bernard N, Schaeffer E. A cycle-based formulation for the simulation of multi time-scale systems - application to the modeling of the storage system of a fully electric ferry. *Math Comput Simul* 2019;158:403-17. DOI
3. Hamburg harbor port. Available from: https://www.hafen-hamburg.de/cn/homepage/ [Last accessed on 31 Jan 2023].
4. Ningbo Zhoushan harbor port. Available from: http://www.portzhoushan.com/detail/?key=00100&id=4742 [Last accessed on 31 Jan 2023].
5. Fang S, Wang Y, Gou B, Xu Y. Toward future green maritime transportation: an overview of seaport microgrids and all-electric ships. *IEEE Trans Veh Technol* 2019;69:207-219. DOI
6. Kumar J, Kumpulainen L, Kauhaniemi K. Technical design aspects of harbour area grid for shore to ship power: state of the art and future solutions. *Electr Power Energy Syst* 2019;104:840-52. DOI
7. Eleftherios S, Maria B, Alkiviadis T, Nikolaos A. Energy efficiency in european ports: state-of-practice and insights on the way forward. *Sustainability* 2019;11:4952. DOI
8. Sadeghi D, Amiri N, Marzband M, Abusorrah A, Sedraoui K. Optimal sizing of hybrid renewable energy systems by considering power sharing and electric vehicles. *Int J Energy Res* 2022;46. DOI
9. Iris C, Lam JSL. A review of energy efficiency in ports: operational strategies, technologies and energy management systems. *Renew Sustain Energy Rev* 2019;112:170-82. DOI
10. Parise G, Parise L, Martirano L, Chavdarian PB, Su CL, Ferrante A. Wise port and business energy management: port facilities, electrical power distribution. *IEEE Tran Ind Applicat* 2016;52:18-24. DOI
11. Kumar J, Palizban O, Kauhaniemi K. Designing and analysis of innovative solutions for harbour area smart grid. In 2017 IEEE Manchester PowerTech. 2017. DOI
12. Chen JD, Wang J. Development status, trends and prospect of offshore wind power in some foreign countries. *World Sci-Tech R&D* 2014;36:458-64. (In Chinese) DOI
13. Luo K, Guo JB, Ma SC, Wang TZ. Review of key technologies of reliability analysis and improvement for offshore wind power grid integration. *Power Syst Technol* 2022;46:3691-3703. (In Chinese) DOI
14. Ge C, Yan J, Liu YQ, Lu ZX. Review of key technologies for operation control and maintenance of offshore wind farm. *SCEE* 2022;42:4278-92. (In Chinese) DOI
15. Li BB, Wang N, Zhao XD, Xu DG. Flexible converter high voltage large capacity DC transformer for all DC offshore wind farms. *Autom Electric Power Syst* 2022:1-16. (In Chinese) DOI
16. Agrawal KK, Jha SK, Mittal RK, Vashishtha S. Assessment of floating solar PV (FSPV) potential and water conservation: case study on Rajghat Dam in Uttar Pradesh, India. *Energy Sustain Dev* 2022;66:287-95. DOI
17. Trapani K, Redón Santafé M. A review of floating photovoltaic installations: 2007-2013. *Prog Photovoltaics* 2015;23:524-32. DOI
18. Oliveira-Pinto S, Stokkermans J. Marine floating solar plants: an overview of potential, challenges and feasibility. *Maritime Eng* 2020;173:1-39. DOI
19. Sahu A, Yadav N, Sudhakar K. Floating photovoltaic power plant: a review. *Renew Sustain Energy Rev* 2016;66:815-24. DOI

20. Ning YT, Li XJ, Dong DH, Jia XC, Hui D. A review of the research methods of smoothing wind/PV power output with energy storage systems. *Distrib Utilizat* 2017;34:2-11. (In Chinese) DOI
21. Zhao Y, Cui Y. Analysis of optimal design of energy storage configuration based on distributed pv system. In Chinese Society For Environmental Sciences 2022 Annual Conference On Science And Technology. 2022. (In Chinese). DOI
22. Gao XT, Qin ZL, Gao XY. Reliability evaluation of multi-energy generation and transmission system with offshore wind power-photovoltaic-energy storage. *Power Gen Technol* 2022;43:626-35. (In Chinese) DOI
23. Sun YH, Zhao SY, Zhang XL, Han YQ, Zhang HR. Distributed energy storage coordinated operation strategy for improving voltage stability of regional power grid. *Renew Energy Resour* 2022;40:1115-22. (In Chinese) DOI
24. Zhu LJ, Yu ZY. Coordinated control strategy of photovoltaic microgrid based on hybrid energy storage. *Electric Eng* 2022;20:45-8. (In Chinese) DOI
25. Shao SH, Yin FY, Li HJ. Research on control strategy of DC photovoltaic energy storage system. *Electric Mater* 2022;04:15-9. (In Chinese) DOI
26. Karimi S, Zadeh M, Suul JA. Shore charging for plug-in battery-powered ships: power system architecture, infrastructure, and control. *IEEE Electrific Mag* 2020;8:47-61. DOI
27. Dragicevic T, Lu X, Vasquez JC, Guerrero JM. DC Microgrids-Part II: a review of power architectures, applications and standardization issues. *IEEE Trans Power Electr* 2015;3:1. DOI
28. Yu H, Niu SY, Zhang YM. An integrated and reconfigurable hybrid AC/DC microgrid architecture with autonomous power flow control for nearly/net zero energy buildings. *Appl Energy* 2020:263. DOI
29. Yu H, Niu S, Shao Z, Jian L. A scalable and reconfigurable hybrid ac/dc microgrid clustering architecture with decentralized control for coordinated operation. *Int J Electr Power Energy Syst* 2022:135. DOI
30. Xu WD, Luo J, Fan WW. Capacity planning of grid-connected PV-and-storage microgrid under uncertainty. *Syst Eng Theory Pract* 2022;42:981-1000. (In Chinese) DOI
31. Wang F, Li H, Yang L, Zhu Yi. Capacity planning method for flexible DC power grid considering access of large-scale new energy. *CSU-EPSA* 2018;30:53-59. (In Chinese) DOI
32. Ju YT, Li HQ, Yu ZM, Liang Y, Zheng LY. Bi-level robust capacity planning of micro-grid considering multivariate uncertainties and reserve demand. *Power Syst Technol* ;2022:1-20. (In Chinese) DOI
33. Zhong W, Kong FQ, Lin XJ, et al. Two-stage planning method of microgrid capacity considering dynamic weighting of typical day characteristics. *Energy Eng* 2022;42:90-8. (In Chinese) DOI
34. Guo L, Yang SQ, Liu YX, et al. Typical day selection method for capacity planning of microgrid with wind turbine-photovoltaic and energy storage. *CSEE* 2020;40:2468-79. (In Chinese) DOI
35. Khlifi F, Cherif H, Belhadj J. Sizing and multi-objective optimization of a multisource micro-grid with storage for an economic activity zone. In 2019 International Conference on Advanced Systems and Emergent Technologies. 2019. DOI
36. Parise G, Parise L, Pepe FM, Ricci S, Chavdarian P. Innovations in a container terminal area and electrical power distribution for the service continuity. In Industrial & Commercial Power Systems Technical Conference. 2016. DOI
37. Gennitsaris SG, Kanellos FD. Emission-aware and cost-effective distributed demand response system for extensively electrified large ports. *IEEE Trans Power Syst* 2019;34:4341-51. DOI
38. Gutierrez-romero JE, Esteve-pérez J, Zamora B. Implementing onshore power supply from renewable energy sources for requirements of ships at berth. *Appl Energy* 2019;255:113883. DOI
39. Kotrikla AM, Lilas T, Nikitakos N. Abatement of air pollution at an aegean island port utilizing shore side electricity and renewable energy. *Marine Policy* 2017;75:238-8. DOI
40. Ahamad NB, Othman M, Vasquez JC, Guerrero JM, Su CL. Optimal sizing and performance evaluation of a renewable energy based microgrid in future seaports. In 2018 IEEE International Conference on Industrial Technology (ICIT). 2018. DOI
41. Wang W, Peng Y, Li X, Qi Q, Feng P, Zhang Y. A two-stage framework for the optimal design of a hybrid renewable energy system for port application. *Ocean Eng* 2019;191:106555. DOI
42. Kumar J, Parthasarathy C, Västi M, Laaksonen H, Shafie-Khah M, Kauhaniemi K. Sizing and allocation of battery energy storage systems in land islands for large-scale integration of renewables and electric ferry charging stations. *Energies* 2020;13:317. DOI
43. Zhong CY, Gui QJ, Jiang QJ, et al. Data-driven Distributed Voltage Control for High-penetration Renewable Power Clusters Without Complete Model. *J Glob Energy Int* 2022;5:251-60. (In Chinese) DOI
44. Li CP, Dong ZM, Lin JH, et al. Optimal control strategy of distributed energy storage cluster for prompting renewable energy accomodation in distribution network. *Autom Electr Power Syst* 2021;45:76-83. (In Chinese) DOI
45. Dong XW, Pei CC, Deng W, Li B, Dai H. Research on control strategy of distributed energy storage system in distribution network with new energy. *Electr Power Construct* 2021;42:81-9. (In Chinese) DOI
46. Ma HN, Wang LY, Qiu C, et al. Research on distributed control of multiple energy storage systems with different SOC in DC microgrid. *Electr Power Construct* 2022;43:87-95. (In Chinese) DOI
47. Liu S. Study on distributed control of voltage and current in DC micro-grid. *Electr Drive* 2022;52:29-34. (In Chinese) DOI
48. Yang YS, Niu XR, Li LX, et al. Design of port distributed lighting control system based on RT-Thread. *Port Sci Technol* 2022:13-7. (In Chinese) DOI
49. He GJ, Lv CX, Shi FJ, et al. Design on port intelligent lighting control system based on WINCC. *Port Oper* 2018:6-8. (In Chinese) DOI

50. Li BC, Zhang XY, Chen MY. A new operation strategy of optical storage microgrid based on demand side response. *Electr Test* 2020:36-9. (In Chinese) DOI
51. Roy A, Auger F, Olivier JC, Schaeffer E, Auvity B. Design, sizing, and energy management of microgrids in harbor areas: a review. *Energies* 2020;13:5314. DOI
52. Chen JC, Cai ZX, Ma GL. Power capacity optimization of islanded microgrid considering uncertainty oupling and load demand management. *South Power Syst Technol* 2020;14:46-55. (In Chinese) DOI
53. Hu NE, Jiang YQ, Shen YT, Yang XX, Wang ZH. Two-stage day-ahead energy management strategy for microgrid with photovoltaic energy storage. *Mod Electr Power* 2022:1-9. (In Chinese) DOI
54. Huang ZH, Zhang YC, Zheng F, Lin JH, An XL, Shi H. Day-ahead and real-time energy management for active distribution network based on coordinated optimization of different stakeholders. *Power Syst Technol* 2021;45:2299-308. (In Chinese) DOI
55. Sun FZ, Ma JC, Yu Miao, Yu M, Wei W. A day-ahead and intraday coordinated energy management method for active distribution networks based on multi-terminal flexible distribution switch. *CSEE* 2020;40:778-90. (In Chinese) DOI
56. Xiao F, Ai Q. Multiple time-scale optimal dispatch of demand response resource for microgrid based on model predictive control. *Electr Power Autom Equip* 2018;38:184-90. (In Chinese) DOI
57. Gong YF, Lu ZX, Qiao Y, Wang Q, Cao X. Copula theory based machine identification algorithm of high proportion of outliers in photovoltaic power date. *Autom Electr Power Syst* 2016;40:48-55. (In Chinese) DOI
58. Bao YQ, Wang BB, Li Y, Yang SC. Rolling dispatch model considering wind penetration and multi-scale demand response resources. *CSEE* 2016;36:4589-600. (In Chinese) DOI
59. Ma J, Chen HH, Song L, Li Y. Residential load scheduling in smart grid: a cost efficiency perspective. *IEEE Trans Smart Grid* 2016;7:771-84. DOI
60. Arun SL, Selvan MP. Dynamic demand response in smart buildings using an intelligent residential load management system. *IET Gener Transm Distrib* 2017;11:4348-57. DOI
61. Ye F, Qian Y, Hu RQ. A real-time information based demand-side management system in smart grid. *IEEE Trans Parallel Distrib Syst* 2016;27:329-39. DOI
62. Jurong harbor port. Available from: https://baike.baidu.com/item/%E8%A3%95%E5%BB%8A%E6%B8%AF/3051430?fr=aladdin 2022 [Last accessed on 31 Jan 2023].
63. Offshore floating photovoltaic Power Station (Bellini). Available from: https://baijiahao.baidu.com/s?id=1709751573887040158&wfr=spider&for=pc, 2022 [Last accessed on 31 Jan 2023].

AUTHOR INSTRUCTIONS

1. Submission Overview

Before you decide to publish with *Complex Engineering Systems* (*CES*), please read the following items carefully and make sure that you are well aware of Editorial Policies and the following requirements.

1.1 Topic Suitability

The topic of the manuscript must fit the scope of the journal. Please refer to Aims and Scope for more information.

1.2 Open Access and Copyright

The journal adopts Gold Open Access publishing model and distributes content under the Creative Commons Attribution 4.0 International License. Copyright is retained by authors. Please make sure that you are well aware of these policies.

1.3 Publication Fees

CES is an open access journal. When a paper is accepted for publication, authors are required to pay Article Processing Charges (APCs) to cover its editorial and production costs. The APC for each submission is $600. There are no additional charges based on color, length, figures, or other elements. For more details, please refer to OAE Publication Fees.

1.4 Language Editing

All submissions are required to be presented clearly and cohesively in good English. Authors whose first language is not English are advised to have their manuscripts checked or edited by a native English speaker before submission to ensure the high quality of expression. A well-organized manuscript in good English would make the peer review even the whole editorial handling more smoothly and efficiently.

If needed, authors are recommended to consider the language editing services provided by Charlesworth to ensure that the manuscript is written in correct scientific English before submission. Authors who publish with OAE journals enjoy a special discount for the services of Charlesworth via the following two ways.
Submit your manuscripts directly at http://www.charlesworthauthorservices.com/~OAE;
Open the link http://www.charlesworthauthorservices.com/, and enter Promotion Code “OAE” when you

1.5 Work Funded by the National Institutes of Health

If an accepted manuscript was funded by National Institutes of Health (NIH), the author may inform editors of the NIH funding number. The editors are able to deposit the paper to the NIH Manuscript Submission System on behalf of the author.

2. Submission Preparation

2.1 Cover Letter

A cover letter is required to be submitted accompanying each manuscript. Here is a guideline of a cover letter for authors’ consideration:

List the highlights of the current manuscript and no more than 5 short sentences;

All authors have read the final manuscript, have approved the submission to the journal, and have accepted full responsibilities pertaining to the manuscript’s delivery and contents;

Clearly state that the manuscript is an original work on its own merit, that it has not been previously published in whole or in part, and that it is not being considered for publication elsewhere;

No materials are reproduced from another source (if there is material in your manuscript that has been reproduced from another source, please state whether you have obtained permission from the copyright holder to use them);

Conflicts of interest statement;

If the manuscript is contributed to a Special Issue, please also mention it in the cover letter;

If the manuscript was presented partly or entirely in a conference, the author should clearly state the background information of the event, including the conference name, time, and place in the cover letter.

2.2 Types of Manuscripts

There is no restriction on the length of manuscripts, number of figures, tables and references, provided that the manuscript is concise and comprehensive. The journal publishes Research Article, Review, Technical Note, *etc*. For more details about paper type, please refer to the following table.

Manuscript Type	Definition	Word Limit	Abstract	Keywords	Main Text Structure
Research Article	A Research Article is a seminal and insightful research study and showcases that often involves modern techniques or methodologies. Authors should justify that their work is of novel findings	8000 max	The abstract should state briefly the purpose of the research, the principal results and major conclusions. No more than 250 words	3-8 keywords	The main content should include four sections: Introduction, Methods, Results and Discussion
Review	A Review should be an authoritative, well balanced, and critical survey of recent progress in an attractive or a fundamental research field	10000 max	Unstructured abstract. No more than 250 words	3-8 keywords	The main text may consist of several sections with unfixed section titles. We suggest that the author include an "Introduction" section at the beginning, several sections with unfixed titles in the middle part, and a "Conclusions" section at the end
Technical Note	A Technical Note is a short article giving a brief description of a specific development, technique, or procedure, or it may describe a modification of an existing technique, procedure or device applied in research	3500 max	Unstructured abstract. No more than 250 words	3-8 keywords	/
Editorial	An Editorial is a short article describing news about the journal or opinions of senior Editors or the publisher	1000 max	None required	None required	/
Commentary	A Commentary is to provide comments on a newly published article or an alternative viewpoint on a certain topic	2500 max	Unstructured abstract. No more than 250 words	3-8 keywords	/
Perspective	A Perspective provides personal points of view on the state-of-the-art of a specific area of knowledge and its future prospects	2000 max	Unstructured abstract. No more than 250 words	3-8 keywords	/

2.3 Manuscript Structure

2.3.1 Front Matter

2.3.1.1 Title

The title of the manuscript should be concise, specific and relevant, with no more than 16 words if possible.

2.3.1.2 Authors and Affiliations

Authors' full names should be listed. The initials of middle names can be provided. The affiliations and email addresses for all authors should be listed. At least one author should be designated as the corresponding author. In addition, corresponding authors are suggested to provide their Open Researcher and Contributor ID upon submission. Please note that any change to authorship is not allowed after manuscript acceptance. The authors' affiliations should be provided in this format: department, institution, city, postcode, country.

2.3.1.3 Abstract

The abstract should be a single paragraph with word limitation and specific structure requirements (for more details please refer to Types of Manuscripts). It usually describes the main objective(s) of the study, explains how the study was done, including any model organisms used, without methodological detail, and summarizes the most important results and their significance. The abstract must be an objective representation of the study: it is not allowed to contain results that are not presented and substantiated in the manuscript, or exaggerate the main conclusions. Citations should not be included in the abstract.

2.3.1.4 Graphical Abstract

The graphical abstract is essential as this can catch first view of your publication by readers. We recommend you submit an eye-catching figure. It should summarize the content of the article in a concise graphical form. It is recommended to use it because this can make online articles get more attention.

The graphical abstract should be submitted as a separate document in the online submission system. Please provide an image with a minimum of 531 × 1,328 pixels (h × w) or proportionally more. The image should be readable at a size of 5 cm × 13 cm using a regular screen resolution of 96 dpi. Preferred file types: TIFF, PSD, AI, JPEG, and EPS files.

2.3.1.5 Keywords

Three to eight keywords should be provided, which are specific to the article, yet reasonably common within the subject discipline.

Sections 2.3.1.1 and 2.3.1.2 should appear in all manuscript types.

2.3.2 Main Text

Manuscripts of different types are structured with different sections of content. Please refer to Types of Manuscripts to make sure which sections should be included in the manuscripts.

2.3.2.1 Introduction

The introduction should contain background that puts the manuscript into context, allow readers to understand why the study is important, include a brief review of key literature, and conclude with a brief statement of the overall aim of the work and a comment about whether that aim was achieved. Relevant controversies or disagreements in the field should be introduced as well.

2.3.2.2 Methods

The methods should contain sufficient details to allow others to fully replicate the study. New methods and protocols should be described in detail while well-established methods can be briefly described or appropriately cited. Statistical terms, abbreviations, and all symbols used should be defined clearly. Protocol documents for clinical trials, observational studies, and other non-laboratory investigations may be uploaded as supplementary materials.

2.3.2.3 Results

This section contains the findings of the study. Results of statistical analysis should also be included either as text or as tables or figures if appropriate. Authors should emphasize and summarize only the most important observations. Data on all primary and secondary outcomes identified in the section Methods should also be provided. Extra or supplementary materials and technical details can be placed in supplementary documents.

2.3.2.4 Discussion

This section should discuss the implications of the findings in context of existing research and highlight limitations of the study. Future research directions may also be mentioned.

2.3.2.5 Conclusion

It should state clearly the main conclusions and include the explanation of their relevance or importance to the field.

2.3.3 Back Matter

The following sections should appear in all manuscript types.

2.3.3.1 Acknowledgments

Anyone who contributed towards the article but does not meet the criteria for authorship, including those who provided professional writing services or materials, should be acknowledged. Authors should obtain permission to acknowledge from all those mentioned in the Acknowledgments section. This section is not added if the author does not have anyone to acknowledge.

2.3.3.2 Authors' Contributions

Each author is expected to have made substantial contributions to the conception or design of the work, or the acquisition, analysis, or interpretation of data, or the creation of new software used in the work, or have drafted the work or substantively revised it.

Please use Surname and Initial of Forename to refer to an author's contribution. For example: made substantial contributions to conception and design of the study and performed data analysis and interpretation: Salas H, Castaneda WV; performed data acquisition, as well as providing administrative, technical, and material support: Castillo N, Young V.

If an article is single-authored, please include "The author contributed solely to the article." in this section.

2.3.3.3 Availability of Data and Materials

In order to maintain the integrity, transparency and reproducibility of research records, authors should include this section in their manuscripts, detailing where the data supporting their findings can be found. Data can be deposited into data repositories or published as supplementary information in the journal. Authors who cannot share their data should state that the data will not be shared and explain it. If a manuscript does not involve such issues, please state "Not applicable." in this section.

2.3.3.4 Financial Support and Sponsorship

All sources of funding for the study reported should be declared. The role of the funding body in the experiment design, collection, analysis and interpretation of data, and writing of the manuscript should be declared. Any relevant grant numbers and the link of funder's website should be provided if any. If the study is not involved with this issue, state "None." in this section.

2.3.3.5 Conflicts of Interest

Authors must declare any potential conflicts of interest that may be perceived as inappropriately influencing the representation or interpretation of reported research results. If there are no conflicts of interest, please state "All authors declared that there are no conflicts of interest." in this section. Some authors may be bound by confidentiality agreements. In such cases, in place of itemized disclosures, we will require authors to state "All authors declared that they are bound by confidentiality agreements that prevent them from disclosing their conflicts of interest in this work.". If authors are unsure whether conflicts of interest exist, please refer to the "Conflicts of Interest" of *Complex Engineering Systems* (*CES*) Editorial Policies for a full explanation.

2.3.3.6 Ethical Approval and Consent to Participate

Research involving human subjects, human material or human data must be performed in accordance with the Declaration of Helsinki and approved by an appropriate ethics committee. An informed consent to participate in the study should also be obtained from participants, or their parents or legal guardians for children under 16. A statement detailing the name of the ethics committee (including the reference number where appropriate) and the informed consent obtained must appear in the manuscripts reporting such research.

Studies involving animals and cell lines must include a statement on ethical approval. More information is available at Editorial Policies.

If the manuscript does not involve such issues, please state "Not applicable." in this section.

2.3.3.7 Consent for Publication

Manuscripts containing individual details, images or videos, must obtain consent for publication from that person, or in the case of children, their parents or legal guardians. If the person has died, consent for publication must be obtained from the next of kin of the participant. Manuscripts must include a statement that written informed consent for publication was obtained. Authors do not have to submit such content accompanying the manuscript. However, these documents must be available if requested. If the manuscript does not involve this issue, state "Not applicable." in this section.

2.3.3.8 Copyright

Authors retain copyright of their works through a Creative Commons Attribution 4.0 International License that clearly states how readers can copy, distribute, and use their attributed research, free of charge. A declaration "© The Author(s) 2023." will be added to each article. Authors are required to sign a License to Publish before formal publication.

2.3.3.9 References

References should be numbered in order of appearance at the end of manuscripts. In the text, reference numbers should be placed in square brackets and the corresponding references are cited thereafter. List all authors when the number of authors

is less than or equal to six, if there are more than six authors, only the first three authors' names should be listed, other authors' names should be omitted and replaced with "et al.". The journal's name should be required to be italicized and the journal references should have corresponding DOI numbers. Information from manuscripts accepted but not published should be cited in the text as "Unpublished material" with written permission from the source. Journal names should be abbreviated according to the List of Title Word Abbreviations.

References should be described as follows, depending on the types of works:

Types	**Examples**
Journal articles by individual authors	Cao MS, Pan LX, Gao YF, et al. Neural network ensemble-based parameter sensitivity analysis in civil engineering systems. *Neural Comput Applic* 2017;28:1583-90. [DOI: 10.1007/s00521-015-2132-4]
Organization as author	Diabetes Prevention Program Research Group. Hypertension, insulin, and proinsulin in participants with impaired glucose tolerance. *Hypertension* 2002;40:679-86. [DOI: 10.1161/01.hyp.0000035706.28494.09]
Both personal authors and organization as author	Vallancien G, Emberton M, Harving N, van Moorselaar RJ; Alf-One Study Group. Sexual dysfunction in 1,274 European men suffering from lower urinary tract symptoms. *J Urol* 2003;169:2257-61. [DOI: 10.1097/01.ju.0000067940.76090.73]
Journal articles not in English	Mao X, Ding YK. Sentiment feature analysis and harmonic sense evaluation of images. *J Electronic* 2001;29:23-7. (in Chinese)
Journal articles ahead of print	Albasir A, Hu Q, Naik K, Naik N. Unsupervised detection of security threats in cyberphysical system and IoT devices based on power fingerprints and RBM autoencoders. *J Surveill Secur Saf* 2021; Epub ahead of print [DOI: 10.20517/jsss.2020.19]
Books	Gaydon AG, Wolfhard HG. Flames. 2nd ed. London: Chapman and Hall Ltd.; 1960. pp. 10-20.
Book chapters	Chothia T, Smirnov V. A traceability attack against e-passports. In: Sion R, Editor. Financial cryptography. Lecture notes in computer science. Springer; 2010. pp. 20-34..
Online resource	Intel Technology Journal. Developing smart toys - from idea to product. Available from: https://www.intel.com/content/dam/www/public/us/en/documents/research/2001-vol05-iss-4-intel-technology-journal.pdf. [Last accessed on 20 Feb 2021]
Conference proceedings	Harnden P, Joffe JK, Jones WG, Editors. Germ cell tumours V. Proceedings of the 5th Germ Cell Tumour Conference; 2001 Sep 13-15; Leeds, UK. New York: Springer; 2002..
Conference paper	Christensen S, Oppacher F. An analysis of Koza's computational effort statistic for genetic programming. In: Foster JA, Lutton E, Miller J, Ryan C, Tettamanzi AG, Editors. Genetic programming. EuroGP 2002: Proceedings of the 5th European Conference on Genetic Programming; 2002 Apr 3-5; Kinsdale, Ireland. Berlin: Springer; 2002. pp. 182-91.
Unpublished material	Tian D, Araki H, Stahl E, Bergelson J, Kreitman M. Signature of balancing selection in Arabidopsis. Proc Natl Acad Sci U S A. Forthcoming 2002.

The journal also recommends that authors prepare references with a bibliography software package, such as EndNote to avoid typing mistakes and duplicated references.

2.3.3.10 Supplementary Materials

Additional data and information can be uploaded as Supplementary Materials to accompany the manuscripts. The supplementary materials will also be available to the referees as part of the peer-review process. Any file format is acceptable, such as data sheet (word, excel, csv, cdx, fasta, pdf or zip files), presentation (powerpoint, pdf or zip files), image (cdx, eps, jpeg, pdf, png or tiff), table (word, excel, csv or pdf), audio (mp3, wav or wma) or video (avi, divx, flv, mov, mp4, mpeg, mpg or wmv). All information should be clearly presented. Supplementary materials should be cited in the main text in numeric order (e.g., Supplementary Figure 1, Supplementary Figure 2, Supplementary Table 1, Supplementary Table 2, *etc*.). The style of supplementary figures or tables complies with the same requirements on figures or tables in main text. Videos and audios should be prepared in English, and limited to a size of 500 MB.

2.4 Manuscript Format

2.4.1 File Format

Manuscript files can be in DOC and DOCX formats and should not be locked or protected.

Manuscript prepared in LaTex must be collated into one ZIP folder (including all source files and images, so that the Editorial Office can recompile the submitted PDF).

When preparing manuscripts in different file formats, please use the corresponding Manuscript Templates.

2.4.2 Length

There are no restrictions on paper length, number of figures, or number of supporting documents. Authors are encouraged

to present and discuss their findings concisely.

2.4.3 Language

Manuscripts must be written in English.

2.4.4 Multimedia Files

The journal supports manuscripts with multimedia files. The requirements are listed as follows:

Video or audio files are only acceptable in English. The presentation and introduction should be easy to understand. The frames should be clear, and the speech speed should be moderate;
A brief overview of the video or audio files should be given in the manuscript text;
The video or audio files should be limited to a size of up to 500 MB;
Please use professional software to produce high-quality video files, to facilitate acceptance and publication along with the submitted article. Upload the videos in mp4, wmv, or rm format (preferably mp4) and audio files in mp3 or wav format.

2.4.5 Figures

Figures should be cited in numeric order (e.g., Figure 1, Figure 2) and placed after the paragraph where it is first cited;

Figures can be submitted in format of TIFF, PSD, AI, EPS or JPEG, with resolution of 300-600 dpi;

Figure caption is placed under the Figure;

Diagrams with describing words (including, flow chart, coordinate diagram, bar chart, line chart, and scatter diagram, *etc.*) should be editable in word, excel or powerpoint format. Non-English information should be avoided;

Labels, numbers, letters, arrows, and symbols in figure should be clear, of uniform size, and contrast with the background;

Symbols, arrows, numbers, or letters used to identify parts of the illustrations must be identified and explained in the legend;

Internal scale (magnification) should be explained and the staining method in photomicrographs should be identified;

All non-standard abbreviations should be explained in the legend;

Permission for use of copyrighted materials from other sources, including re-published, adapted, modified, or partial figures and images from the internet, must be obtained. It is authors' responsibility to acquire the licenses, to follow any citation instruction requested by third-party rights holders, and cover any supplementary charges.

2.4.6 Tables

Tables should be cited in numeric order and placed after the paragraph where it is first cited;

The table caption should be placed above the table and labeled sequentially (e.g., Table 1, Table 2);

Tables should be provided in editable form like DOC or DOCX format (picture is not allowed);

Abbreviations and symbols used in table should be explained in footnote;

Explanatory matter should also be placed in footnotes;

Permission for use of copyrighted materials from other sources, including re-published, adapted, modified, or partial tables from the internet, must be obtained. It is authors' responsibility to acquire the licenses, to follow any citation instruction requested by third-party rights holders, and cover any supplementary charges.

2.4.7 Abbreviations

Abbreviations should be defined upon first appearance in the abstract, main text, and in figure or table captions and used consistently thereafter. Non-standard abbreviations are not allowed unless they appear at least three times in the text. Commonly-used abbreviations, such as DNA, RNA, ATP, *etc.*, can be used directly without definition. Abbreviations in titles and keywords should be avoided, except for the ones which are widely used.

2.4.8 Italics

General italic words like vs., et al., etc., in vivo, in vitro; t test, F test, U test; related coefficient as r, sample number as n, and probability as P; names of genes; names of bacteria and biology species in Latin.

2.4.9 Units

SI Units should be used. Imperial, US customary and other units should be converted to SI units whenever possible. There is a space between the number and the unit (i.e., 23 mL). Hour, minute, second should be written as h, min, s.

2.4.10 Numbers

Numbers appearing at the beginning of sentences should be expressed in English. When there are two or more numbers in a paragraph, they should be expressed as Arabic numerals; when there is only one number in a paragraph, number < 10 should be expressed in English and number > 10 should be expressed as Arabic numerals. 12345678 should be written as 12,345,678.

2.4.11 Equations

Equations should be editable and not appear in a picture format. Authors are advised to use either the Microsoft Equation Editor or the MathType for display and inline equations.

Display equations should be numbered consecutively, using Arabic numbers in parentheses;
Inline equations should not be numbered, with the same/similar size font used for the main text.

2.4.12 Headings

In the main body of the paper, three different levels of headings may be used.

Level one headings: they should be in bold, and numbered using Arabic numbers, such as 1. INTRODUCTION, and 2. METHODS, with all letters capitalized;
Level two headings: they should be in bold and numbered after the level one heading, such as 2.1 Statistical analyses, 2.2 ..., 2.3..., *etc*., with the first letter capitalized;
Level three headings: they should be italicized, and numbered after the level two heading, such as 2.1.1 Data distributions,and 2.1.2 outliers and linear regression, with the first letter capitalized.

2.4.13 Text Layout

As the electronic submission will provide the basic material for typesetting, it is important to prepare papers in the general editorial style of the journal.

The font is Times New Roman;
The font size is 12pt;
Single column, 1.5x line spacing;
Insert one line break (one Return) before the heading and paragraph, if the heading and paragraph are adjacent, insert a line break before the heading only;
No special indentation;
Alignment is left end;
Insert consecutive line numbers;
For other details please refer to the Manuscript Templates.

2.5 Submission Link

Submit an article via https://oaemesas.com/login?JournalId=comengsys.

3. Research and Publication Ethics

3.1 Research Involving Human Subjects

All studies involving human subjects must be in accordance with the Helsinki Declaration and seek approval to conduct the study from an independent local, regional, or national review body (e.g., ethics committee, institutional review board, *etc*.). Such approval, including the names of the ethics committee, institutional review board, *etc*., must be listed in a declaration statement of Ethical Approval and Consent to Participate in the manuscript. If the study is judged exempt from ethics approval, related information (e.g., name of the ethics committee granting the exemption and the reason for the exemption) must be listed. Further documentation on ethics should also be prepared, as Editors may request more detailed information. Manuscripts with suspected ethical problems will be investigated according to COPE Guidelines.

3.1.1 Consent to Participate

For all studies involving human subjects, informed consent to participate in the studies must be obtained from participants, or their parents or legal guardians for children under 16. Statements regarding consent to participate should be included in a declaration statement of Ethical Approval and Consent to Participate in the manuscript. If informed consent is not required, the name of the ethics committee granting the exemption and the reason for the exemption must be listed. If any ethical violation is found at any stage of publication, the issue will be investigated seriously based on COPE Guidelines.

3.1.2 Consent for Publication

All articles published by OAE are freely available on the Internet. All manuscripts that include individual participants' data in any form (i.e., details, images, videos, *etc.*) will not be published without Consent for Publication obtained from that person(s), or for children, their parents, or legal guardians. If the person has died, Consent for Publication must be obtained from the next of kin. Authors must add a declaration statement of Consent for Publication in the manuscript, specifying written informed consent for publication has been obtained.

3.1.3 Trial Registration

OAE requires all authors to register all relevant clinical trials that are reported in manuscripts submitted. OAE follows the World Health Organization (WHO)'s definition of clinical trials: "A clinical trial is any research study that prospectively assigns human participants or groups of humans to one or more health-related interventions to evaluate the effects on health outcomes. Interventions include but are not restricted to drugs, cells, other biological products, surgical procedures, radiologic procedures, devices, behavioral treatments, process-of-care changes, preventive care, *etc.*".

In line with International Committee of Medical Journal Editors (ICMJE) Recommendations, OAE requires the registration of clinical trials in a public trial registry at or before the time of first patient enrollment. OAE accepts publicly accessible registration in any registry that is a primary register of the WHO International Clinical Trials Registry Platform or in ClinicalTrials.gov. The trial registration number should be listed at the end of the Abstract section.

Secondary data analyses of primary (parent) clinical trials should not be registered as a new clinical trial, but rather reference the trial registration number of the primary trial.

Editors of OAE journals will consider carefully whether studies failed to register or had an incomplete trial registration. Because of the importance of prospective trial registration, if there is an exception to this policy, trials must be registered and the authors should indicate in the publication when registration was completed and why it was delayed. Editors will publish a statement indicating why an exception was allowed. Please note such exceptions should be rare, and authors failing to prospectively register a trial risk its inadmissibility to OAE journals.

Authors who are not sure whether they need trial registration may refer to ICMJE FAQs for further information.

3.2 Research Involving Animals

Experimental research on animals should be approved by an appropriate ethics committee and must comply with institutional, national, or international guidelines. OAE encourages authors to comply with the AALAS Guidelines, the ARRIVE Guidelines, and/or the ICLAS Guidelines, and obtain prior approval from the relevant ethics committee. Manuscripts must include a statement indicating that the study has been approved by the relevant ethical committee and the whole research process complies with ethical guidelines. If a study is granted an exemption from requiring ethics approval, the name of the ethics committee granting the exemption and the reason(s) for the exemption should be detailed. Editors will take account of animal welfare issues and reserve the right to reject a manuscript, especially if the research involves protocols that are inconsistent with commonly accepted norms of animal research.

3.3 Research Involving Cell Lines

Authors must describe what cell lines are used and their origin so that the research can be reproduced. For established cell lines, the provenance should be stated and references must also be given to either a published paper or to a commercial source. For de novo cell lines derived from human tissue, appropriate approval from an institutional review board or equivalent ethical committee, and consent from the donor or next of kin, should be obtained. Such statements should be listed on the Declaration section of Ethical Approval and Consent to Participate in the manuscript.

Further information is available from the International Cell Line Authentication Committee (ICLAC). OAE recommends that authors check the NCBI database for misidentification and contamination of human cell lines.

3.4 Research Involving Plants

Experimental research on plants (either cultivated or wild), including collection of plant material, must comply with institutional, national, or international guidelines. Field studies should be conducted in accordance with local legislation, and the manuscript should include a statement specifying the appropriate permissions and/or licenses. OAE recommends that authors comply with the IUCN Policy Statement on Research Involving Species at Risk of Extinction and the Convention on the Trade in Endangered Species of Wild Fauna and Flora.

For each submitted manuscript, supporting genetic information and origin must be provided for plants that were utilized. For research manuscripts involving rare and non-model plants (other than, e.g., Arabidopsis thaliana, Nicotiana benthamiana, Oriza sativa, or many other typical model plants), voucher specimens must be deposited in a public herbarium or other public collections providing access to deposited materials.

3.5 Publication Ethics Statement

OAE is a member of the Committee on Publication Ethics (COPE). We fully adhere to its Code of Conduct and to its Best Practice Guidelines.

The Editors of this journal enforce a rigorous peer-review process together with strict ethical policies and standards to guarantee to add high-quality scientific works to the field of scholarly publication. Unfortunately, cases of plagiarism, data falsification, image manipulation, inappropriate authorship credit, and the like, do arise. The Editors of *CES* take such publishing ethics issues very seriously and are trained to proceed in such cases with zero tolerance policy.

Authors wishing to publish their papers in *CES* must abide by the following:

The author(s) must disclose any possibility of a conflict of interest in the paper prior to submission;
The authors should declare that there is no academic misconduct in their manuscript in the cover letter;
Authors should accurately present their research findings and include an objective discussion of the significance of their findings;
Data and methods used in the research need to be presented in sufficient detail in the manuscript so that other researchers can replicate the work;
Authors should provide raw data if referees and the Editors of the journal request;
Simultaneous submission of manuscripts to more than one journal is not tolerated;
Republishing content that is not novel is not tolerated (for example, an English translation of a paper that is already published in another language will not be accepted);
The manuscript should not contain any information that has already been published. If you include already published figures or images, please get the necessary permission from the copyright holder to publish under the CC-BY license;
Plagiarism, data fabrication and image manipulation are not tolerated;
Plagiarism is not acceptable in OAE journals.

Plagiarism involves the inclusion of large sections of unaltered or minimally altered text from an existing source without appropriate and unambiguous attribution, and/or an attempt to misattribute original authorship regarding ideas or results, and copying text, images, or data from another source, even from your own publications, without giving credit to the source. As to reusing the text that is copied from another source, it must be between quotation marks and the source must be cited. If a study's design or the manuscript's structure or language has been inspired by previous studies, these studies must be cited explicitly.

If plagiarism is detected during the peer-review process, the manuscript may be rejected. If plagiarism is detected after publication, we may publish a Correction or retract the paper.

Falsification is manipulating research materials, equipment, or processes, or changing or omitting data or results so that the findings are not accurately represented in the research record.

Image files must not be manipulated or adjusted in any way that could lead to misinterpretation of the information provided by the original image.

Irregular manipulation includes: introduction, enhancement, moving, or removing features from the original image; grouping of images that should be presented separately, or modifying the contrast, brightness, or color balance to obscure, eliminate, or enhance some information.

If irregular image manipulation is identified and confirmed during the peer-review process, we may reject the manuscript. If irregular image manipulation is identified and confirmed after publication, we may publish a Correction or retract the paper.

OAE reserves the right to contact the authors' institution(s) to investigate possible publication misconduct if the Editors find conclusive evidence of misconduct before or after publication. OAE has a partnership with iThenticate, which is the most trusted similarity checker. It is used to analyze received manuscripts to avoid plagiarism to the greatest extent possible. When plagiarism becomes evident after publication, we will retract the original publication or require modifications, depending on the degree of plagiarism, context within the published article, and its impact on the overall integrity of the published study. Journal Editors will act under the relevant COPE guidelines.

4. Authorship

Authorship credit of *CES* should be solely based on substantial contributions to a published study, as specified in the

following four criteria:

1. Substantial contributions to the conception or design of the work, or the acquisition, analysis, or interpretation of data for the work;
2. Drafting the work or revising it critically for important intellectual content;
3. Final approval of the version to be published;
4. Agreement to be accountable for all aspects of the work in ensuring that questions related to the accuracy or integrity of any part of the work are appropriately investigated and resolved.

All those who meet these criteria should be identified as authors. Authors must specify their contributions in the section Authors'' Contributions of their manuscripts. Contributors who do not meet all the four criteria (like only involved in acquisition of funding, general supervision of a research group, general administrative support, writing assistance, technical editing, language editing, proofreading, *etc*.) should be acknowledged in the section of Acknowledgement in the manuscript rather than being listed as authors.

If a large multiple-author group has conducted the work, the group ideally should decide who will be authors before the work starts and confirm authors before submission. All authors of the group named as authors must meet all the four criteria for authorship.

AI and AI-assisted technologies should not be listed as an author or co-author.

5. Reviewers Exclusions

You are welcome to exclude a limited number of researchers as potential Editors or reviewers of your manuscript. To ensure a fair and rigorous peer review process, we ask that you keep your exclusions to a maximum of three people. If you wish to exclude additional referees, please explain or justify your concerns—this information will be helpful for Editors when deciding whether to honor your request.

6. Editors and Journal Staff as Authors

Editorial independence is extremely important and OAE does not interfere with Editorial decisions. Editorial staff or Editors shall not be involved in processing their own academic work. Submissions authored by Editorial staff/Editors will be assigned to at least three independent outside reviewers. Decisions will be made by the Editor-in-Chief, including Special Issue papers. Journal staff are not involved in the processing of their own work submitted to any OAE journals.

7. Policy of the Use of AI and AI-assisted Technologies in Scientific Writing

Generative AI and AI-assisted technologies (e.g., large language models) are expected to be increasingly used to create content. In the writing process of manuscripts, using AI and AI-assisted technologies to complete key researcher work, such as producing scientific insights, analyzing and interpreting data or drawing scientific conclusions, is not allowed, and they should only be used to improve the readability and language of manuscripts.

AI and AI-assisted technologies should be used under human control and supervision as they may generate incorrect or prejudiced output, and they should not be listed as an author or co-author, nor cited as an author.

The use of AI and AI-assisted technologies should be disclosed by authors in their manuscripts, and a statement will be required in the final publication.

OAE will keep monitoring the development and adjust the policy when necessary.

8. Conflict of Interests

OAE journals require authors to declare any possible financial and/or non-financial conflicts of interest at the end of their manuscript and in the cover letter, as well as confirm this point when submitting their manuscript in the submission system. If no conflicts of interest exist, authors need to state "All authors declared that there are no conflicts of interest". We also recognize that some authors may be bound by confidentiality agreements, in which cases authors need to state "All authors declared that they are bound by confidentiality agreements that prevent them from disclosing their competing interests in this work".OAE will keep monitoring the development and adjust the policy when necessary.

9. Editorial Process

9.1 Pre-Check

New submissions are initially checked by the Managing Editor from the perspectives of originality, suitability, structure and formatting, conflicts of interest, background of authors, *etc*. Poorly prepared manuscripts may be rejected at this stage. If your manuscript does not meet one or more of these requirements, we will return it for further revisions.

Once your manuscript has passed the initial check, it will be assigned to the Assistant Editor, and then the Editor-in-Chief, or an Associate Editor in the case of a conflict of interest, will be notified of the submission and invited to review. Regarding Special Issue paper, after passing the initial check, the manuscript will be successively assigned to the Assistant Editor, and then to the Editor-in-Chief, or an Associate Editor in the case of conflict of interest for the Editor-in-Chief to review. The Editor-in-Chief, or the Associate Editor may reject manuscripts that they deem highly unlikely to pass peer review without further consultation. Once your manuscript has passed the Editorial assessment, the Associate Editor will start to organize peer-review.

All manuscripts submitted to *CES* are screened using CrossCheck powered by iThenticate to identify any plagiarized content. Your study must also meet all ethical requirements as outlined in our Editorial Policies. If the manuscript does not pass any of these checks, we may return it to you for further revisions or decline to consider your study for publication.

9.2 Peer Review

CES operates a single-blind review process, which means that reviewers know the names of authors, but the names of the reviewers are hidden from the authors. The scientific quality of the research described in the manuscript is assessed by a minimum of three independent expert reviewers. The Editor-in-Chief is responsible for the final decision regarding acceptance or rejection of the manuscript.

All information contained in your manuscript and acquired during the review process will be held in the strictest confidence.

9.3 Decisions

Your research will be judged on scientific soundness only, not on its perceived impact as judged by Editors or referees. There are three possible decisions: Accept (your study satisfies all publication criteria), Invitation to Revise (more work is required to satisfy all criteria), and Reject (your study fails to satisfy key criteria and it is highly unlikely that further work can address its shortcomings). All of the following publication criteria must be fulfilled to enable your manuscript to be accepted for publication:

Originality

The study reports original research and conclusions.

Data availability

All data to support the conclusions either have been provided or are otherwise publicly available.

Statistics

All data have been analyzed through appropriate statistical tests and these are clearly defined.

Methods

The methods are described in sufficient detail to be replicated.

Citations

Previous work has been appropriately acknowledged.

Interpretation

The conclusions are a reasonable extension of the results.

Ethics

The study design, data presentation, and writing style comply with our Editorial Policies.

9.4 Revisions

Authors are required to submit the revised manuscript within one week if minor revision is recommended while two weeks if major revision recommended or one month if additional experiments are needed. If authors need more than one month to revise their manuscript, we usually require the authors to resubmit their paper. We request that a document of point-to-point response to all comments of reviewers and the Editor-in-Chief or the Associate Editor should be supplied along with the revised manuscript to allow quick assessment of your revised manuscript. This document should outline in detail how each of the comments was addressed in the revised manuscript or should provide a rebuttal to the criticism. Manuscripts may or may not be sent to reviewers after revision, dependent on whether the reviewer requested to see the revised version. Apart from in exceptional circumstances, *CES* only supports a round of major revision per manuscript.

10. Contact Us

Journal Contact
Complex Engineering Systems Editorial Office
Suite 1504, Tower A, Xi'an National Digital Publishing Base, No. 996 Tiangu 7th Road, Gaoxin District, Xi'an 710077, Shaanxi, China.

Wen Zhang
Managing Editor
editorial@comengsys.com

Last updated on 2 June, 2023

www.oaepublish.com

Complex Engineering Systems
(*CES*)
Los Angeles Office
245 E Main Street Ste 107, Alhambra,
CA 91801, USA
E-mail: editorial@comengsys.com
Website: www.comengsys.com.